9-Borafluoren-9-yl and diphenylboron tetracoordinate complexes of 8-quinolinolato ligands with heavy-atoms substituents: synthesis, fluorescence and application in OLED devices

Carina B. Fialho,[a] Tiago F. C. Cruz,[a] Maria José Calhorda,[b] Luís F. Vieira Ferreira,[c] Piotr Pander,[d,e,f] Fernando B. Dias,[f] António L. Maçanita,[a] Pedro T. Gomes[a,*]

[a] *Centro de Química Estrutural, Departamento de Engenharia Química, Instituto Superior Técnico, Universidade de Lisboa, Av. Rovisco Pais, 1049-001 Lisboa, Portugal.*
E-mail: pedro.t.gomes@tecnico.ulisboa.pt

[b] *BioISI - Instituto de Biossistemas e Ciências Integrativas, Departamento de Química e Bioquímica, Faculdade de Ciências, Universidade de Lisboa, Campo Grande, 1749-016 Lisboa, Portugal.*

[c] *BSIRG – Biospectroscopy and Interfaces Research Group, IBB-Institute for Bioengineering and Biosciences, Instituto SuperiorTécnico, Universidade de Lisboa, 1049-001 Lisboa, Portugal*

[d] *Faculty of Chemistry, Silesian University of Technology, Strzody 9, 44-100 Gliwice, Poland*

[e] *Centre for Organic and Nanohybrid Electronics, Silesian University of Technology, Konarskiego 22B, 44-100 Gliwice, Poland*

[f] *Department of Physics, Durham University, South Road, Durham DH1 3LE, U.K.*

Abstract

This work describes the synthesis and characterisation of new tetrahedral boron complexes, incorporating bromine- or iodine-substituted 8-quinolinolato chelate chromophores connected to 9-borafluoren-9-yl or diphenylboron orthogonal fragments. The molecular features and photophysical properties of these complexes are analysed in both solution and solid state. Steady-state photophysical studies reveal photoluminescence quantum yields (Φ_f) ranging from 0.02 to 0.15 and prompt fluorescence (PF) lifetimes (τ_f) between 2 and 16 ns. Time-resolved photophysical experiments show the presence of delayed fluorescence (DF) and phosphorescence at both 77 K and room temperature. The DF intensity increases with a rise in temperature. This variation is ascribed to an enhancement in the intersystem crossing (ISC) process promoted by the bromine or iodine heavy-atom effect. Investigations into the dependence of DF intensity relative to the excitation dose indicate emissions stemming either

from Triplet-Triplet Annihilation (TTA), Thermally Activated Delayed Fluorescence (TADF), or a combination of these competing mechanisms. The effect is related to the size and number of heavy-atom substituents in each boron complex. A study of the DF emission intensity as a function of the excitation dose reveals that diiodo-substituted 8-quinolinolato boron complexes, whether rigid or flexible, display TADF emission. Rigid 5,7-dibromo- and 5-chloro-7-iodo-substituted 8-quinolinolato complexes exhibit a combined TADF-TTA mechanism, whereas the other complexes predominantly demonstrate pure TTA emission. DFT and TDDFT calculations showed that the ground state structures reproduced the experimental geometries and only small increases in bond lengths were observed in the excited state geometries. The low energy absorption bands displayed mainly intra-ligand $\pi \rightarrow \pi^*$ (8-quinolinato) character. The fluorescence emission energies were well reproduced, while the singlet-triplet energy gaps were relatively high. Ultimately, organic light-emitting diodes (OLEDs) are fabricated using the most luminescent boron complexes. The best OLED is obtained when using complex **3a**, which displays green electroluminescence (EL) (λ_{EL} = 502 nm) with maximum external quantum efficiency (EQE_{max}) of 2.5% and maximum luminance (L_{max}) of 2200 cd m^{-2}.

Keywords: Boron, DFT calculations, heavy-atom effect, OLED, TADF, triplet-triplet annihilation

1. Introduction

The harvesting of triplet states electrically formed in Organic Light-Emitting Diodes (OLEDs) is of great importance to achieve higher maximum external quantum efficiencies (EQE_{max}), since the conventional fluorescent emitters (the so-called first generation of OLEDs) merely use 25% of the generated excitons (see Fig. 1).[1]

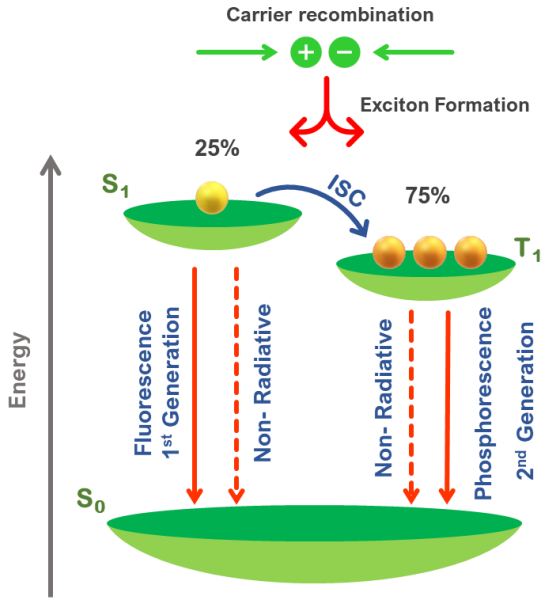

Fig. 1. Diagram of the exciton generation by recombination of holes and electrons, which form 25% of singlet excited states and 75% of triplet excited states, and relaxation pathways to the fundamental state. The excited singlet states can deactivate radiatively by fluorescence (1st generation of OLEDs) or non-radiatively to the ground state (S_0), or undergo intersystem crossing (ISC) to a triplet excited state. The radiative deactivation of the triplet excited states results in phosphorescence (2nd generation of OLEDs), which can also undergo deactivation to the fundamental state through non-radiative processes.

Complexes containing heavy-metal atoms, such as iridium or platinum are typical of the second generation of OLEDs and can reach internal quantum efficiencies (IQEs) close to 100%, thus allowing higher EQEs. These improved efficiencies are achieved by the incorporation of those precious metals, which substantially increases the fabrication cost of OLED devices.[1,2]

The efficiency of singlet exciton formation through harvesting of dark triplet states can be enhanced by employing heavy-metal-free molecules *via* up-conversion (UC) mechanisms leading to delayed fluorescence (DF) (Fig. 2).[3]

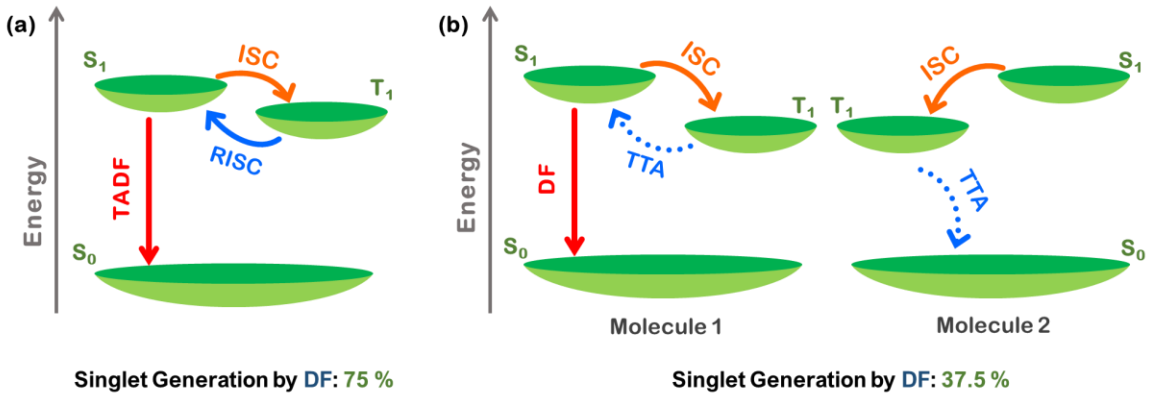

Fig. 2. Diagram of the mechanisms of delayed fluorescence (DF): (a) Thermally Activated Delayed Fluorescence (TADF); (b) Triplet-Triplet Annihilation (TTA).

The third generation of OLEDs is based on the Thermally Activated Delayed Fluorescence (TADF) process, formerly known as E-type delayed fluorescence, which allows to effectively harvest triplet excitons through reverse intersystem crossing (RISC) by thermal activation, reaching EQEs as high as 20-30%.[4] On the other hand, the triplet-triplet annihilation (TTA), formerly known as P-type delayed fluorescence, is a bimolecular phenomenon originated from the collision of two molecules in their triplet excited state. In the latter scenario, with high triplet densities, one of the molecules decays non-radiatively to S_0, and the other one achieves sufficient energy to end up in S_1, enabling the subsequent radiative deactivation to the ground state.[3,5]

The efficiency of TADF emitters depends significantly on the existence of a small energy gap between the singlet and triplet states (ΔE_{ST}).[6] Although TADF is a widely attractive process for its capacity to generate a greater proportion of singlet states *via* UC, it is worth noting that molecules with larger ΔE_{ST} values can still be efficient as emissive layer dopants *via* TTA-based delayed fluorescence. Significant advancements have been made in the development of efficient OLEDs using TTA-emitters with larger EQEs than those of purely fluorescent emitters of the 1st generation. Anthracene [7] and pyrene [8] derivatives have, notably, emerged as candidates, demonstrating pronounced TTA characteristics. Nevertheless, most of the OLEDs utilising the TTA mechanism have primarily focused on blue and deep blue emissions, and those exhibiting green and red emitters remain scarce.[9] To enhance versatility and expand the range of applications, it is fundamental to explore fluorophores in these spectral regions.

Boron-doped materials display interesting properties that make them suitable for application in the emissive layer of OLEDs. Their exceptional photophysical and electrochemical properties can be tuned by incorporating different substituents in the ligand framework.[10]

Recent years have seen an increased interest in both tricoordinated and tetracoordinated boron complexes as promising candidates for TADF emitters.[11]

In four-coordinate boron molecular structures, the LUMO is predominantly located in a π-conjugated chelating ligand. In contrast, the HOMO may reside on either the chelating ligand itself or on the ancillary R ligands, such as aryls, alkyls, or halides, depending on their specific characteristics. The luminescence of these complexes is attributed to intra-ligand π–π* electronic transitions or charge transfer transitions originating from the R groups to the chelating chromophore, which is oriented almost orthogonally. Variations in the structure of the chelating ligand or R groups can typically modulate the emission colours by altering the nature and the gap between the first excited and the ground state. DF properties in four-coordinate boron complexes are notably rare and limited to a small selection of highly fluorescent complexes that demonstrate TADF.[10] Boron-based TTA emitters are even rarer and only a few examples of tetracoordinated complexes have been reported.[12]

In a previous study,[12d] we presented the synthesis of tetrahedral boron complexes featuring 9-borafluoren-9-yl and diphenylboron cores, which were bound to fluorine- and chloride-substituted 8-quinolinolato chelate chromophores (Chart 1). Thin films incorporating these complexes exhibited DF arising from the triplet-triplet annihilation (TTA) process.

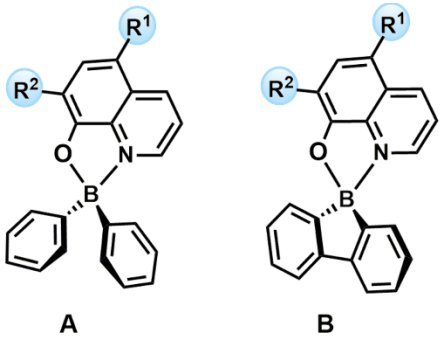

Chart 1. Tetracoordinated boron complexes of diphenylboron (**A**) and 9-borafluouren-9-yl (**B**) coordinated to 8-quinolinato ligands.[12d]

The focus of the present work is to investigate the impact of incorporating heavy-atoms, such as bromine and iodine, in the 8-quinolinato moiety with the aim of enhancing ISC and RISC processes as ways to harvest triplet states, since under electrical excitation there is always 75% triplets formed. The new complexes (see Scheme 1 below) were synthesised and characterised by NMR spectroscopy, elemental analysis, and single crystal X-ray diffraction.

An extensive study was conducted to examine the photophysical properties of the 8-quinolinato boron materials in both solution and film. Steady-state and time-resolved fluorescence techniques were employed to study the photoluminescence characteristics, revealing the presence of DF in the solid-state. Density Functional Theory[13] (DFT) and Time-Dependent Density Functional Theory[14] (TDDFT) studies were performed to understand the photophysical features of this class of compounds. In addition, we selected some of the synthesised boron-based fluorophores for use in fully thermally evaporated OLEDs, which gave green electroluminescence (λ_{EL} = 502 nm) with EQE_{max} of 2.5% and maximum luminance (L_{max}) of 2200 cd m^{-2} as the best result using complex **3a**.

2. Results and Discussion

2.1. Synthesis and characterisation of boron complexes

Tetracoordinated boron complexes **3a**-**3d** and **4a**-**4b** were synthesised through coordination of the monoanionic halide-substituted 8-quinolinolato bidentate ligand chromophores to the 9-borafluoren-9-yl and the diphenylboron moieties, as depicted in Scheme 1.

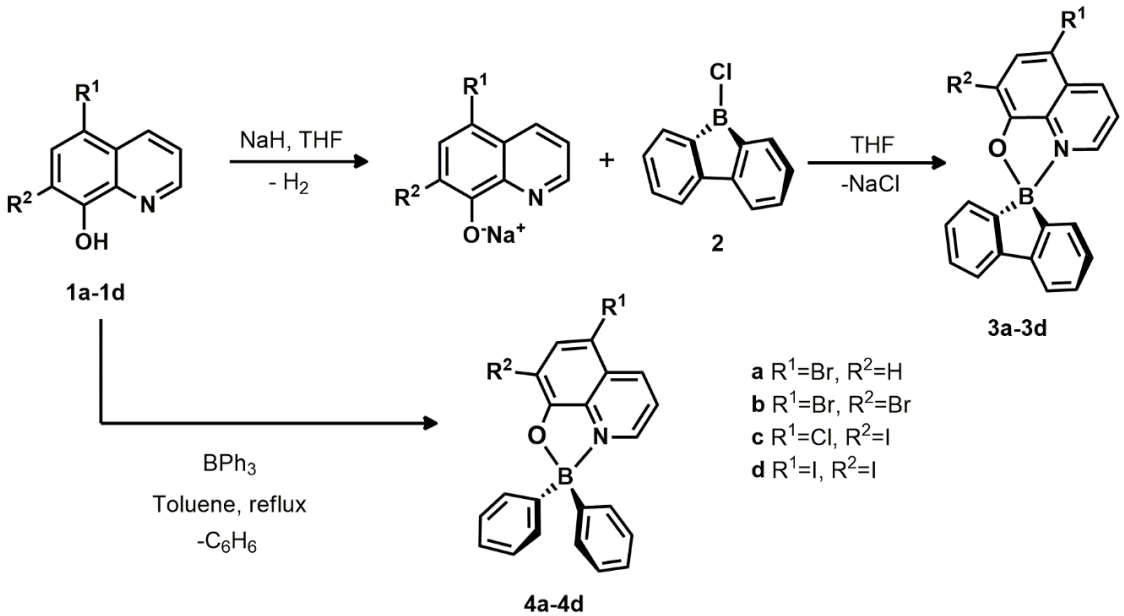

Scheme 1. Syntheses of 9-borafluoren-9-yl (**3a**-**3d**) and diphenylboron (**4a**-**4d**) complexes bearing 8-quinolinolato ligands.

The synthesis of the tetrahedral boron compounds **3a**-**3d**, containing the 9-borafluoren-9-yl core, started with an *in situ* deprotonation of the phenolic hydroxyl proton of the corresponding ligand precursor (**1a**-**1d**), employing a slight excess of sodium hydride at room temperature, in THF. Subsequently, the resulting suspension containing the sodium salt of the ligand precursor was combined with a THF solution of 9-chloro-9-borafluorene[15] (**2**) under controlled low-temperature conditions, leading to the synthesis of the desired products as outlined in Scheme 1. The BPh_2 analogues (**4a**-**4d)** were also prepared to study the effect of the molecular rigidity in the luminescence features. The syntheses of these compounds were adapted from procedures reported in literature,[16] where a solution of the corresponding protonated 8-hydroxyquinoline (*i.e.* 8-quinolinol) **1a**-**1d** was added to a solution of triphenyl boron, both in toluene (Scheme 1). The reaction mixture was refluxed for 16 hours resulting, after purification, in the tetracoordinated boron complexes **4a**-**4d**. Complex **4b** had already been reported in the literature.[16c] However, herein we report an improved and more convenient procedure giving higher yield, at a larger preparative scale.

All the synthesised compounds were obtained in moderate to high yields and their molecular characterisation was conducted using NMR spectroscopy (^{1}H, ^{13}C and ^{11}B) – see Fig. S1-S24 of the Supplementary Material (SM) – elemental analysis and single-crystal X-ray diffraction.

The absence of the O*H* proton resonance in the respective ^{1}H NMR spectra, combined with the appearance of a singlet in the range 8.6-12.9 ppm in the ^{11}B spectra provides evidence for the successful formation of the target boron complexes (three-coordinated ^{11}B resonances typically occur at chemical shifts higher than 25 ppm[17]). Additionally, the presence of ^{1}H and ^{13}C characteristic resonances of the 8-quinolinato and 1,1'-biphenyl-2,2'-diyl (complexes **3**) or bis(phenyl) (complexes **4**) moieties further substantiates this observation.

2.2. X-Ray Diffraction Studies

The molecular structures of compounds **3a**, **3d** and **4a**-**4d** were determined by single-crystal X-ray diffraction, at 150 K. The complexes crystallised in the monoclinic crystal system, in the $P2_1/c$ (complexes **3d** and **4a**) and $P2_1/n$ (complexes **4b**-**4d**) space groups, except for complex **3a**, which crystallised in the triclinic crystal system in the P-1 space group. Even though single crystals of complex **3a** suitable for X-ray diffraction were obtained, the crystal selected for analysis was of poor diffracting quality, presenting a low ratio of observed/unique reflections. Although the structure of complex **3a** was refined to convergence, it is only presented in Fig. S25 of the SM as a proof of its molecular connectivity. The crystal structure of complex **4b** had

already been previously determined at 173 K in a work reported by other authors[16c] and, for this reason, the one determined in this work, at 150 K, is only presented in SM (Fig. S26). Crystallographic data for the molecular structures of these complexes and their most significant bond distances and angles are listed in Tables S1-S4 of the SM. Perspective views of the molecular structures of the boron complexes **3d**, **4a**, **4c** and **4d** are presented in Fig. 3.

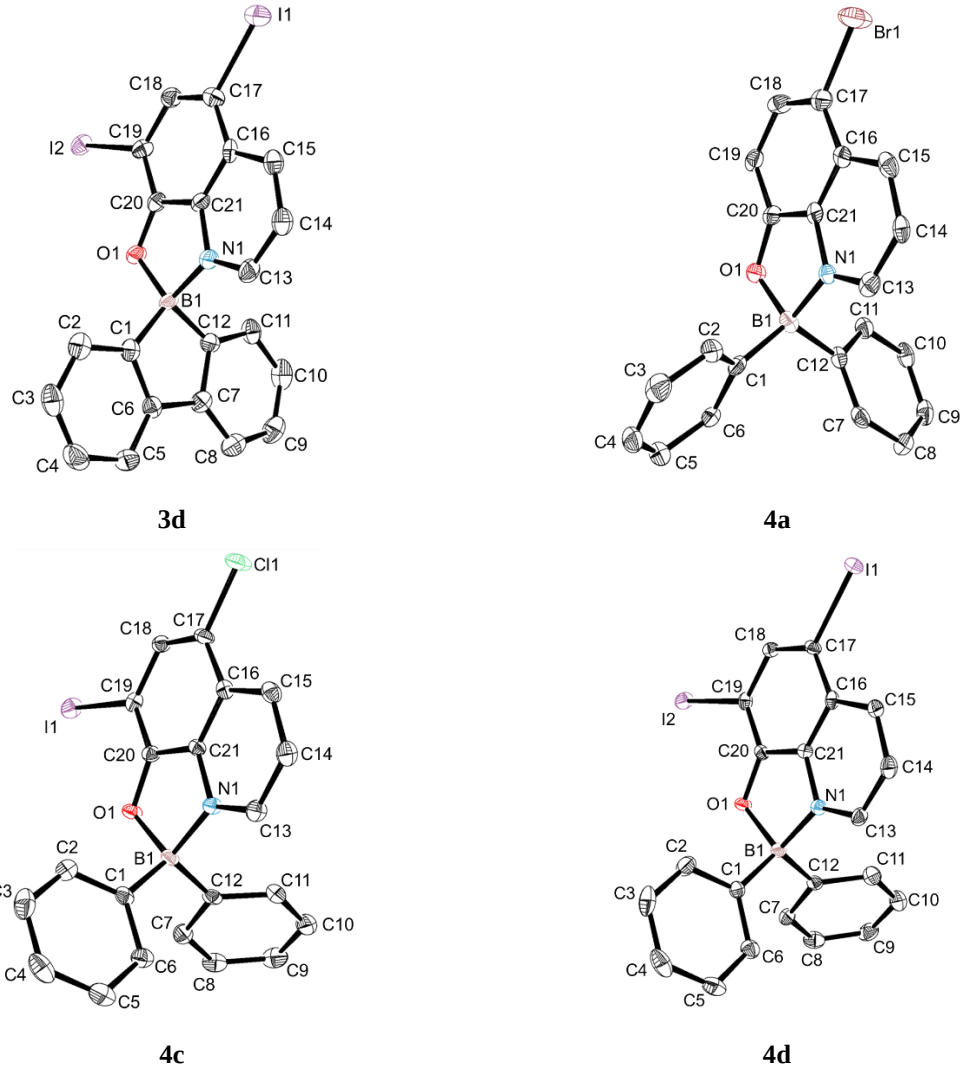

Fig. 3. ORTEP-3 perspective views of the molecular structures of complexes **3d**, **4a**, **4c** and **4d**. The calculated hydrogen atoms were omitted for clarity and the ellipsoids were drawn at the 50% probability level.

The boron complexes display boron centres with near-tetrahedral coordination geometries, including a bidentate 8-quinolinolato chelate and additional co-ligands: the bidentate 1,1-biphenyl-2,2-diyl fragment (*i.e.* 9-borafluorene complex **3a**, which is depicted in Fig. S25 of the SM, and complex **3d**) or two phenyl groups (complexes **4a**-**4d**). The 9-borafluorene complexes **3a** and **3d** feature nearly flat 1,1-biphenyl-2,2-diyl fragments. The angles between

both phenyl rings, defined by the planes containing carbon atoms C1 to C6 and C7 to C12 range from 3.28 to 3.85°. The B1-N1, B1-O1 and B1-C1/B1-C12 bond lengths span 1.617(5)-1.635(5) Å, 1.518(6)-1.549(3) Å and 1.592(4)-1.621(7) Å, respectively. These bond lengths are virtually identical across complexes **3** to **4**. In all crystallographically characterised complexes, the 9-borafluorene and 8-quinolinolato fragments are almost orthogonal, with the angles between their respective chelation planes ranging from 86.23 to 89.36°. The bond lengths and angles observed align with those in other crystallographically characterised boron 8-quinolinolato complexes.[12d,16c,18]

2.3. Molecular geometries and electronic structures

The molecular structures of the 9-borafluoren-9-yl (**3a**-**3d**) and diphenylboron (**4a**-**4d**) complexes **3** and **4** were optimised using DFT calculations[13] with the ADF Program.[19] The PBE0[20,21] functional with spin-orbit coupling effects (SOPERT[22]) and solvent (THF) were considered (method A used in previous related studies; see Computational details). Further calculations were performed with the B3LYP functional and in both cases also with the D3 dispersion correction (see Computational details). TDDFT[14] calculations were used to obtain the absorption spectra, the geometries of the first excited singlet and triplet states and the lifetime of the first singlet state (Figs. S27-S30 of the SM).

The calculated ground state structures of the complexes reproduce very well the X-ray structures of **3d** and **4a**-**4d** (less than 0.02 Å), but not so well that of **3a**. All the bond distances can be found in Tables S3 and S4 (in SM) along with the corresponding experimental values. This good agreement can be seen for the two diiodide derivatives **3d** and **4d** in Fig. S30 (in SM), where the experimental bond distances barely differ from those calculated for the ground state S_0, and the same happens with **4a**-**4c**. The only exception is the **3a** complex (Fig. S27 of the SM). There are two different molecules in the unit cell and, for instance, the two experimental distances B(1)-N(1) are 1.75(3) and 1.68(7) Å, while the calculated value is 1.608 Å. This reflects the poor crystallographic data collected for this complex. This same B(1)-N(1) bond varies for **3d** and **4a**-**4d** between 1.617 and 1.629 Å, comparing very well with the calculated values 1.622 and 1.621 Å. The same behaviour was found in a previous work, where the largest shifts were found for a structure of a similar compound with two independent molecules in the unit cell.[12d]

Slightly smaller bond distances are found for all the complexes when examining the structures of the first singlet and triplet excited states (up to 0.05 Å), but they are still too small

to detect any significant trends, besides that they increase in the order $S_1 < T_1 < S_0$ (for complexes **3a**-**3c** and **4a**-**4c** see Fig. S27-S29 in SM). The same pattern is observed for the angles (O-B-N, O-B-C, N-B-C, C-B-C). The rigid architecture of the complexes is only slightly modified in the excited states, as described in a previous work[12d] dealing with similar complexes carrying F and Cl substituents. The chelation angles O–B–N range from 0° to 0.3° in **3** and 0° to 0.6° in **4**, and C-B-C from 0° to 0.6° in **3** and 0.1° to 0.6° in **4**. The C-B-O/N angles undergo slightly larger changes (2.4° to 5.3° in **3** and 0.8° to 8.8° in **4**). The angles between the O-B-N and C-B-C planes remain very close to 90° in all cases, as observed in the experimentally determined structures. Deviations are even smaller in the 1,1'-biphenyl-2,2'-diyl complexes **3**, with two rigid bidentate ligands, than in the bis(phenyl) derivatives **4**, with only one rigid ligand. This analysis of the changes in angles displays essentially the same trends observed earlier for the F and Cl derivatives.[12d]

2.4. Photophysical studies: absorption spectra and steady-state fluorescence

The photophysical properties of the 9-borafluoren-9-yl complexes **3a**-**3d** and the BPh_2 analogues **4a**-**4d** were investigated in THF solution and in solid-state, using ZEONEX 480R cycloolefin polymer as the dispersion medium. To conduct the studies in solid-state, solutions containing 1% weight ratio of each boron complex and ZEONEX 480R in toluene were deposited in quartz slides using the drop-cast technique to produce thin films. Fig. 4 presents the absorption and fluorescence spectra of all boron complexes, and Fig. 5 their corresponding photoluminescence colours in THF solution, under UV light.

In THF, the absorption wavelength maxima (λ_{abs}^{max}) of the complexes lie between 407-419 nm and their emission wavelength maxima (λ_{em}^{max}) are in the range of 530-544 nm (Table 1). In ZEONEX 480R films, the absorption wavelength maxima (λ_{abs}^{max}) show bathochromic shifts in comparison with the solution values, whereas the emission wavelength maxima (λ_{em}^{max}) reveal hypsochromic shifts, exhibiting values within the 419-426 nm and 522-527 ranges, respectively. Overall, all the compounds display emissions in the green-yellow region and the molar extinction coefficients (ε_{max}), at λ_{abs}^{max}, are very similar between boron complexes **3** and **4**, ranging from 3.6×10^3 to 6.0×10^3 L mol^{-1} cm^{-1}.

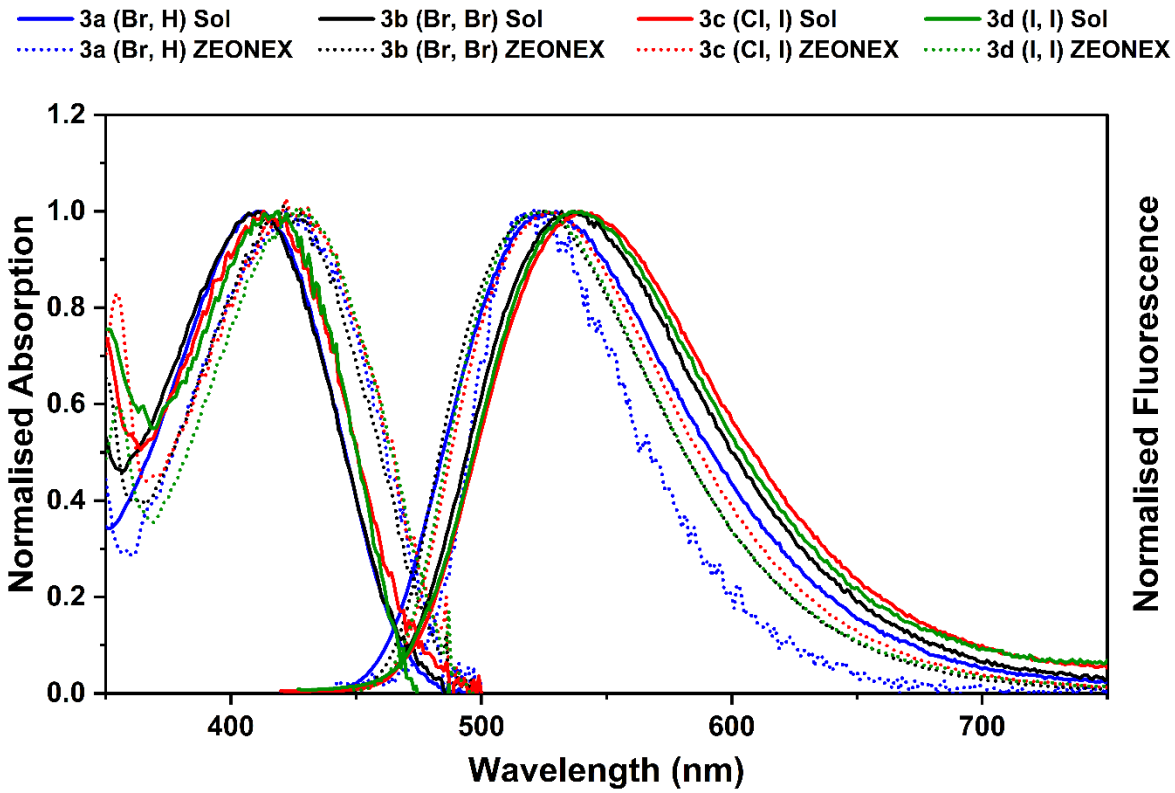

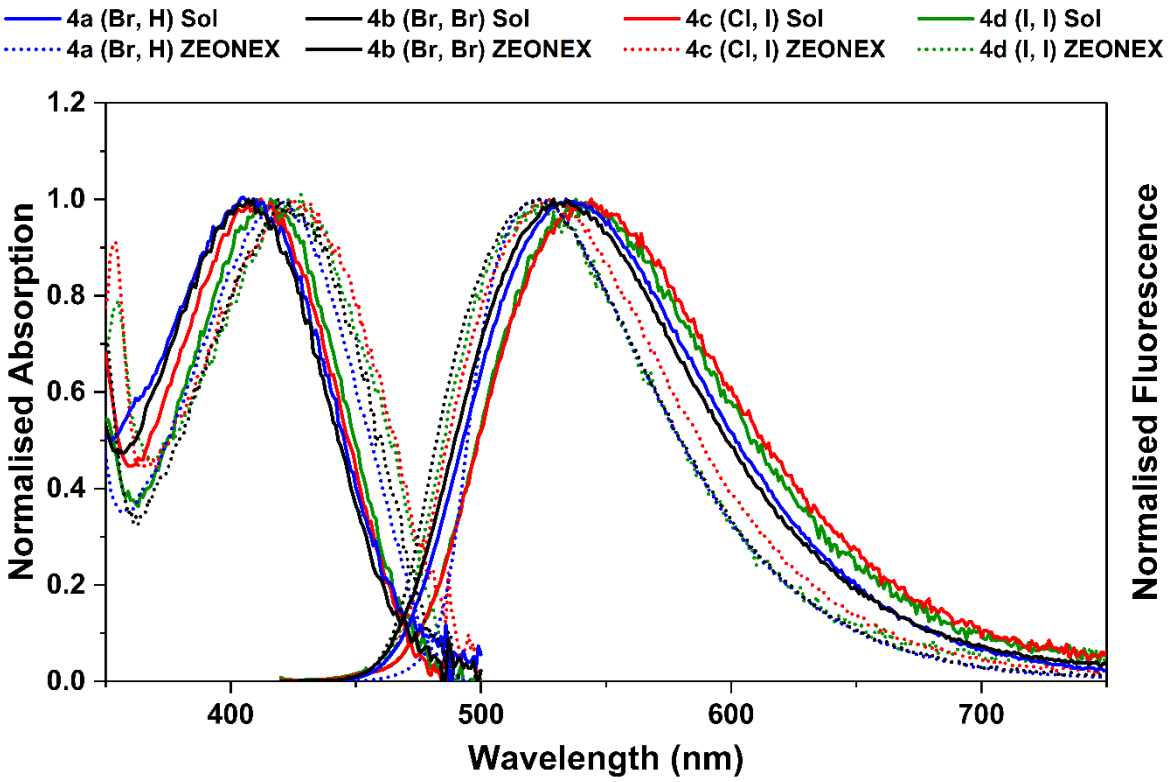

Fig. 4. Normalised absorption and emission spectra of complexes **3** (top) and **4** (bottom) in solution (THF, $OD_{max} < 0.2$, $c < 8\times10^{-5}$) and film (ZEONEX 480R, 1% wt), at 293 K.

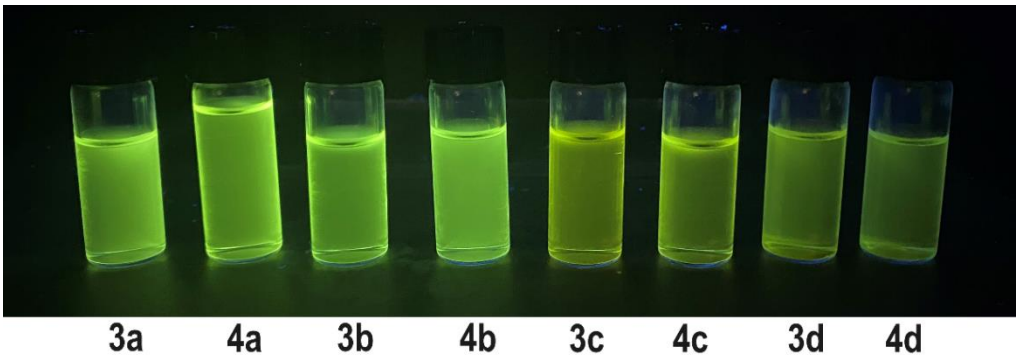

Fig. 5. Photoluminescence of complexes **3** and **4** in solution under UV-irradiation at 365 nm.

Table 1 Summary of photoluminescent characteristics of complexes **3a**-**3d** and **4a**-**4d** in THF solutions and ZEONEX 480R films, at room temperature (r.t.; *ca.* 293 K) and under N_2 atmosphere.

			Solution (THF)							Solid state (ZEONEX 480R film)					
Complex	R^1	R^2	λ_{abs}^{max} [a] (nm)	ε_{max} [b]	λ_{em}^{max} [c] (nm)	Φ_f [d]	τ_f [e,f] (ns)	k_f [g] (ns^{-1})	k_{nr} [h] (ns^{-1})	λ_{abs}^{max} [a] (nm)	λ_{em}^{max} [c] (nm)	Φ_{PL} [d]	τ_{PL} [e,f] (ns)	k_{PL} [g] (ns^{-1})	k_{nr} [h] (ns^{-1})
4a	Br	H	409	5.1	534	0.11	11.0	0.010	0.08	421	522	0.15	14.2	0.011	0.06
3a	Br	H	413	5.7	530	0.15	14.9	0.010	0.06	422	524	0.15	16.3	0.009	0.05
4b	Br	Br	407	6.0	534	0.08	7.9	0.010	0.12	419	523	0.10	11.5	0.009	0.08
3b	Br	Br	413	6.0	537	0.08	6.8	0.012	0.14	421	525	0.12	11.2	0.011	0.08
4c	Cl	I	412	3.6	544	0.06	4.2	0.014	0.22	425	526	0.05	6.0	0.008	0.16
3c	Cl	I	413	4.0	540	0.06	4.7	0.013	0.20	425	527	0.06	6.2	0.010	0.15
4d	I	I	416	5.1	539	0.02	2.0	0.010	0.49	425	523	0.02	2.6	0.008	0.38
3d	I	I	419	5.6	539	0.03	2.1	0.014	0.46	426	524	0.02	2.4	0.008	0.41

[a] Absorption wavelength maxima (λ_{abs}^{max}). [b] Molar extinction coefficient at λ_{abs}^{max} (ε_{max}), 10^3 L mol^{-1} cm^{-1}. [c] Photoluminescence wavelength maxima (λ_{em}^{max}). [d] Fluorescence quantum yields (Φ_f). [e] Fluorescence lifetimes (τ_f). [f] From single exponential decays. [g] Radiative rate constants (k_f); $k_f = \Phi_f/\tau_f$. [h] Sum of non-radiative rate constants (k_{nr}); $k_{nr} = k_{ic} + k_{isc}$.

Upon switching the medium from ZEONEX 480R to THF, the increased medium polarity induces a blue-shift in the absorption spectra and a red-shift in the fluorescence spectra across all the complexes. Similarly to the previously reported complexes shown in Chart 1,[12d] this is not a typical behaviour of π-π* electronic transitions in conventional boron-free organic compounds.

TDDFT calculations (see Table S5 and more details below) revealed that these complexes have a more polar ground state (S_0) than the S_1 state at the Franck-Condon geometry (S_{1FC}) as shown by dipole moments in the range 5.86-7.73 D and 4.72-6.50 D, respectively. The former is more stabilised by the larger polarity, resulting in the observed hypsochromic shift in the absorption spectra when THF is the medium. After subsequent relaxation to the first excited state (S_1), the dipole moment increases (values from 5.95 to 7.85 D), and S_1 becomes more

stabilised than the ground state (S_0). Thus, a bathochromic shift in the emission spectra is observed when the medium is more polar.

The fluorescence quantum yields (Φ_f) of materials **3** and **4** fall within the range of 0.02-0.15. No significant disparity is observed due to the rigidification of the molecules by altering the medium from THF to ZEONEX 480R. In general, the values of k_f exhibit a small variation (Table 1), aligning closely with those of the previously reported fluorinated and chlorinated analogues.[12d] However, the non-radiative rate constant values k_{nr} ($k_{nr} = k_{ic} + k_{isc}$, *i.e.* the sum of the internal conversion (IC) and ISC rate constants) show a marked increase in the mono- and bis-iodinated complexes. In fact, it is particularly noteworthy that an increase in both the number and size of heavy-atoms significantly reduces the fluorescence quantum yield. Additionally, in contrast to the previously studied chlorine- and fluorine-substituted analogues,[12d] the radiative deactivation of the triplet states through phosphorescence is observed in time-gated luminescence spectra of complexes **3** and **4**. These observations were made in 2-Me-THF, at 77 K, using a 50 µs of delay upon excitation and a 10 ms time window (Fig. S31 in SM). The presence of phosphorescence partly explains the low fluorescence quantum yields obtained, which are likely attributable to an enhanced intersystem crossing due to the heavy-atom effect.

The fluorescence and phosphorescence spectra enabled the calculation of experimental ΔE_{ST} values in 2-Me-THF based on the emissions onsets, which are listed in Table 2 (and in Fig. S31). These ΔE_{ST} values are relatively similar, in a range of 0.55-0.70 eV.

Table 2 Experimental ΔE_{ST} values (energy gap between the singlet and triplet states) calculated from the emissions onsets. The experimental values were measured in 2-Me-THF solutions, and in ZEONEX 480R films, at 77 K. All energy values in eV.

Complex	R^1	R^2	2-Me-THF			ZEONEX		
			S_1	T_1	ΔE_{ST}	S_1	T_1	ΔE_{ST}
3a	Br	H	[a]	[a]	[a]	2.64	2.12	0.52
4a	Br	H	[a]	[a]	[a]	2.64	2.14	0.50
3b	Br	Br	[a]	[a]	[a]	2.70	2.10	0.60
4b	Br	Br	2.78	2.13	0.65	2.70	2.10	0.60
3c	Cl	I	2.67	2.08	0.59	2.68	2.07	0.61
4c	Cl	I	2.71	2.10	0.61	2.68	2.07	0.61
3d	I	I	2.68	2.13	0.55	2.67	2.06	0.61
4d	I	I	2.75	2.13	0.62	2.68	2.07	0.61

[a] Not determined due to low signal-to-noise ratio.

2.5. TDDFT calculation of electronic transitions and excited state energy

The energy of electronic transitions and of the first excited singlet and triplet states, as well as the lifetime of S_1, were obtained from TDDFT calculations, including the spin-orbit term and the solvent (THF) correction.

The lowest energy electronic transitions of complexes **4** are from the HOMO to the LUMO (96-97%) in all cases, while those of **3** consist of HOMO to LUMO and HOMO-1 to LUMO excitations (see Table S6 in SM). These molecular orbitals and their energy (in eV) can be seen in Fig. 6 for **3c**, **3d**, **4c** and **4d**, and in Fig. S32 for **3a**, **3b**, **4a** and **4b**. The energies of the frontier orbitals (HOMO and LUMO) calculated by several methods are shown in Table S7 (in SM).

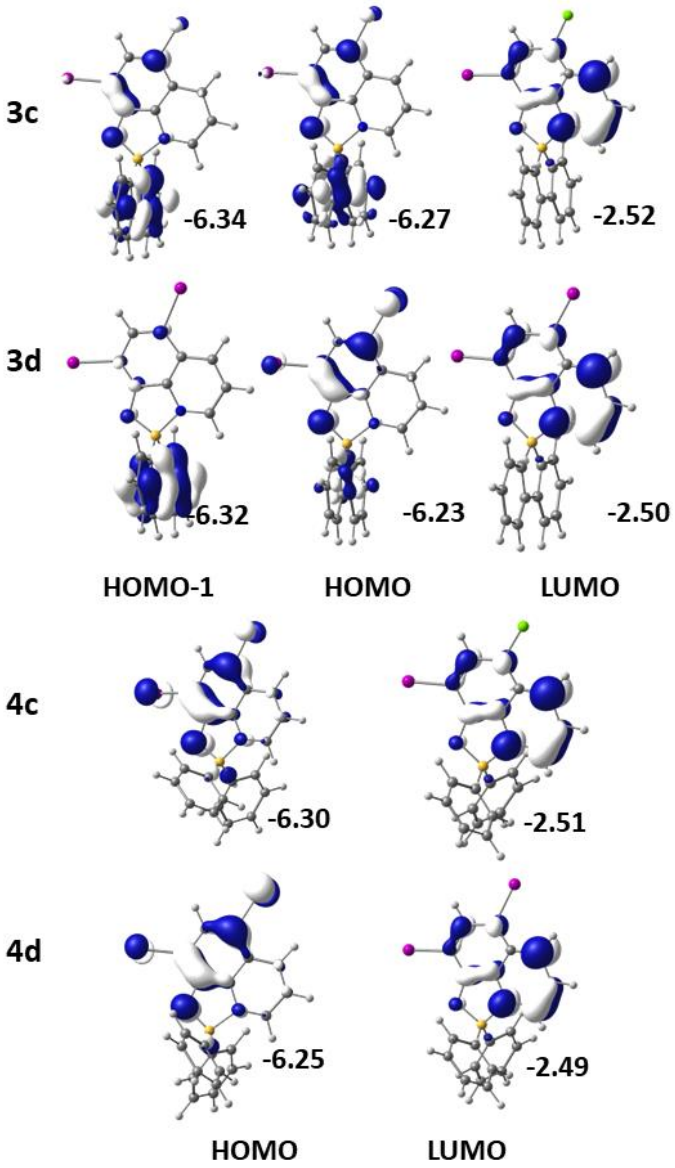

Fig. 6. Relevant frontier molecular orbitals and their energies (eV) for complexes **3c**, **3d**, **4c** and **4d**.

The analysis of the orbitals indicates that for all the complexes **4** both the HOMO and the LUMO are localised in the 8-quinolinato ligand, so that the HOMO to LUMO transition corresponds to a $\pi \rightarrow \pi^*$ (8-quinolinato) excitation. The frontier orbitals of complexes **3** differ from those of complex **4**. While the LUMO remains in the 8-quinolinato, the HOMO and HOMO-1 are always delocalised over the two bidentate ligands, as also found in analogous complexes with H/H, H/F, and H/Cl substituents.[12d] In all these species, the lowest energy absorption, consisting of two excitations from HOMO-1 and HOMO to LUMO, have both a partial charge transfer character from one ligand to the other and an intra-ligand $\pi \rightarrow \pi^*$ (8-quinolinato) character. A slightly different interpretation arises from the plots of the density transfer for the lowest energy transition, which are shown in Fig. 7 for **3d** and **4d**. The main character is indeed intra-ligand $\pi \rightarrow \pi^*$ (8-quinolinato), as almost all the density is in the 8-quinolinato ligand. The role of the remaining ligands is very small, as expected for **4d** (or **4a-4d**) but not for **3d**. There is more electron density for the latter, but less than expected from the HOMO and HOMO-1, suggesting that the contributions of these orbitals are out of phase and almost cancel each other out (analogous plots for complexes **3a-3c** and **4a-4c** are shown in Fig. S33).

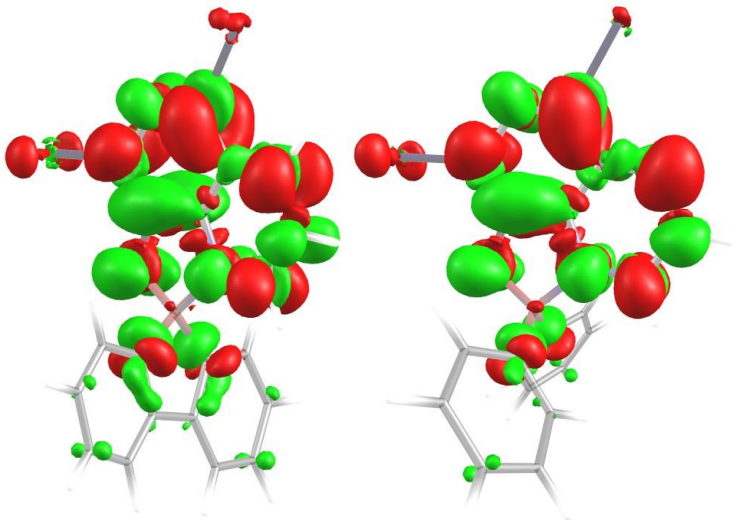

Fig. 7. Charge density plots for complexes **3d** (left) and **4d** (right) for the lowest energy transition (red: increased electron density; green: decreased electron density; contour value 0.0009).

The calculated absorption maxima shown in Table 3 reproduce very well the experimental values, with shifts between 0 and 13 nm.

Table 3. Comparison of the experimental (solution) and TDDFT-calculated photophysical properties of boron complexes **3a**-**3d** and **4a**-**4d**.

Complex	R^1	R^2	λ_{abs}^{max} [a]		λ_{em}^{max} [b]		τ_f [c]		T_1 [d]		ΔE_{ST} [e]		SOC [f]
			exp (nm)	calc (nm)	exp (nm)	calc (eV, nm)	exp (ns)	calc (ns)	exp (nm)	calc (eV, nm)	exp (eV)	calc (eV)	calc (cm^{-1})
4a	Br	H	409	400	534	2.32 (533)	11.0	13.9	[g]	1.44 (862)	[g]	0.89	0.97
3a	Br	H	413	400	530	2.32 (534)	14.9	20.8	[g]	1.43 (868)	[g]	0.89	0.75
4b	Br	Br	407	404	534	2.33 (533)	7.9	15.9	[g]	1.46 (847)	[g]	0.88	0.48
3b	Br	Br	413	408	537	2.33 (533)	6.8	22.8	634	1.45 (856)	0.65	0.86	0.71
4c	Cl	I	412	406	544	2.29 (541)	4.2	19.1	624	1.43 (868)	0.59	0.87	4.00
3c	Cl	I	413	408	540	2.30 (540)	4.7	25.5	628	1.42 (872)	0.61	0.86	0.92
4d	I	I	416	416	539	2.30 (540)	2.0	17.7	624	1.47 (846)	0.55	0.84	2.17
3d	I	I	419	415	539	2.30 (540)	2.1	18.4	628	1.46 (851)	0.62	0.83	2.83

[a] Absorption maxima (λ_{abs}^{max}) in THF. [b] Fluorescence emission maxima (λ_{em}^{max}) in THF. [c] Fluorescence lifetimes (τ_f). [d] Triplet state energy (T_1); the experimental values are the phosphorescence emission maxima, in 2-Me-THF, at 77 K. [e] Energy gap between S_1 and T_1 (ΔE_{ST}). [f] Calculated spin-orbit coupling values between T_1 and S_1. [g] Not determined due to low signal-to-noise ratio.

The role of spin-orbit coupling (SOC) was analysed in the absorption spectra, as done earlier for related tetrahedral *N*-iminopyrrolyl boron complexes containing iodide substituents.[23] The simplest way to detect it is to compare the absorption spectra calculated with and without spin-orbit coupling (Fig. S34 of the SM). The two curves almost superimpose for complexes **3a** and **4a** and they start to shift progressively when going to **3b** and **4b**, and **3c** and **4c**. There is a clear difference in the two curves for **3d** and **4d**, indicating that spin-orbit coupling should influence the behaviour of these complexes. The SOC values between S_1 and T_1 were calculated from the $\langle S|\hat{H}_{SOC}|T\rangle$ matrix elements and are listed in Table 3. The trend indeed indicates that ISC should be favoured for the iodine containing complexes (in particular, for **4c**, **3d** and **4d**).

The fluorescence emission energies obtained from the TDDFT calculations are also in excellent agreement with the experimental ones, the maximum deviation being 4 nm (Table 3). The calculated fluorescence lifetimes (τ_f) reproduce the experimental values for **4a** and **3a**. The remaining complexes, exhibiting an increasing heavy-atom effect, show much shorter experimental lifetimes than those obtained from TDDFT, because other effects, such as ISC and IC, start to quench the fluorescence and are not considered in these calculations. The energies of S1 and T1 obtained with several methods (other functional and dispersion effects), given in Table S8 (in SM), show no significant difference. On the other hand, the energies of the triplet excited states are significantly shifted from the experimental values, thus the experimental and calculated ΔE_{ST} values also differ from each other.

2.6 Photophysical studies: time-resolved luminescence

The time-resolved luminescence studies in films were conducted at room temperature and at 77 K for compounds **3** and **4** dispersed in ZEONEX 480R (1% wt). Fig. 8 shows the spectra of compounds **3b**, **3d**, **4b** and **4d**. Spectra of the remaining compounds (**3a**, **3c**, **4a** and **4c**) are presented in SM (Fig. S35). The delayed fluorescence and phosphorescence emission spectra maxima along with the respective decay lifetimes (τ_{DF} and τ_P, respectively) are listed in Table 4.

Under the specific experimental conditions employed, with a start delay of approximately 20 μs, only delayed fluorescence and phosphorescence were observed. All compounds demonstrated DF at both room temperature and 77 K. These measurements were conducted in air as samples purged with argon showed no enhancement in DF intensity. This indicates that the diffusion of molecular oxygen within the polymer films is negligible, and consequently, O_2 does not significantly quench the triplet states involved in the DF mechanism.

In the case of complexes **3d** and **4d**, the well-resolved phosphorescence bands at both 77 K and room temperature allow the calculation of phosphorescence lifetimes (τ_P), which are remarkably similar to the corresponding DF lifetimes (τ_{DF}) listed in Table 4. This similarity suggests the presence of a TADF process.[24] However, the experimental ΔE_{ST} values obtained in ZEONEX 480R films (Table 2), which range from 0.50 to 0.61, indicate that TADF would be unlikely to occur.[6]

To better understand the nature of the long-lived photoluminescence, studies of delayed fluorescence intensity as a function of the excitation dose were conducted at room temperature, as no pronounced TADF can be observed at 77 K. To determine whether the DF process is driven by a unimolecular or a bimolecular mechanism, it was necessary to plot the experimental data in a log-log scale by linearising the general formula $Y = aX^b$, *i.e.* $\log Y = b \log X + \log a$. Here, Y represents the DF intensity, X the excitation dose, and a and b are fitting parameters. The value of b (slope) in this linearised equation is crucial: a value of $b = 1$ suggests a unimolecular process, while a value of $b = 2$ suggests a bimolecular process involving two excited molecules. Examples of the spectra obtained are shown in Fig. 9 for compounds **3d** and **4a**, with the spectra for the other complexes presented in Fig. S36 in the SM. The values b obtained for complexes **3** and **4** in ZEONEX 480R films, at room temperature, are listed in Table 5.

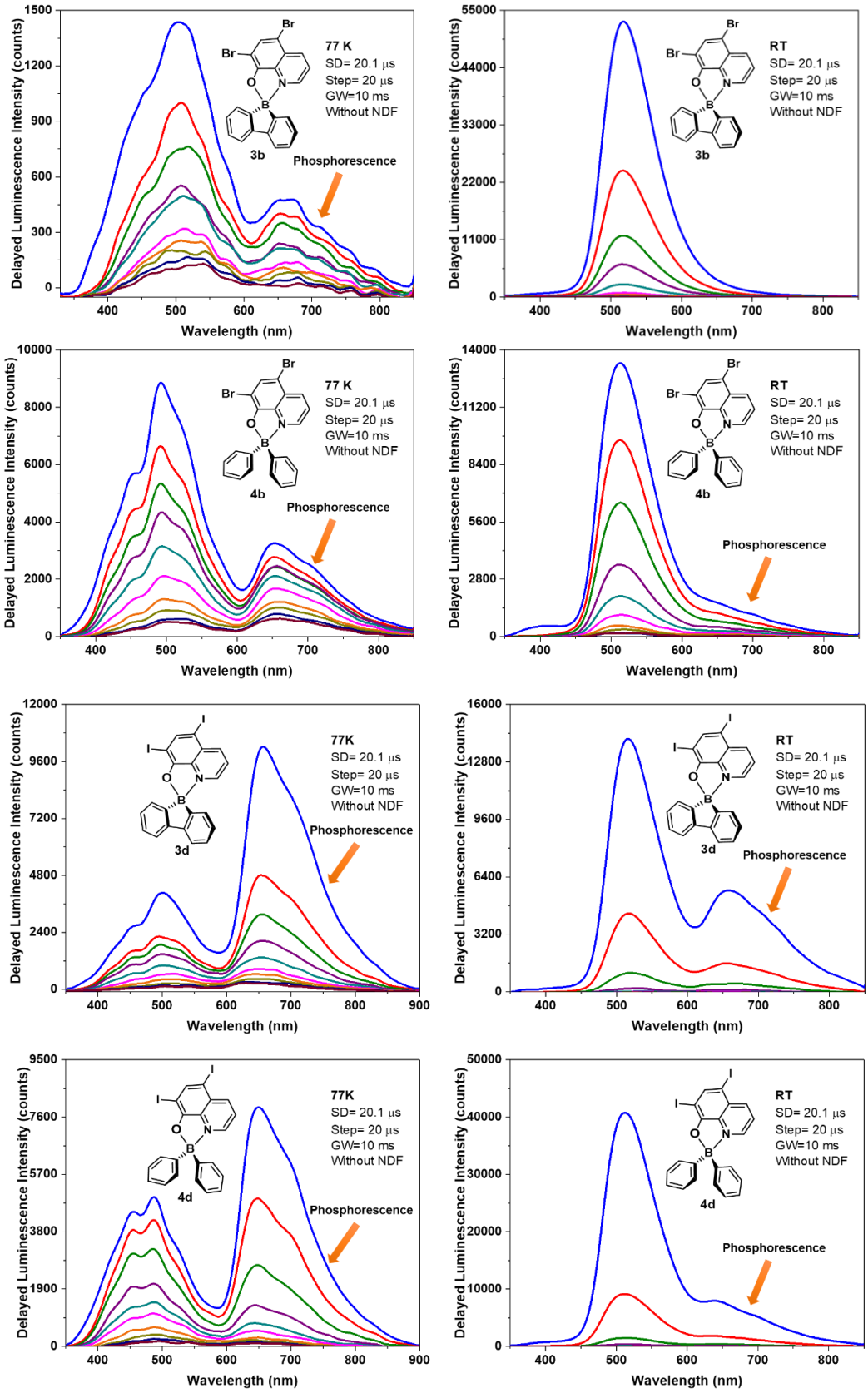

Fig. 8. Transient emission spectra of complexes **3b**, **3d**, **4b** and **4d** in ZEONEX 480R films (1% wt) at 77 K (left) and room temperature (*ca.* 293 K) (right). All spectra were recorded with a start delay (SD) of 20.1 μs (blue curve) and recorded every 20 μs (Step), with the use of a large gate width (GW=10 ms). DF intensity decreases with increasing delay time.

Table 4. Delayed fluorescence lifetimes (τ_{DF}) and emission maxima for boron complexes **3a**-**4d** and **4a**-**4d**, at r.t. and 77 K, in solid state ZEONEX 480R films.

Complex	R^1	R^2	PF [a]		DF [b]							
			r.t. [c]		r.t. [c]				77 K			
			λ_{em}^{max} [d,e]	τ_f [a,e]	λ_{em}^{max}	τ_{DF} [f]	$\lambda_{em(P)}^{max}$ [g]	τ_P [f]	λ_{em}^{max}	τ_{DF} [f]	$\lambda_{em(P)}^{max}$ [g]	τ_P [f]
			(nm)	(ns)	(nm)	(μs)	(nm)	(μs)	(nm)	(μs)	(nm)	(μs)
4a	Br	H	522	14.2	516	24.0	[h]	[h]	504	51.4	661	[i]
3a	Br	H	524	16.3	517	23.7	[h]	[h]	520	41.4	664	74.2
4b	Br	Br	523	11.5	513	34.2	[i]	[i]	492	59.5	658	112.4
3b	Br	Br	525	11.2	518	23.1	[h]	[h]	508	71.4	660	79.1
4c	Cl	I	526	6.0	516	22.0	[h]	[h]	492	82.6	657	102.9
3c	Cl	I	527	6.2	520	22.2	[i]	[i]	500	72.1	662	86.9
4d	I	I	523	2.6	512	12.4	640	12.0	487	45.6	650	46.6
3d	I	I	524	2.4	516	15.4	657	14.9	501	49.5	660	49.5

[a] PF: Prompt fluorescence. [b] DF: Delayed fluorescence. [c] r.t.= *ca.* 293 K. [d] Steady-state fluorescence. [e] Data reproduced from Table 1. [f] From ln(*I*) vs. time plots, where *I* is the DF intensity. [g] Phosphorescence wavelength maxima. [h] No detectable phosphorescence. [i] Not determined due to low signal-to-noise ratio.

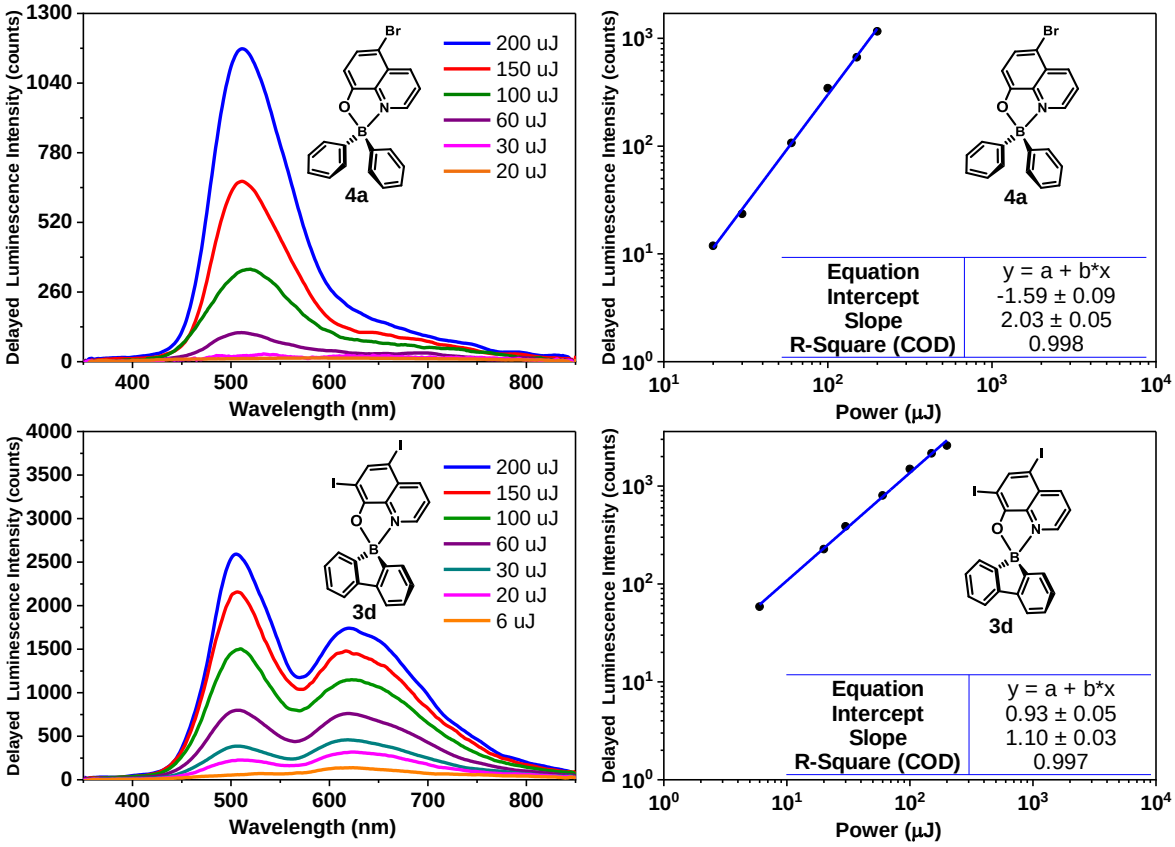

Fig. 9. Left: Dependence of the DF intensity (with a start delay (SD) of 20 μs) on the excitation dose for complexes **4a** and **3d** in ZEONEX 480R films, at room temperature (*ca.* 293 K). Right: log-log plot of DF intensity versus excitation dose.

Table 5. Values obtained for the *b* parameter (slope) in the log-log plot of DF intensity (SD = 20 μs) *versus* excitation dose, at room temperature, for complexes **3** and **4** in ZEONEX 480R films.

Complex	R^1	R^2	*b*
4a	Br	H	2.03 ± 0.05
3a	Br	H	2.14 ± 0.05
4b	Br	Br	1.98 ± 0.03
3b	Br	Br	1.38 ± 0.04
4c	Cl	I	2.23 ± 0.05
3c	Cl	I	1.42 ± 0.08
4d	I	I	1.02 ± 0.03
3d	I	I	1.10 ± 0.03

For compounds **3a**, **4a**, **4b** and **4c**, the parameter $b \approx 2$ indicates a bimolecular process characteristic of TTA. This is supported by the DF lifetimes observed for these complexes (Table 4), which are roughly half of their respective phosphorescence lifetimes.[24]

Higher temperature promotes molecular diffusion, thereby enhancing the probability of collisions between molecules (*i.e.* supporting TTA). This effect is less pronounced in heavy-atom-free molecules, as in those complexes the population of triplet states is comparatively low at room temperature.[12d]

In contrast, the behaviour of boron complexes **3d** and **4d**, which contain two iodine atoms, is markedly different. Increasing the excitation dose leads to a roughly proportional increase in DF, hence $b \approx 1$, confirming that unimolecular luminescent processes, such as that of TADF, are dominant. We speculate that the intensified heavy-atom effect helps the RISC process, thereby promoting TADF, despite the high ΔE_{ST} exhibited by complexes **3d** and **4d** (as well as by the other complexes). However, their low fluorescence quantum yields (0.03 and 0.02, respectively – see Table 1) render them unsuitable for use in OLED devices. The Jablonski diagrams of **3d** and **4d** are depicted in Fig. 10 to illustrate the photophysical processes occurring in these complexes.

For compounds **3b** and **3c**, $b \approx 1.4$, which suggests the potential interplay of both TTA and TADF processes. In these complexes, the phosphorescence lifetimes exceed those of DF (Table 4), although being far from twice those of DF, and confirm that both mechanisms likely operate simultaneously. This interplay appears more pronounced in the more rigid complexes, hinting that rigidification may also promote the RISC process to some extent. The diagrams of complexes **3a**-**3c** and **4a**-**4c** are in the SM (Fig. S37).

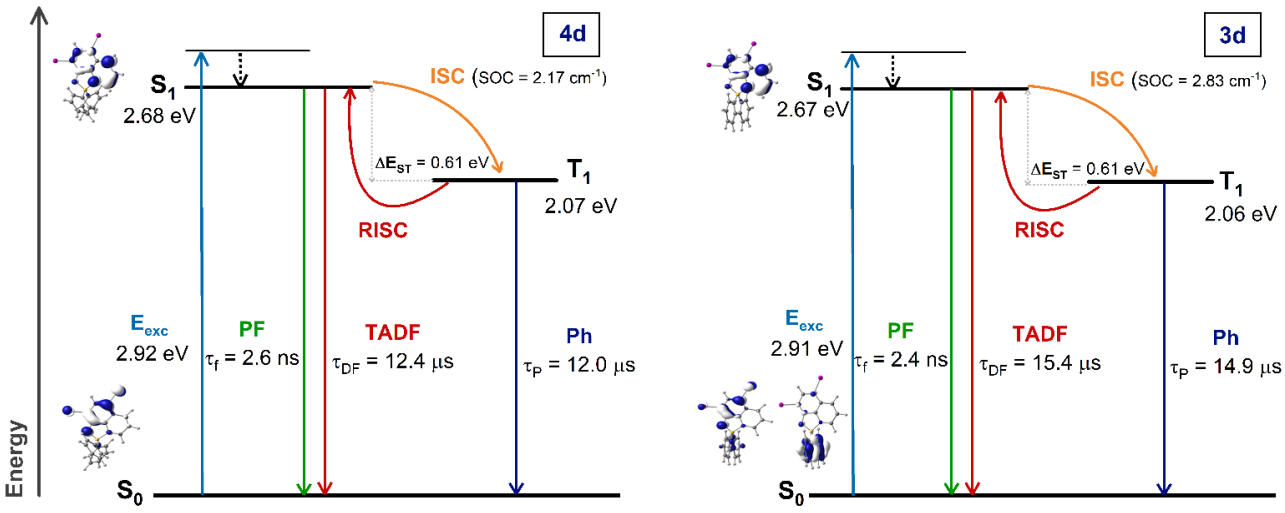

Fig. 10. Jablonski diagrams of complexes **3d** (right) and **4d** (left) illustrating their most relevant photophysical processes and properties, in ZEONEX 480R films, at room temperature (*ca.* 293 K). The values exhibited are experimental, except those of the DFT-calculated SOC values.

2.7. Electroluminescence studies

OLED devices employing brominated complexes **3a**, **4a**, **3b**, and **4b** have been produced using the same architecture as previously presented for analogous emitters: ITO | HAT-CN (10 nm) | TSBPA (40 nm) | mCP (2 nm) | mCP co 10% **emitter** | PO-T2T (5 nm) | TPBi (40 nm) | LiF (0.8 nm) | Al (100 nm) (Fig. S38 in SM).[12d] Here HAT-CN serves as the hole injection layer, followed by TSBPA hole transport layer. A thin 2 nm mCP layer is added between TSBPA and the EML as a spacer, which is followed by the EML comprising mCP as host and 10% organoboron compound **3a**, **4a**, **3b** or **4b** as the emitter. PO-T2T serves as the hole blocking layer, while TPBi is the electron transport layer. For simplicity, we use emitter codes when referring to individual devices using the respective complexes in the emissive layer. Acronyms used for describing the OLED architecture are explained in the Experimental section.

In general, the behaviour of OLEDs **3a**, **4a**, **3b**, and **4b** is similar to that reported earlier for analogous boron complexes.[12d] A summary of OLED characteristics is presented in Table 6 and the most important OLED characteristics and the EL spectra are shown in Fig. 11.

Table 6. Characteristics of OLED devices using complexes **3a**, **4a**, **3b**, and **4b** in the emissive layer. Structure of devices: ITO | HAT-CN (10 nm) | TSBPA (40 nm) | mCP (2 nm) | mCP co 10% **emitter** | PO-T2T (5 nm) | TPBi (40 nm) | LiF (0.8 nm) | Al (100 nm).

	Dev 1	**Dev 2**	**Dev 3**	**Dev 4**
Emitter	**3a**	**4a**	**3b**	**4b**
V_{ON} / V [a]	4.5	5.5	5.6	7.0
L_{max} / cd m^{-2} [b]	2200	1700	2200	1300
λ_{EL} / nm [c]	502	501	499	495
CIE 1931 (x; y) [d]	(0.27; 0.50)	(0.27; 0.50)	(0.25; 0.49)	(0.25; 0.47)
CE_{max} / cd A^{-1} [e]	6.4	6.0	4.4	3.7
EQE_{max} / % [f]	2.5	2.2	1.5	1.5

[a] Turn-on voltage at 10 cd m^{-2}. [b] Maximum luminance. [c] Electroluminescence spectrum maxima. [d] Colour coordinates of electroluminescence spectrum as defined in International Commission on Illumination colour space CIE 1931. [e] Maximum current efficiency. [f] Maximum external quantum efficiency.

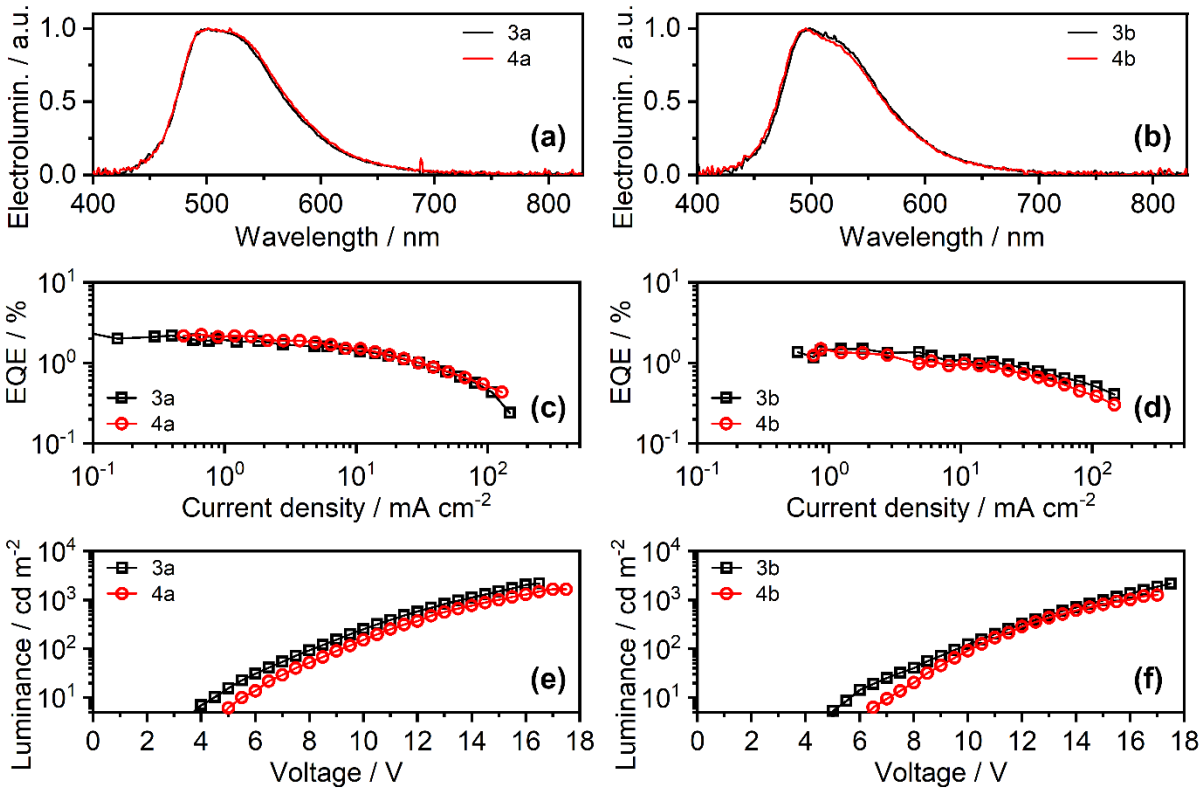

Fig. 11. Characteristics of OLED devices using complexes **3a**, **4a**, **3b**, and **4b** in the emissive layer: (a) and (b) Electroluminescence spectra; (c) and (d) EQE - current density; and (e) and (f) Luminance – voltage bias.

The OLED EQE reported here is slightly lower than that obtained earlier for analogous complexes substituted with lighter halogens (Chart 1), which is in line with fluorescence quenching caused by bromine heavy-atoms. The mono-Br compounds **3a** and **4a** display a slightly higher EQE than the di-Br analogues **3b** and **4b**, again in line with the heavy-atom effect and in agreement with their luminescent characteristics (Table 1). The EL spectra are nearly identical within the **3a**/**4a** and **3b**/**4b** pairs, but the latter pair displays a slightly blue shifted emission. All devices display green electroluminescence. The EQEs within each pair are comparable with each other, but the luminance of devices **4a** and **4b** is significantly lower than that of **3a** and **3b**, respectively. This appears to be most likely related to their electrical rather than photophysical characteristics. For example, OLEDs **3a**/**3b** display lower optical V_{ON} than the respective counterparts **4a**/**4b**. In **3a**/**4a**, the higher electrical V_{ON} in **4a** is accompanied by a generally lower current density at every given applied voltage in **4a** than in **3a** (Fig. S39 in SM). The **4b** OLED displays a lower EQE at low current densities than **3b** as well as a slightly more significant efficiency roll-off, hence also resulting in lower maximum luminance and higher optical V_{ON} of the former device.

In summary, borafluorene derivatives **3a** and **3b** appear to be slightly better OLED emitters than the diphenyl boron analogues **4a** and **4b**. The maximum luminance of 2200 cd m^{-2} and maximum EQE of 2.5% in this set of devices are recorded for OLED **3a**.

3. Conclusions

We have synthesised and structurally characterised seven new 9-borafluoren-9-yl and diphenylboron complexes (**3a**-**3d**, **4a**, **4c** and **4d**, respectively). The structures incorporate bromine- or iodine-substituted 8-quinolinolato *N*,*O*-bidentate ligands as chromophores, and display distorted tetrahedral geometries around the boron atom.

These complexes exhibit fluorescent properties, displaying green-yellow emission colours. The photophysical study reveals film photoluminescence quantum yields (Φ_f) ranging from 0.02 to 0.15 and prompt fluorescence (PF) lifetimes (τ_f) between 2 and 16 ns. The lower values correspond to the diiodo-substituted complexes **3d** and **4d**, while the higher figures are associated with the monobromo-substituted complexes **3a** and **4a**. These values are notably smaller than those recorded for the previously reported unsubstituted as well as the fluorine- and chlorine-substituted 8-quinolinolate analogues.[12d]

The TDDFT calculated absorption and emission energies reproduce very well the experimental values. The nature of the $S_0 \rightarrow S_1$ transition is mainly 8-quinolinolato π-π* (intra-ligand) for all complexes. The role of spin-orbit coupling is reflected on the absorption spectra of the complexes containing heavier halogens. Higher SOC values between S_1 and T_1 also confirm that ISC is more likely to occur in complexes **4c**, **3d** and **4d**. Time-resolved luminescence experiments demonstrate that complexes **3a**-**3d** and **4a**-**4d** exhibit delayed fluorescence (DF) in ZEONEX 480R films at both 77 K and room temperature. Phosphorescence is observed in all complexes at 77 K and, for **3c**, **3d**, **4b** and **4d**, also at room temperature. These phenomena are attributed to an enhancement in the intersystem crossing (ISC) rate due to the heavy-atom effect induced by the heavy halogen substituents. Unlike in the case of their unsubstituted and fluorine- or chlorine-substituted 8-quinolinolate counterparts,[13d] higher temperatures markedly enhance the DF intensity of complexes containing heavy halogens. Laser fluence experiments reveal that the DF at r.t. is of the following nature: 1) TTA for complexes **3a**, **4a**, **4b** and **4c**; 2) TADF-dominated in **3d** and **4d**; 3) a combination of TTA and TADF in complexes **3b** and **3c**. These observations are corroborated by the comparison of the DF lifetimes (τ_{DF}) with those of phosphorescence lifetimes (τ_P), at 77 K. In complexes displaying TADF, $\tau_{DF} \approx \tau_P$, whereas in those exhibiting TTA, $\tau_{DF} \approx ½\tau_P$. In complexes exhibiting a mixed mechanism TTA + TADF, the τ_P values exceed those of τ_{DF}, although far from $\tau_{DF} \approx ½\tau_P$. This behaviour stands in contrast to their non-heavy-atom-substituted counterparts, which exclusively exhibit DF of TTA nature. Despite significant ΔE_{ST}, in the range of 0.55-0.65 eV, TADF is observed in some of complexes **3** and **4**, especially those containing the more rigid 9-borafluorenyl fragment and a higher degree of heavy-atom substitution in the 8-quinolinolato ligand.

Finally, OLED devices were fabricated using the more emissive luminophores, which showed green electroluminescence ($\lambda_{EL} \approx 502$ nm). The best-performing OLED, using emitter **3a**, demonstrated an external quantum efficiency (EQE) of 2.5%, and a maximum luminance (L_{max}) of 2200 cd/m².

4. Experimental Section

4.1. General

All experiments involving air- and/or moisture-sensitive materials were conducted under inert atmosphere using a dual vacuum/nitrogen line and standard Schlenk and glovebox techniques.[25] Nitrogen gas was provided by Air Liquide and purified by passing it through 4 Å molecular sieves. Unless stated otherwise, all reagents were purchased from commercial suppliers (e.g., Acrös, Aldrich, Fluka, Alfa Aesar) and used without further purification. All solvents used under inert atmosphere were thoroughly deoxygenated and dehydrated beforehand. They were dried and purified by refluxing over an appropriate drying agent, followed by distillation under nitrogen. The following drying agents were used: sodium/benzophenone (for toluene, THF, and diethyl ether) and calcium hydride (for n-hexane and dichloromethane). Solvents and solutions were transferred using a positive pressure of nitrogen through stainless steel cannulas, and mixtures were filtered similarly using modified cannulas that could accommodate glass fibre filter disks.

Nuclear Magnetic Resonance (NMR) spectra were collected using a Bruker Avance III 300 spectrometer operating at frequencies of 300.130 MHz (^{1}H), 75.468 MHz (^{13}C), and 96.2712 MHz (^{11}B) or on a Bruker Avance III 400 spectrometer at 400.130 MHz (^{1}H), 100.613 MHz (^{13}C) and 128.3478 (^{11}B). Deuterated solvents were dried using 4 Å molecular sieves and degassed using the freeze-pump-thaw method. The spectra were internally referenced to the residual protio solvent resonance (^{1}H) and the solvent carbon resonance (^{13}C), relative to tetramethylsilane (δ=0). External referencing was achieved using 15% $BF_3{\cdot}OEt_2$ (δ=0) for ^{11}B. Chemical shifts are reported in δ (ppm), and coupling constants are given in hertz. Multiplicities were abbreviated as follows: singlet (s), doublet (d), doublet of doublets (dd), triplet (t), triplet of doublets (td), and multiplet (m). Samples of air- and/or moisture-sensitive materials were prepared in J. Young NMR tubes within a controlled environment glovebox. Elemental analyses were obtained from the IST elemental analysis services.

The various 8-hydroxyquinolines (*i.e.* 8-quinolinols) were used without further purification, while 9-chloro-9-borafluorene (**2**)[15] and $B(C_6H_5)_3$[26] were synthesised following established procedures described in the literature.

4.2. Syntheses

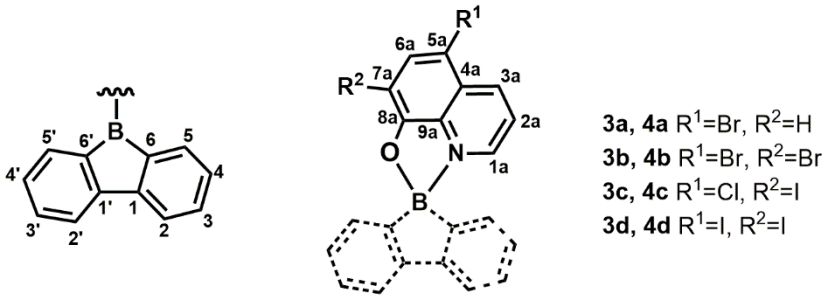

Chart 2. Labelling of protons and carbons of the 9-borafluoren-9-yl and respective 8-quinolinolato moieties used in the NMR assignments of this work.

*4.2.1. Synthesis of (κ^2N,O-5-bromo-8-quinolinolato)-9-borafluorene (**3a**)*

A solution of 5-bromo-8-hydroxyquinoline **1a** (0.22 g; 1.0 mmol), in tetrahydrofuran, was added to an excess of NaH (0.03 g; 1.5 mmol), at room temperature. The resulting yellow suspension was stirred for 2 h and added dropwise to a solution of 9-chloro-9-borafluorene (0.20 g; 1.0 mmol) also in THF, at low temperature (-80 ºC). The yellow solution was stirred overnight, under nitrogen, and allowed to slowly warm up to room temperature. The solution was filtered, and all the volatiles removed under vacuum. Yellow crystals of the desired product **3a** were obtained from a Et_2O solution stored overnight at -20 ºC. Yield, 0.25 g (65%). ^{1}H NMR (400 MHz, THF-d_8) δ 8.66 (d, $^3J_{HH}$= 8.5 Hz, 1H, H_{1a}), 8.20 (d, $^3J_{HH}$= 5.0 Hz, 1H, H_{3a}), 7.95 (d, $^3J_{HH}$= 8.2 Hz, 1H, H_{6a}), 7.84 – 7.69 (m, 1H, H_{2a}), 7.62 (d, $^3J_{HH}$= 7.6 Hz, 2H, H_5 + $H_{5'}$), 7.19 (t, $^3J_{HH}$= 7.3 Hz, 2H, H_4 + $H_{4'}$), 7.06 (d, $^3J_{HH}$= 8.2 Hz, 1H, H_{7a}), 7.02 – 6.87 (m, 4H, H_3 + H_2 + H_2' + H_3'). ^{13}C{^{1}H} NMR (101 MHz, THF-d_8): δ 161.02 (C_{8a}), 150.65 (C_6 + $C_{6'}$), 141.99 (C_{3a}), 139.35 (C_{1a}), 136.37 (C_{6a}), 130.44 (C_3 + $C_{3'}$ or C_2 + $C_{2'}$), 129.38 (C_3 + $C_{3'}$ or C_2 + $C_{2'}$), 129.05 (C_{4a}), 127.67 (C_4 + $C_{4'}$), 125.77 (C_{2a}), 120.04 (C_5 + $C_{5'}$), 110.66 (C_{7a}), 103.98 (C_{9a}), C_{5a} + C_1 + $C_{1'}$ resonances absent. ^{11}B NMR (128 MHz, THF-d_8) δ 12.9. Anal. Calcd (%) for $C_{21}H_{13}BBrNO$: C, 65.34; H, 3.39; N, 3.63. Found: C, 65.39; H, 3.23; N, 3.65.

*4.2.2. Synthesis of (κ^2N,O-5,7-dibromo-8-quinolinolato)-9-borafluorene (**3b**)*

A solution of 5,7-dibromo-8-hydroxyquinoline **1b** (0.30 g; 1.0 mmol), in tetrahydrofuran, was added to an excess of NaH (0.03 g; 1.5 mmol), at room temperature. The resulting yellow

solution was stirred for 2 h, then filtered and added dropwise to a solution of 9-chloro-9-borafluorene (0.20 g; 1.0 mmol) also in THF, at low temperature (-80 ºC). The greenish yellow solution was stirred overnight, under nitrogen, and allowed to slowly warm up to room temperature. The solution was filtered, and all the volatiles were removed under vacuum. The solid was washed with Et_2O, extracted with CH_2Cl_2 and all the volatiles were removed to obtain the desired product **3d** as a bright greenish yellow solid. Yield, 0.33 g (72%). ^{1}H NMR (400 MHz, THF-*d*$_8$) δ 8.68 (d, $^3J_{HH}$= 8.5 Hz, 1H, H_{1a}), 8.27 (d, $^3J_{HH}$= 5.3 Hz, 1H, H_{3a}), 8.16 (s, 1H, H_{6a}), 7.87 – 7.71 (m, 2H, H_{2a}), 7.63 (d, $^3J_{HH}$= 7.6 Hz, 2H, H_5 + $H_{5'}$), 7.21 (td, $^3J_{HH}$= 7.2, $^4J_{HH}$= 2.0 Hz, 2H, H_4 + $H_{4'}$), 7.06 – 6.90 (m, 4H, H_3 + H_2 + H_2' + $H_{3'}$). ^{13}C{^{1}H} NMR (101 MHz, THF-*d*$_8$): δ 150.74 (C_{8a}), 146.07 (C_6 + $C_{6'}$), 143.18 (C_{3a}), 139.92 (C_{1a}), 139.53 (C_{4a}), 138.40 (C_{6a}), 130.59 (C_3 + $C_{3'}$ or C_2 + $C_{2'}$), 129.59 (C_4 + $C_{4'}$), 128.23 (C_{5a}), 127.77 (C_3 + $C_{3'}$ or C_2 + $C_{2'}$), 125.85 (C_{2a}), 120.08 (C_5 + $C_{5'}$), 104.77 (C_{9a}), 102.10 (C_{7a}), C_1 + $C_{1'}$ resonances absent. ^{11}B NMR (128 MHz, THF-*d*$_8$) δ 11.4. Anal. Calcd (%) for $C_{21}H_{12}BBr_2NO{\cdot}0.1CH_2Cl_2$: C, 53.53; H, 2.60; N, 2.96. Found: C, 53.75; H, 2.28; N, 2.92.

*4.2.3. Synthesis of (κ^2N,O-5-chloro-7-iodo-8-quinolinolato)-9-borafluorene (**3c**)*

A solution of 5-chloro-7-iodo-8-hydroxyquinoline **1c** (0.37 g; 1.2 mmol) in tetrahydrofuran was added to an excess of NaH (0.04 g; 1.6 mmol), at room temperature. The resulting greenish black solution was stirred for 2 h, then filtered and added dropwise to a solution of 9-chloro-9-borafluorene (0.24 g; 1.2 mmol) also in THF, at low temperature (-80 ºC). The greenish yellow solution was stirred overnight, under nitrogen, and allowed to slowly warm up to room temperature. The solution was filtered, and all volatiles were removed under vacuum. The solid was washed twice with Et_2O, extracted with CH_2Cl_2 and all volatiles were removed to obtain the desired product **3c** as a bright greenish-yellow solid. Yield, 0.48 g (80%). ^{1}H NMR (300 MHz, THF-*d*$_8$) δ 8.73 (d, $^3J_{HH}$= 8.4 Hz, 1H, H_{1a}), 8.26 (d, $^3J_{HH}$= 5.1 Hz, 1H, H_{3a}), 8.11 (s, 1H, H_{6a}), 7.77 (dd, $^3J_{HH}$= 8.4 Hz, $^4J_{HH}$= 5.1 Hz, 1H, H_{2a}), 7.63 (d, $^3J_{HH}$= 7.5 Hz, 2H, H_5 + $H_{5'}$), 7.21 (td, $^3J_{HH}$= 7.5 Hz, $^4J_{HH}$=2.2 Hz, 2H, H_4 + $H_{4'}$), 7.06 – 6.91 (m, 4H, H_3 + H_2 + H_2' + $H_{3'}$). ^{13}C{^{1}H} NMR (75 MHz, THF-*d*$_8$) δ 150.62 (C_6 + $C_{6'}$), 142.91 (C_{3a}), 139.85 (C_{6a}), 137.64 (C_{1a}), 130.45 (C_3 + $C_{3'}$ or C_2 + $C_{2'}$), 129.41 (C_4 + $C_{4'}$), 127.63 (C_3 + $C_{3'}$ or C_2 + $C_{2'}$), 127.20 ($C_{2\sim4a}$), 125.50 (C_{2a}), 119.92 (C_5 + $C_{5'}$), 116.72 (C_{9a}), C_{5a} + C_{7a} + C_{8a} + C_1 + $C_{1'}$ resonance absent. ^{11}B NMR (96 MHz, THF-*d*$_8$) δ 11.67. Anal. Calcd (%) for $C_{21}H_{12}BClINO{\cdot}0.2CH_2Cl_2$: C, 52.68; H, 2.58; N, 2.90. Found: C, 52.90; H, 2.45; N, 2.90.

*4.2.4. Synthesis of (κ^2 N,O-5,7-diiodo-8-quinolinolato)-9-borafluorene (**3d**)*

A solution of 5,7-diiodo-8-hydroxyquinoline **1d** (0.47 g; 1.2 mmol), in tetrahydrofuran, was added to an excess of NaH (0.04 g; 1.6 mmol), at room temperature. The resulting greenish black solution was stirred for 2 h, then filtered and added dropwise to a solution of 9-chloro-9-borafluorene (0.24 g; 1.2 mmol) also in THF, at low temperature (-80 ºC). The greenish yellow solution was stirred overnight, under nitrogen, and allowed to slowly warm up to room temperature. The solution was filtered, and all the volatiles were removed under vacuum. The solid was washed with Et_2O, extracted with CH_2Cl_2 to obtain the desired product **3a** as a bright greenish yellow solid. Crystals suitable for X-ray diffraction studies of the desired product **3d** were obtained from Et_2O at room temperature. Yield, 0.56 g (83%). ^{1}H NMR (300 MHz, THF-d_8) δ 8.52 (d, $^3J_{HH}$= 8.4 Hz, 1H, H_{1a}), 8.46 (s, 1H, H_{6a}), 8.20 (d, $^3J_{HH}$= 5.1 Hz, 1H, H_{3a}), 7.74 (dd, $^3J_{HH}$= 8.5 Hz, $^4J_{HH}$= 5.2 Hz, 1H, H_{2a}), 7.62 (d, $^3J_{HH}$= 7.6 Hz, 2H, H_5 + $H_{5'}$), 7.20 (td, $^3J_{HH}$= 7.7 Hz, $^4J_{HH}$= 2.3 Hz, 3H, 4', 4), 7.02 – 6.91 (m, 4H, H_3 + H_2 + H_2' + $H_{3'}$). ^{13}C{^{1}H} NMR (75 MHz, THF-d_8) δ 150.63 (C_6 + $C_{6'}$), 149.36 (C_{6a}), 143.73 (C_{1a}), 142.71 (C_{3a}), 130.46 (C_3 + $C_{3'}$ or C_2 + $C_{2'}$), 129.39 (C_4 + $C_{4'}$), 127.63 (C_3 + $C_{3'}$ or C_2 + $C_{2'}$), 125.87 (C_{2a}), 119.91 (C_5 + $C_{5'}$), C_{4a} + C_{5a} + C_{7a} + C_{8a} + C_{9a} + C_1 + $C_{1'}$ resonances absent. ^{11}B NMR (96 MHz, THF-d_8) δ 11.87. Anal. Calcd (%) for $C_{21}H_{12}BI_2NO$: C, 45.13; H, 2.16; N, 2.51. Found: C, 45.28; H, <=2.00; N, 2.48.

*4.2.5. Synthesis of (κ^2N,O-5-bromo-8-quinolinolato)-diphenylboron (**4a**)*

A solution of 5-bromo-8-hydroxyquinoline **1a** (0.22 g; 1 mmol), in toluene, was added dropwise to triphenylboron (0.24 g; 1 mmol) also in toluene, at room temperature. The resulting yellow solution was heated to reflux and stirred overnight under nitrogen. On the next day, the solution was cooled down and concentrated. A yellow powder of the desired product **4a** was obtained by double layering a toluene solution with *n*-hexane, which was kept at -20 ºC. The solution was filtered, and the powder dried under vacuum. Crystals suitable for X-ray diffraction studies of the desired product were obtained from reverse vapor diffusion of a Et_2O solution onto toluene at room temperature. Yield, 0.27 g (70%). ^{1}H NMR (300 MHz, CD_2Cl_2): δ 8.70-8.57 (m, 2H, H_{1a} + H_{3a}), 7.88 (d, $^3J_{HH}$= 8.2 Hz, 1H, H_{6a}), 7.83-7.67 (m, 1H, H_{2a}), 7.48-7.32 (m, 4H, B-Ph_2-H_{ortho}), 7.33-7.16 (m, 6H, B-Ph_2-H_{meta} + B-Ph_2-H_{para}), 7.07 (d, $^3J_{HH}$= 8.2

Hz, 1H, H_{7a}). $^{13}C\{^1H\}$ NMR (75 MHz, CD_2Cl_2): δ 159.15 (C_{8a}), 140.94 (C_{1a}), 139.35 (C_{3a}), 136.12 (C_{6a}), 132.41 (B-Ph_2-C_{ortho}), 128.57 (C_{4a}), 128.15 (B-Ph_2-C_{meta}), 127.60 (B-Ph_2-C_{para}), 124.62 (C_{2a}), 110.89 (C_{7a}), 104.02 (C_{5a}), C_{9a} + B-Ph_2-C_{ipso} resonances absent. ^{11}B NMR (96.29 MHz, CD_2Cl_2): δ 12.3. Anal. Calcd (%) for $C_{21}H_{15}BBrNO$: C, 65.00; H, 3.90; N, 3.61. Found: C, 65.24; H, 3.58; N, 3.39.

*4.2.6. Synthesis of (κ^2N,O-5,7-dibromo-8-quinolinolato)-diphenylboron (**4b**)*

Complex **4b** had already been reported in the literature.[16c] Herein is described an optimised and more efficient synthetic method, at a larger preparative scale, which achieves an improved yield: A solution of 5,7-dibromo-8-hydroxyquinoline **1b** (0.30 g; 1 mmol), in toluene, was added dropwise to triphenylboron (0.24 g; 1 mmol) also in toluene, at room temperature. The resulting yellow solution was heated to reflux and stirred overnight under nitrogen. On the next day, the solution was cooled down to room temperature, concentrated and stored at -20 ºC, allowing the precipitation of a microcrystalline green solid. The supernatant solution was filtered off and the solid dried under vacuum, affording the desired compound **4b**. Crystals suitable for X-ray diffraction studies were obtained from reverse vapor diffusion of an Et_2O solution into toluene at room temperature. Yield, 0.35 g (76%). ^1H NMR (300 MHz, CD_2Cl_2): δ 8.68 (d, $^3J_{HH}$= 5.1 Hz, 1H, H_{1a}), 8.62 (d, $^3J_{HH}$= 8.5 Hz, 1H, H_{3a}), 8.05 (s, 1H, H_{6a}), 7.88 – 7.76 (m, 1H, H_{2a}), 7.49 – 7.33 (m, 4H, B-Ph_2-H_{ortho}), 7.33 – 7.13 (m, 6H, B-Ph_2-H_{meta} + B-Ph_2-H_{para}). ^{13}C $\{^1H\}$ NMR (75 MHz, CD_2Cl_2): δ 141.98 (C_{1a}), 139.85 (C_{3a}), 138.28 (C_{6a}), 132.46 (B-Ph_2-C_{ortho}), 128.24 (B-Ph_2-C_{meta}), 127.84 (B-Ph_2-C_{para}), 124.64 (C_{2a}), C_{8a} + C_{4a} + C_{5a} + C_{7a} + C_{9a} + B-Ph_2-C_{ipso} resonances absent. ^{11}B NMR (96.29 MHz, CD_2Cl_2): δ 12.4. Anal. Calcd (%) for $C_{21}H_{14}BBr_2NO$: C, 54.01; H, 3.02; N, 3.00. Found: C, 54.32; H, 2.95; N, 3.01.

*4.2.7. Synthesis of (κ^2N,O-5-chloro-7-iodo-8-quinolinolato)-diphenylboron (**4c**)*

A solution of 5-chloro-7-iodo-8-hydroxyquinoline **1c** (0.31 g; 1 mmol), in toluene, was added dropwise to triphenylboron (0.24 g; 1 mmol) also in toluene, at room temperature. The resulting yellow solution was heated to reflux and stirred overnight under nitrogen. On the next day, the solution was cooled down to room temperature, concentrated, filtered and stored at -20 ºC, allowing the precipitation of a microcrystalline yellow solid. The supernatant solution was filtered off and the solid was dried under vacuum, affording the desired product **4c**. Crystals

suitable for X-ray diffraction studies were obtained from reverse vapor diffusion of a dichloromethane solution into *n*-hexane at room temperature. Yield, 0.24 g (51%). ^{1}H NMR (300 MHz, CD_2Cl_2): δ 8.70-8.61 (m, 2H, H_{1a} + H_{3a}), 8.02 (s, 1H, H_{6a}), 7.79 (dd, $^{3}J_{HH}$= 5.1 Hz, 1H, H_{2a}), 7.45-7.22 (m, 10H, B-Ph_2-H_{ortho} + B-Ph_2-H_{meta} + B-Ph_2-H_{para}).^{13}C {^{1}H} NMR (75 MHz, CD_2Cl_2): 159.6 (C_{8a}), 141.9 (C_{1a}), 139.6 (C_{6a}), 137.7 (C_{3a}), 132.5 (B-Ph_2-C_{ortho}), 128.2 (B-Ph_2-C_{meta}), 127.8 (B-Ph_2-C_{para}), 126.9 (C_{4a}), 124.5 (C_{6a}), 116.9 (C_{5a}), C_{7a} + C_{9a} + B-Ph_2-C_{ipso} resonances absent. ^{11}B NMR (96.29 MHz, CD_2Cl_2): δ 12.6. Anal. Calcd (%) for $C_{21}H_{14}BClINO$ 0.125C_7H_8: C, 54.62; H, 3.14; N, 2.91. Found: C, 54.66; H, 2.98; N, 2.80.

*4.2.8. Synthesis of (κ^2N,O-5,7-diiodo-8-quinolinolato)-diphenylboron (**4d**)*

A solution of 5,7-diiodo-8-hydroxyquinoline **1d** (0.39 g; 1 mmol), in toluene, was added dropwise to triphenylboron (0.24 g; 1 mmol) also in toluene, at room temperature. The resulting yellow-green suspension was heated to reflux and stirred overnight under nitrogen. On the next day, the solution was cooled down to room temperature, precipitating a green solid. The suspension was further concentrated to 25% of its volume, the supernatant solution was filtered and the solid washed twice with *n*-hexane. The green solid was dried under vacuum, affording the desired compound **4d**. Crystals suitable for X-ray diffraction studies were obtained from reverse vapor diffusion of a dichloromethane solution onto *n*-hexane at room temperature. Yield, 0.44 g (79%). ^{1}H NMR (300 MHz, CD_2Cl_2): δ 8.69 (d, $^{3}J_{HH}$= 5.1 Hz, 1H, H_{1a}), 8.44 (d, $^{3}J_{HH}$= 8.1 Hz, 1H, H_{3a}), 8.37 (s, 1H, H_{6a}), 7.78 (t, $^{3}J_{HH}$= 6.0 Hz, 1H, H_{2a}), 7.38-7.30 (d, $^{3}J_{HH}$= 6.0 Hz, 4H, B-Ph_2-H_{ortho}), 7.23-7.13 (m, 6H, B-Ph_2-H_{meta} + B-Ph_2-H_{para}). ^{13}C {^{1}H} NMR (75 MHz, CD_2Cl_2): 149.1 (C_{6a}), 143.73 (C_{3a}), 142.3 (C_{1a}), 132.5 (B-Ph_2-C_{ortho}), 128.1 (B-Ph_2-C_{meta}), 127.6 (B-Ph_2-C_{para}), 125.2 (C_{2a}). C_{4a} + C_{5a} + C_{7a} + C_{8a} + C_{9a} + B-Ph_2-C_{ipso} resonances absent. ^{11}B NMR (96.29 MHz, CD_2Cl_2): δ 8.7. Anal. Calcd (%) for $C_{21}H_{14}BI_2NO$: C, 44.96; H, 2.52; N, 2.50. Found: C, 44.57; H, 2.31; N, 2.42.

4.3. X-ray data collection

The crystallographic data for complexes **3a**, **3d** and **4a**-**d** were collected using graphite monochromated Mo-Kα radiation (λ = 0.71073 Å) on a Bruker AXS-KAPPA APEX II diffractometer equipped with an Oxford Cryosystem open-flow nitrogen cryostat, at 150 K, and the crystals selected under inert atmosphere, stored in polyfluoroether oil and mounted on a

nylon loop. Cell parameters were retrieved using Bruker SMART software and refined using Bruker SAINT on all observed reflections. Absorption corrections were applied using SADABS.[27] Structure solution and refinement were performed using direct methods in SIR2004,[28] SIR2014[29] and SHELXL[30] programmes included in the WINGX-Version2014.1 software package.[31] All hydrogen atoms were inserted in idealised positions and allowed to refine riding on the parent carbon atom, with C-H distances of 0.95 Å for aromatic H atoms and with $U_{iso}(H) = 1.2U_{eq}(C)$. Graphic presentations were prepared with ORTEP-3.[31] The CIF file corresponding to the molecular structure of complex **3a** presented A-level alerts, which were associated with a low ratio of observed to unique reflections, due to the poor diffracting power/lack of unique data of the crystal and the corresponding data. Nevertheless, it was possible to undoubtedly solve the molecular structure. Data was deposited in CCDC under the deposit numbers 2325491for **3a**, 2325492 for **3d**, 2325493 for **4a**, 2325494 for **4b**, 2325495 for **4c** and 2325496 for **4d**.

4.4. Computational Studies

The Density Functional Theory calculations[13] were performed using the Amsterdam Density Functional program package (ADF),[19] with the Vosko-Wilk-Nusair [32] Local Density Approximation of the correlation energy and the PBE0 functional,[33,34] considering solvent effects (THF) according to the COSMO model implemented in ADF. Relativistic effects were described with the ZORA approximation.[35] Triple ζ Slater-type orbitals (STO) were used to describe all the electrons of H, C, B, N, Cl and I, augmented with one set of polarisation functions (ADF TZP basis set). The geometries of complexes **3a-d** and **4a-d** were modelled after those described above (Section 2.2) and optimised without symmetry constraints. TDDFT[14] methods were performed to optimise the geometries of the first excited singlet and triplet states and, including spin orbit coupling (SOPERT)[22] and the Tamm-Dancoff approximation (TDA),[36] to obtain the absorption spectra. Unrestricted calculations were carried out for open shell complexes. The calculated fluorescence rate constants were the reciprocal of the excited singlet state lifetimes obtained from the SOPERT calculations (SO).

In order to compare the results of this work with those of our previous ones,[12d,23,37] as well as to probe the role of functional and dispersion, the calculations described above (model A) were repeated with the Grimme D3 correction[38] (A/D3), with the B3LYP functional[39] (method B), and B3LYP with the Grimme D3 correction (B/D3), with the TZP basis set. Another older approach used the Becke's exchange[40] and Perdew's[41] correlation functionals, with a TZ2P

basis set (two sets of polarization functions) and a small core in the gas-phase (GP). The structure obtained in these conditions was used to calculate the energy of the HOMO and LUMO in THF and dichloromethane (DCM) with COSMO. The first singlet excited states were obtained by promotion of one electron from the HOMO to the LUMO, with the same spin (T_1) or opposite spins (S_1) followed by geometry optimisation. The results from these calculations are presented in the SM. Structures and orbitals were visualised with Chemcraft.[42]

4.5. Spectroscopic measurements

4.5.1. Samples preparation and Absorption and Luminescence Measurements

Solutions of all complexes in THF with optical density (OD) < 0.2 ($c < 8\times10^{-5}$ M) were used. For solid state measurements, toluene solutions of each boron complex (concentration of 1 mg/mL) and ZEONEX® 480R (concentration of 100 mg/mL), in toluene, were combined on a and drop-casted (~80 μL) at 30 ºC on quartz slides to form thin films by evaporation of the solvent under nitrogen atmosphere.

Absorption and fluorescence spectra of **3a-d** and **4a-d** in solution and solid state were measured with an Agilent Cary 8454 UV-Visible spectrophotometer and a SPEX Fluorolog 212I, respectively. The fluorescence spectra were collected with right angle geometry, in the S/R mode, and corrected for instrumental wavelength dependence. Fluorescence quantum yields of the compound in THF solution were determined by comparison with the quantum yields of α-pentathiophene in dioxane at 25 ºC. The phosphorescence spectra were obtained in a SPEX 1934D phosphorimeter using a 50 μs of delay upon excitation and a time window of 10 ms. The spectra were measured at 77 K using degassed 2-Me-THF as solvent, under complete inert conditions without the presence of molecular oxygen.

4.5.2 Absolute Fluorescence Emission Quantum Yields Measurements

An integrating sphere for absolute measurements was used to obtain the values for the fluorescence emission quantum yields (Φ_f) of the solid powdered samples, as recommended by the EPA.[43] A NIST calibration lamp was used to compute the correction curve of the integrating sphere/detection system. This is of utmost importance, for the correct calculation of fluorescence quantum yields, Φ_f. A 355 nm continuous laser (LaserTechnic, 10mW) was used as the excitation source and neutral density filters to attenuate the excitation light whenever

needed. The signals were collected from the integrating sphere by a collimating beam probe coupled to an optical fibre (fused silica), in this way assuring the connection to the monochromator entrance. A fixed monochromator (Andor, Shamrock 163) coupled to an ICCD detector (Andor, i-Star 720) with time gate capabilities was used in the accumulation mode.

The absolute fluorescence quantum yields were obtained using the following equation:

$$\Phi_f = (P_c - (1 - A) \times P_b) / A \times L_a \quad \text{with } A = (1 - L_c / L_b),$$

where A is the absorption coefficient, P_b is the light emitted by the sample after absorption of scattered excitation light, P_c is the light emitted by the sample after absorption of total laser light, L_a is the total amount of excitation laser light, L_b is the scattered laser light, and L_c is excitation light spectrum.

In many cases P_b is negligible and the equation simply becomes:

$$\Phi_f = P_c / (L_a - L_c)$$

Using this methodology, the Φ_f determinations of several standard fluorophores with a known quantum yield were performed for validation purposes. The agreement found between the Φ_f obtained by the absolute method and the reported literature values validate the photoluminescence quantum yields determined by this absolute approach.

4.5.3. Fluorescence Lifetime determinations

Fluorescence lifetimes were determined using Easylife VTM equipment from OBB corporation (Birmingham, NJ, USA), lifetime range from 100 ps to 3 μs. This technique uses pulsed light sources from different LEDs (365 nm in this case) and measures fluorescence intensity at different time delays after the excitation pulse. In this case, 490 nm cut-off filters were used at emission both for solution and for solid samples, depending on the sample under study. The instrument response function was measured using a Ludox scattering solution. FelixGX software from OBB was used for fitting and analysis of the decay dynamics, 1 to 4 exponentials and also a lifetime distribution analysis,[43b,44] the Exponential Series Method (ESM).

4.5.4. Transient Emission Spectroscopy (TRS EMI)

The transient emission measurements were performed using as excitation source a pulsed N_2 laser at 337 nm (OBB, model 4500 with ~1mJ per pulse). A fixed monochromator (Andor, Shemrock 163) coupled to an ICCD detector (Andor, i-Star 720) with time gate capabilities and

in the kinetics mode, were used to detect the fluorescence, delayed fluorescence or phosphorescence signals. The available detection ranges from 200 to 900 nm. The signals were collected by a collimating beam probe coupled to an optical fibre (fused silica) assuring in this way the connection to the monochromator entrance. The TRS EMI spectra of all compounds under study (ZEONEX 480 films), were acquired in a short time or long time domains using suitable gate widths and start delay, as provided by the ICCD (with a minimum temporal gate of 2.2 ns and with 1024×128 pixels for the whole spectral range).

Further details of the use of this time resolved emission spectroscopic technique can be found in ref. 43.

4.6. Organic light-emitting diodes

OLEDs were fabricated by vacuum thermal evaporation using indium-tin-oxide (ITO) coated glass substrates with a sheet resistance of 20 Ω/sq and ITO thickness of 100 nm. The substrates were first washed with water, acetone and then sonicated in acetone and isopropanol for 15 min. Substrates were dried with compressed air and transferred into an oxygen-plasma generator for 6 min at full power. Thermally deposited layers were obtained using a Kurt J. Lesker Spectros II deposition system at 10^{-6} mbar base pressure. All organic materials and aluminium were deposited at a rate of 1 Å s^{-1}. The LiF layer was deposited at a rate of 0.1–0.2 Å s^{-1}. Characterisation of OLED devices was conducted in a 10-inch integrating sphere (Labsphere) connected to a Source Measure Unit (SMU, Keithley) and coupled with a USB4000 spectrometer (Ocean Optics). Further details are available in ref. 45. Devices with 4×2 mm pixel size were fabricated.

Substances used for OLED fabrication have been purchased from suppliers indicated in parentheses: HAT-CN – dipyrazino[2,3-f:2',3'-h]quinoxaline-2,3,6,7,10,11-hexacarbonitrile (sublimed, LUMTEC); TSBPA – 4,4'-(diphenylsilanediyl)bis(*N*,*N*-diphenylaniline) (LUMTEC); mCP – 1,3-bis(carbazol-9-yl)benzene (sublimed, LUMTEC); PO-T2T – 2,4,6-tris[3-(diphenylphosphinyl)phenyl]-1,3,5-triazine (LUMTEC); TPBi – 1,3,5-tris(1-phenyl-1*H*-benzimidazol-2-yl)benzene, (sublimed, LUMTEC); LiF (99.995%, Sigma Aldrich); Al pellets (99.9995%, Lesker).

The fully thermally deposited OLEDs comprised hole injection layer: HAT-CN, hole transport layer: TSBPA, exciton blocking layer: mCP, hole blocking layer: PO-T2T and electron transport layer: TPBi, electron injection layer: LiF and cathode: Al. mCP served as the host material in the emissive layer.

CRediT authorship contribution statement

Carina B. Fialho: Investigation, Data Curation, Methodology, Validation, Writing – original draft. **Tiago F. C. Cruz:** Investigation, Data Curation, Methodology, Validation, Writing – original draft. **Maria José Calhorda:** Investigation, Data Curation, Methodology, Validation, Writing – original draft. **Luís F. Vieira Ferreira:** Investigation, Data Curation, Methodology, Supervision, Validation, Writing – review & editing. **Piotr Pander:** Investigation, Data Curation, Methodology, Validation, Writing – original draft. **Fernando B. Dias:** Methodology, Supervision, Validation, Writing – original draft, Writing – review & editing. **António L. Maçanita:** Data Curation, Methodology, Validation. **Pedro T. Gomes:** Conceptualization, Methodology, Project administration, Supervision, Validation, Writing – original draft, Writing – review & editing.

Declaration of competing interest

The authors declare the following financial interests/personal relationships which may be considered as potential competing interests: Pedro T. Gomes reports financial support was provided by Foundation for Science and Technology. Maria Jose Calhorda reports financial support was provided by Foundation for Science and Technology (FCT), Portugal. Luis F. Vieira Ferreira reports financial support was provided by Foundation for Science and Technology (FCT), Portugal. Carina B. Fialho reports financial support was provided by Foundation for Science and Technology (FCT), Portugal. Tiago F. C. Cruz reports financial support was provided by Foundation for Science and Technology (FCT), Portugal. If there are other authors, they declare that they have no known competing financial interests or personal relationships that could have appeared to influence the work reported in this paper.

Data Availability

The data that support the findings of this study are available in the supplementary material of this article. The supplementary crystallographic data for the complexes **3a**, **3d**, **4a**, **4b**, **4c**,

and **4d** have been registered with 2325491, 2325492, 2325493, 2325494, 2325495, and 2325496, respectively. These data are available free of charge on http://www.ccdc.cam.ac.uk/data_request/cif, or via emailing data_request@ccdc.cam.ac.uk, or by contacting The Cambridge Crystallographic Data Centre, 12 Union Road, Cambridge CB2 1EZ, UK; fax: +441223 336033.

Acknowledgements

We thank the Fundação para a Ciência e a Tecnologia (FCT) for financial support (Project PTDC/QUI-QIN/31585/2017) and for a fellowship to C.B.F. (2021.05622.BD). Centro de Química Estrutural (CQE) and Institute of Molecular Sciences (IMS), BioISI – Biosystems & Integrative Sciences Institute, and IBB-Institute for Bioengineering and Biosciences acknowledge the FCT for financial support (respectively: Projects UIDB/00100/2020 (https://doi.org/10.54499/UIDB/00100/2020), UIDP/00100/2020 (https://doi.org/10.54499/UIDP/00100/2020) and LA/P/0056/2020 (https://doi.org/10.54499/LA/P/0056/2020); UIDB/04046/2020 (https://doi.org/10.54499/UIDB/04046/2020) and UIDP/04046/2020 (https://doi.org/10.54499/UIDP/04046/2020); and UIDB/04565/2020 (https://doi.org/10.54499/UIDB/04565/2020)).

References

1 (a) Baldo MA, O'Brien DF, You Y, Shoustikov A, Sibley S, Thompson ME, et al. Highly efficient phosphorescent emission from organic electroluminescent devices. Nat 1998;395:151–4. https://doi.org/10.1038/25954. (b) Adachi C, Sandanayaka ASD. The Leap from Organic Light-Emitting Diodes to Organic Semiconductor Laser Diodes. CCS Chem 2020;2:1203–16. https://doi.org/10.31635/ccschem.020.202000327.

2 (a) Baldo MA, Lamansky S, Burrows PE, Thompson ME, Forrest SR. Very high-efficiency green organic light-emitting devices based on electrophosphorescence. Appl Phys Lett 1999;75:4–6. https://doi.org/10.1063/1.124258. (b) Adachi C, Baldo MA, Thompson ME, Forrest SR. Nearly 100% internal phosphorescence efficiency in an organic light-emitting device. J Appl Phys 2001;90:5048–51. https://doi.org/10.1063/1.1409582. (c) Sajoto T,

Djurovich PI, Tamayo A, Yousufuddin M, Bau R, Thompson ME, et al. Blue and Near-UV Phosphorescence from Iridium Complexes with Cyclometalated Pyrazolyl or N -Heterocyclic Carbene Ligands. Inorg Chem 2005;44:7992–8003. https://doi.org/10.1021/ic051296i. (d) Li G, Congrave DG, Zhu D, Su Z, Bryce MR. Recent advances in luminescent dinuclear iridium(III) complexes and their application in organic electroluminescent devices. Polyhedron 2018;140:146–57. https://doi.org/10.1016/j.poly.2017.11.029. (e) Tuong Ly K, Chen-Cheng R-W, Lin H-W, Shiau Y-J, Liu S-H, Chou P-T, et al. Near-infrared organic light-emitting diodes with very high external quantum efficiency and radiance. Nat Photonics 2017;11:63–8. https://doi.org/10.1038/nphoton.2016.230. (f) Amouri H. Luminescent Complexes of Platinum, Iridium, and Coinage Metals Containing N -Heterocyclic Carbene Ligands: Design, Structural Diversity, and Photophysical Properties. Chem Rev 2023;123:230–70. https://doi.org/10.1021/acs.chemrev.2c00206.

3 Itagaki H, Fluorescence Spectroscopy. *In* Tanaka T (Ed.), *Experimental Methods in Polymer Science: modern methods in polymer research*, San Diego: Academic Press; 2000, p. 155-260.

4 (a) Nakagawa T, Ku S-Y, Wong K-T, Adachi C. Electroluminescence based on thermally activated delayed fluorescence generated by a spirobifluorene donor–acceptor structure. Chem Commun 2012;48:9580. https://doi.org/10.1039/c2cc31468a. (b) Uoyama H, Goushi K, Shizu K, Nomura H, Adachi C. Highly efficient organic light-emitting diodes from delayed fluorescence. Nat 2012;492:234–8. https://doi.org/10.1038/nature11687. (c) Zhang Q, Li J, Shizu K, Huang S, Hirata S, Miyazaki H, et al. Design of Efficient Thermally Activated Delayed Fluorescence Materials for Pure Blue Organic Light Emitting Diodes. J Am Chem Soc 2012;134:14706–9. https://doi.org/10.1021/ja306538w. (d) Li J, Nakagawa T, MacDonald J, Zhang Q, Nomura H, Miyazaki H, et al. Highly Efficient Organic Light-Emitting Diode Based on a Hidden Thermally Activated Delayed Fluorescence Channel in a Heptazine Derivative. Adv Mater 2013;25:3319–23. https://doi.org/10.1002/adma.201300575. (e) Youn Lee S, Yasuda T, Nomura H, Adachi C. High-efficiency organic light-emitting diodes utilizing thermally activated delayed fluorescence from triazine-based donor–acceptor hybrid molecules. Appl Phys Lett 2012;101:093306. https://doi.org/10.1063/1.4749285. (f) Wu T-L, Huang M-J, Lin C-C, Huang P-Y, Chou T-Y, Chen-Cheng R-W, et al. Diboron compound-based organic light-emitting diodes with high efficiency and reduced efficiency roll-off. Nat Photonics 2018;12:235–40. https://doi.org/10.1038/s41566-018-0112-9. (g) Zeng W, Lai H, Lee W,

Jiao M, Shiu Y, Zhong C, et al. Achieving Nearly 30% External Quantum Efficiency for Orange–Red Organic Light Emitting Diodes by Employing Thermally Activated Delayed Fluorescence Emitters Composed of 1,8-Naphthalimide-Acridine Hybrids. Adv Mater 2018;30:1704961. https://doi.org/10.1002/adma.201704961. (h) Lin T, Chatterjee T, Tsai W, Lee W, Wu M, Jiao M, et al. Sky-Blue Organic Light Emitting Diode with 37% External Quantum Efficiency Using Thermally Activated Delayed Fluorescence from Spiroacridine-Triazine Hybrid. Adv Mater 2016;28:6976–83. https://doi.org/10.1002/adma.201601675. (i) Chen Y, Zhang D, Zhang Y, Zeng X, Huang T, Liu Z, et al. Approaching Nearly 40% External Quantum Efficiency in Organic Light Emitting Diodes Utilizing a Green Thermally Activated Delayed Fluorescence Emitter with an Extended Linear Donor–Acceptor–Donor Structure. Adv Mater 2021;33:2103293. https://doi.org/10.1002/adma.202103293. (j) Chen Y, Jayakumar J, Hsieh C, Wu T, Liao C, Pandidurai J, et al. Triarylamine-Pyridine-Carbonitriles for Organic Light-Emitting Devices with EQE Nearly 40%. Adv Mater 2021;33:2008032. https://doi.org/10.1002/adma.202008032.

5 (a) Sternlicht H, Nieman GC, Robinson GW. Triplet—Triplet Annihilation and Delayed Fluorescence in Molecular Aggregates. J Chem Phys 1963;38:1326–35. https://doi.org/10.1063/1.1733853; (b) Yang Z, Mao Z, Xie Z, Zhang Y, Liu S, Zhao J, et al. Recent advances in organic thermally activated delayed fluorescence materials. Chem Soc Rev 2017;46:915–1016. https://doi.org/10.1039/C6CS00368K; (c) Chitraningrum N, Chu T-Y, Huang P-T, Wen T-C, Guo T-F. The triplet-triplet annihilation process of triplet to singlet excitons to fluorescence in polymer light-emitting diodes. Org Electron 2018;62:505–10. https://doi.org/10.1016/j.orgel.2018.06.021.

6 (a) Penfold TJ, Dias FB, Monkman AP. The theory of thermally activated delayed fluorescence for organic light emitting diodes. Chem Commun 2018;54:3926–35. https://doi.org/10.1039/C7CC09612G. (b) Santos PL, Ward JS, Data P, Batsanov AS, Bryce MR, Dias FB, et al. Engineering the singlet–triplet energy splitting in a TADF molecule. J Mater Chem C 2016;4:3815–24. https://doi.org/10.1039/C5TC03849A; (c) Dias FB, Penfold TJ, Monkman AP. Photophysics of thermally activated delayed fluorescence molecules. Methods Appl Fluoresc 2017;5:012001. https://doi.org/10.1088/2050-6120/aa537e. (d) Endo A, Ogasawara M, Takahashi A, Yokoyama D, Kato Y, Adachi C. Thermally Activated Delayed Fluorescence from Sn 4^{+} –Porphyrin Complexes and Their Application to Organic Light Emitting Diodes — A Novel Mechanism for Electroluminescence. Adv Mater 2009;21:4802–6.

https://doi.org/10.1002/adma.200900983. (e) Gibson J, Monkman AP, Penfold TJ. The Importance of Vibronic Coupling for Efficient Reverse Intersystem Crossing in Thermally Activated Delayed Fluorescence Molecules. ChemPhysChem 2016;17:2956–61. https://doi.org/10.1002/cphc.201600662.

7 (a) Hu J, Pu Y, Satoh F, Kawata S, Katagiri H, Sasabe H, et al. Bisanthracene‐Based Donor‐Acceptor‐type Light‐Emitting Dopants: Highly Efficient Deep‐Blue Emission in Organic Light‐Emitting Devices. Adv Funct Mater 2014;24:2064–71. https://doi.org/10.1002/adfm.201302907. (b) Peng L, Yao J-W, Wang M, Wang L-Y, Huang X-L, Wei X-F, et al. Efficient soluble deep blue electroluminescent dianthracenylphenylene emitters with CIE y ($y \leq 0.08$) based on triplet-triplet annihilation. Sci Bull (Beijing) 2019;64:774–81. https://doi.org/10.1016/j.scib.2019.04.029. (c) Liu W, Ying S, Guo R, Qiao X, Leng P, Zhang Q, et al. Nondoped blue fluorescent organic light-emitting diodes based on benzonitrile-anthracene derivative with 10.06% external quantum efficiency and low efficiency roll-off. J Mater Chem C 2019;7:1014–21. https://doi.org/10.1039/C8TC05707A. (d) Huh J-S, Ha YH, Kwon S-K, Kim Y-H, Kim J-J. Design Strategy of Anthracene-Based Fluorophores toward High-Efficiency Deep Blue Organic Light-Emitting Diodes Utilizing Triplet–Triplet Fusion. ACS Appl Mater Interfaces 2020;12:15422–9. https://doi.org/10.1021/acsami.9b21143. (e) Cao C, Yang G-X, Tan J-H, Shen D, Chen W-C, Chen J-X, et al. Deep-blue high-efficiency triplet-triplet annihilation organic light-emitting diodes using donor- and acceptor-modified anthracene fluorescent emitters. Mater Today Energy 2021;21:100727. https://doi.org/10.1016/j.mtener.2021.100727. (f) Li W, Chasing P, Nalaoh P, Chawanpunyawat T, Chantanop N, Sukpattanacharoen C, et al. Deep-blue high-efficiency triplet–triplet annihilation organic light-emitting diodes using hydroxyl-substituted tetraphenylimidazole-functionalized anthracene fluorescent emitters. J Mater Chem C 2022;10:9968–79. https://doi.org/10.1039/D2TC01406H. (g) Chen C-H, Li Y-S, Fang S-C, Lin B-Y, Li C-Y, Liao Y-C, et al. High‐Performance Deep‐Blue OLEDs Harnessing Triplet‐Triplet Annihilation Under Low Dopant Concentration. Adv Photonics Res 2023;4. https://doi.org/10.1002/adpr.202200204.

8 (a) Chen Y-H, Lin C-C, Huang M-J, Hung K, Wu Y-C, Lin W-C, et al. Superior upconversion fluorescence dopants for highly efficient deep-blue electroluminescent devices. Chem Sci 2016;7:4044–51. https://doi.org/10.1039/C6SC00100A. (b) Shan T, Gao Z, Tang X, He X, Gao Y, Li J, et al. Highly efficient and stable pure blue nondoped

organic light-emitting diodes at high luminance based on phenanthroimidazole-pyrene derivative enabled by triplei-triplet annihilation. Dyes Pigments 2017;142:189–97. https://doi.org/10.1016/j.dyepig.2017.03.032. (c) Ding Z, Ma B, Zhou Z, Zhang S, Pan J, Zhu W, et al. Efficient solution-processed OLEDs featuring deep-blue triplet-triplet annihilation emitter based on pyrene derivative. Dyes Pigments 2023;216:111346. https://doi.org/10.1016/j.dyepig.2023.111346.

9 (a) Zheng X, Peng Q, Lin J, Wang Y, Zhou J, Jiao Y, et al. Simultaneous harvesting of triplet excitons in OLEDs by both guest and host materials with an intramolecular charge-transfer feature via triplet–triplet annihilation. J Mater Chem C 2015;3:6970–8. https://doi.org/10.1039/C5TC00779H. (b) Tang X, Liu H, Xu L, Xu X, He X, Liu F, et al. Achieving High Efficiency at High Luminance in Fluorescent Organic Light‐Emitting Diodes through Triplet‐Triplet Fusion Based on Phenanthroimidazole‐Benzothiadiazole Derivatives. Chem Eur J 2021;27:13828–39. https://doi.org/10.1002/chem.202102136. (c) Sk B, Thangaraji V, Yadav N, Nanda GP, Das S, Gandeepan P, et al. High performance non-doped green organic light emitting diodes via delayed fluorescence. J Mater Chem C 2021;9:15583–90. https://doi.org/10.1039/D1TC03849D.

10 (a) Mellerup SK, Wang S. Boron-Doped Molecules for Optoelectronics. Trends Chem 2019;1:77–89. https://doi.org/10.1016/j.trechm.2019.01.003; (b) Kothavale SS, Lee JY. Three‐ and Four‐Coordinate, Boron‐Based, Thermally Activated Delayed Fluorescent Emitters. Adv Opt Mater 2020;8:2000922. https://doi.org/10.1002/adom.202000922. (c) Lee H, Karthik D, Lampande R, Ryu JH, Kwon JH. Recent Advancement in Boron-Based Efficient and Pure Blue Thermally Activated Delayed Fluorescence Materials for Organic Light-Emitting Diodes. Front Chem 2020;8:373. https://doi.org/10.3389/fchem.2020.00373. (d) Murali AC, Nayak P, Venkatasubbaiah K. Recent advances in the synthesis of luminescent tetra-coordinated boron compounds. Dalton Trans 2022;51:5751–71. https://doi.org/10.1039/D2DT00160H.

11 (a) Bell BM, Clark TP, De Vries TS, Lai Y, Laitar DS, Gallagher TJ, et al. Boron-based TADF emitters with improved OLED device efficiency roll-off and long lifetime. Dyes Pigments 2017;141:83–92. https://doi.org/10.1016/j.dyepig.2017.01.055. (b) Shiu Y-J, Chen Y-T, Lee W-K, Wu C-C, Lin T-C, Liu S-H, et al. Efficient thermally activated delayed fluorescence of functional phenylpyridinato boron complexes and high performance organic light-emitting diodes. J Mater Chem C 2017;5:1452–62. https://doi.org/10.1039/C6TC04994J. (c) Stanoppi M, Lorbach A. Boron-based donor-

spiro-acceptor compounds exhibiting thermally activated delayed fluorescence (TADF). Dalton Trans 2018;47:10394–8. https://doi.org/10.1039/C8DT01255E. (d) Li P, Chan H, Lai S, Ng M, Chan M, Yam VW. Four‐Coordinate Boron Emitters with Tridentate Chelating Ligand for Efficient and Stable Thermally Activated Delayed Fluorescence Organic Light‐Emitting Devices. Angew Chem Int Ed 2019;58:9088–94. https://doi.org/10.1002/anie.201903332. (e) Zhang H, Chen P-Z, Niu L-Y, Yang Q-Z. A difluoroboron β-diketonate-based luminescent material with tunable solid-state emission and thermally activated delayed fluorescence. Mater Chem Front 2020;4:285–91. https://doi.org/10.1039/C9QM00672A. (f) Urban M, Marek-Urban PH, Durka K, Luliński L, Pander P, Monkman AP. TADF Invariant of Host Polarity and Ultralong Fluorescence Lifetimes in a Donor-Acceptor Emitter Featuring a Hybrid Sulfone-Triarylboron Acceptor. Angew Chem Int Ed 2023;62: e202217530. https://doi.org/10.1002/anie.202217530.

12 (a) Singh-Rachford TN, Haefele A, Ziessel R, Castellano FN. Boron Dipyrromethene Chromophores: Next Generation Triplet Acceptors/Annihilators for Low Power Upconversion Schemes. J Am Chem Soc 2008;130:16164–5. https://doi.org/10.1021/ja807056a. (b) Deng F, Francis AJ, Weare WW, Castellano FN. Photochemical upconversion and triplet annihilation limit from a boron dipyrromethene emitter. Photochem Photobiol Sci 2015;14:1265–70. https://doi.org/10.1039/c5pp00106d. (c) Li J, Zhang M, Zeng L, Huang L, Wang X. NIR‐Absorbing B,N‐Heteroarene as Photosensitizer for High‐Performance NIR‐to‐Blue Triplet‐Triplet Annihilation Upconversion. Angew Chem Int Ed 2023;62:e20230309. https://doi.org/10.1002/anie.202303093. (d) Fialho CB, Cruz TFC, Rodrigues AI, Calhorda MJ, Vieira Ferreira LF, Pander P, et al. 9-Borafluoren-9-yl and diphenylboron tetracoordinate complexes of F- and Cl-substituted 8-quinolinolato ligands: synthesis, molecular and electronic structures, fluorescence and application in OLED devices. Dalton Trans 2023;52:4933–53. https://doi.org/10.1039/D3DT00496A.

13 Parr RG, Yang W. Density Functional Theory of Atoms and Molecule. New York: Oxford University Press; 1989.

14 (a) van Gisbergen SJA, Groeneveld JA, Rosa A, Snijders JG, Baerends EJ. Excitation Energies for Transition Metal Compounds from Time-Dependent Density Functional Theory. Applications to MnO_4^-, $Ni(CO)_4$, and $Mn_2(CO)_{10}$. J Phys Chem A 1999;103:6835–44. https://doi.org/10.1021/jp991060y. (b) Gray HB, Beach NA. The Electronic Structures of Octahedral Metal Complexes. I. Metal Hexacarbonyls and Hexacyanides. J Am Chem

Soc 1963;85:2922–7. https://doi.org/10.1021/ja00902a014. (c) van Gisbergen SJA, Rosa A, Ricciardi G, Baerends EJ. Time-dependent density functional calculations on the electronic absorption spectrum of free base porphin. J Chem Phys 1999;111:2499–506. https://doi.org/10.1063/1.479617. (d) van Gisbergen SJA, Snijders JG, Baerends EJ. Implementation of time-dependent density functional response equations. Comput Phys Commun 1999;118:119–38. https://doi.org/10.1016/S0010-4655(99)00187-3. (e) Damas A, Ventura B, Moussa J, Esposti AD, Chamoreau L-M, Barbieri A, et al. Turning on Red and Near-Infrared Phosphorescence in Octahedral Complexes with Metalated Quinones. Inorg Chem 2012;51:1739–50. https://doi.org/10.1021/ic202021w.

15 (a) Herrmann WA. Synthetic Methods of Organometallic and Inorganic Chemistry, Volume 10. New York: Georg Thieme Verlag Stuttgart; 2002. (b) Biswas S, Oppel IM, Bettinger HF. Synthesis and Structural Characterization of 9-Azido-9-Borafluorene: Monomer and Cyclotrimer of a Borole Azide. Inorg Chem 2010;49:4499–506. https://doi.org/10.1021/ic902436s.

16 (a) DeYoung E. Notes- Even-Numbered n-Acyl and n-Alkyl Ferrocenes. J Org Chem 1961;26:1312–1312. https://doi.org/10.1021/jo01063a618. (b) Wu Q, Esteghamatian M, Hu N-X, Popovic Z, Enright G, Tao Y, et al. Synthesis, Structure, and Electroluminescence of BR 2 q (R = Et, Ph, 2-Naphthyl and q = 8-Hydroxyquinolato). Chem Mater 2000;12:79–83. https://doi.org/10.1021/cm990372a. (c) Kappaun S, Rentenberger S, Pogantsch A, Zojer E, Mereiter K, Trimmel G, et al. Organoboron Quinolinolates with Extended Conjugated Chromophores: Synthesis, Structure, and Electronic and Electroluminescent Properties. Chem Mater 2006;18:3539–47. https://doi.org/10.1021/cm060720q. (d) Urban M, Durka K, Górka P, Wiosna-Sałyga G, Nawara K, Jankowski P, et al. The effect of locking π-conjugation in organoboron moieties in the structures of luminescent tetracoordinate boron complexes. Dalton Trans 2019;48:8642–63. https://doi.org/10.1039/C9DT01332F.

17 (a) Hudson ZM, Wang S. Impact of Donor−Acceptor Geometry and Metal Chelation on Photophysical Properties and Applications of Triarylboranes. Acc Chem Res 2009;42:1584–96. https://doi.org/10.1021/ar900072u. (b) Chen P, Lalancette RA, Jäkle F. π‐Expanded Borazine: An Ambipolar Conjugated B‐π‐N Macrocycle. Angew Chem Int Ed 2012;51:7994–8. https://doi.org/10.1002/anie.201203788. (c) Halik M, Wenseleers W, Grasso C, Stellacci F, Zojer E, Barlow S, et al. Bis(dioxaborine) compounds with large two-photon cross sections, and their use in the photodeposition of silver. Chem Commun 2003:1490–1. https://doi.org/10.1039/B303135G. (d) Entwistle CD, Marder TB.

Applications of Three-Coordinate Organoboron Compounds and Polymers in Optoelectronics. Chem Mater 2004;16:4574–85. https://doi.org/10.1021/cm0495717. (e) Entwistle CD, Marder TB. Boron chemistry lights the way: optical properties of molecular and polymeric systems. Angew Chem Int Ed Engl 2002;41:2927–31. https://doi.org/10.1002/1521-3773(20020816)41:16<2927::AID-ANIE2927>3.0.CO;2-L. (f) Bernard R, Cornu D, Scharff J-P, Chiriac R, Miele P, Baldeck PL, et al. Synthesis, Characterization, and UV−vis Linear Absorption of Centrosymmetric π-Systems Incorporating c loso -Dodecaborate Clusters. Inorg Chem 2006;45:8743–8. https://doi.org/10.1021/ic060563x. (g) Bernard R, Cornu D, Baldeck PL, Čáslavský J, Létoffé J-M, Scharff J-P, et al. Synthesis, characterization and optical properties of π-conjugated systems incorporating closo-dodecaborate clusters: new potential candidates for two-photon absorption processes. Dalton Trans 2005:3065–71. https://doi.org/10.1039/b504414f. (h) Jäkle F. Advances in the Synthesis of Organoborane Polymers for Optical, Electronic, and Sensory Applications. Chem Rev 2010;110:3985–4022. https://doi.org/10.1021/cr100026f.

18 (a) Höpfl H, Barba V, Vargas G, Farfan N, Santillan R, Castillo D. X-ray crystallographic study of three (N → B)-borinates prepared from 8-hydroxyquinoline and 2-hydroxypyridine. Chem Heterocycl Compd (N Y) 1999;35:912–27. https://doi.org/10.1007/BF02252159. (b) Wu Q, Esteghamatian M, Hu N-X, Popovic Z, Enright G, Tao Y, et al. Synthesis, Structure, and Electroluminescence of BR 2 q (R = Et, Ph, 2-Naphthyl and q = 8-Hydroxyquinolato). Chem Mater 2000;12:79–83. https://doi.org/10.1021/cm990372a. (c) Cui Y, Liu Q-D, Bai D-R, Jia W-L, Tao Y, Wang S. Organoboron Compounds with an 8-Hydroxyquinolato Chelate and Its Derivatives: Substituent Effects on Structures and Luminescence. Inorg Chem 2005;44:601–9. https://doi.org/10.1021/ic0489746.

19 (a) te Velde G, Bickelhaupt FM, Baerends EJ, Fonseca Guerra C, van Gisbergen SJA, Snijders JG, et al. Chemistry with ADF. J Comput Chem 2001;22:931–67. https://doi.org/10.1002/jcc.1056. (b) Fonseca Guerra C, Snijders JG, te Velde G, Baerends EJ. Towards an order- N DFT method. Theor Chem Acc 1998;99:391–403. https://doi.org/10.1007/s002140050353. (c) ADF2013, SCM, Theoretical Chemistry, Vrije Universiteit, Amsterdam, The Netherlands, http://www.scm.com (last accessed on 08 February 2024).

20 Ernzerhof M, Scuseria GE. Assessment of the Perdew–Burke–Ernzerhof exchange-correlation functional. J Chem Phys 1999;110:5029–36. https://doi.org/10.1063/1.478401.

21 Adamo C, Barone V. Toward reliable density functional methods without adjustable parameters: The PBE0 model. J Chem Phys 1999;110:6158–70. https://doi.org/10.1063/1.478522.

22 Wang F, Ziegler T. A simplified relativistic time-dependent density-functional theory formalism for the calculations of excitation energies including spin-orbit coupling effect. J Chem Phys 2005;123:154102. https://doi.org/10.1063/1.2061187.

23 Rodrigues AI, Krishnamoorthy P, Gomes CSB, Carmona N, Di Paolo RE, Pander P, et al. Luminescent halogen-substituted 2-(N-arylimino)pyrrolyl boron complexes: the internal heavy-atom effect. Dalton Trans 2020;49:10185–202. https://doi.org/10.1039/D0DT01845G.

24 For example: (a) Melhuish WH. Nomenclature, symbols, units and their usage in spectrochemical analysis-Part VI: molecular luminescence spectroscopy. Pure Appl Chem 1984;56:231–45. https://doi.org/10.1351/pac198456020231. (b) Zhang Y, Aslan K, Previte MJR, Geddes CD. Metal-enhanced e-type fluorescence. Appl Phys Lett 2008;92:013905. https://doi.org/10.1063/1.2829798.

25. For example: (a) Gomes PT, Green MLH, Martins AM. Ansa-bridged η-cyclopentadienyl imido and amido derivatives of titanium, zirconium and molybdenum. J Organomet Chem 1998;551:133–8. https://doi.org/10.1016/S0022-328X(97)00516-0. (b) Marques MM, Fernandes S, Correia SG, Ascenso JR, Caroço S, Gomes PT, et al. Synthesis of acrylamide/olefin copolymers by a diimine nickel catalyst. Macromol Chem Phys 2000;201:2464–8. https://doi.org/10.1002/1521-3935(20001101)201:17<2464::AID-MACP2464>3.0.CO;2-0. (c) Li LD, Lopes PS, Figueira CA, Gomes CSB, Duarte MT, Rosa V, et al. Cationic and Neutral (Ar-BIAN) Copper(I) Complexes Containing Phosphane and Arsane Ancillary Ligands: Synthesis, Molecular Structure and Catalytic Behaviour in Cycloaddition Reactions of Azides and Alkynes. Eur J Inorg Chem 2013:1404–17. https://doi.org/10.1002/ejic.201201211. (d) Suresh D, Ferreira B, Lopes PS, Gomes CSB, Krishnamoorthy P, Charas A, et al. Boron complexes of aromatic ring fused iminopyrrolyl ligands: synthesis, structure, and luminescence properties. Dalton Trans 2016;45:15603–20. https://doi.org/10.1039/c6dt02771g.

26 Köster R, Binger P, Fenzl W, Wonchoba ER, Parshall GW. Triphenylborane. Inorg Synth 1974:134–6. https://doi.org/10.1002/9780470132463.ch30.

27 Sheldrick GM. SADABS: Program for Empirical Absorption Correction. Germany: University of Göttingen; 1996.

28 Burla MC, Caliandro R, Camalli M, Carrozzini B, Cascarano GL, De Caro L, et al. *SIR2004*: an improved tool for crystal structure determination and refinement. J Appl Crystallogr 2005;38:381–8. https://doi.org/10.1107/S002188980403225X.

29 Burla MC, Caliandro R, Carrozzini B, Cascarano GL, Cuocci C, Giacovazzo C, et al. Crystal structure determination and refinement via *SIR2014*. J Appl Crystallogr 2015;48:306–9. https://doi.org/10.1107/S1600576715001132.

30 (a) Burla MC, Caliandro R, Carrozzini B, Cascarano GL, Cuocci C, Giacovazzo C, et al. Crystal structure determination and refinement via *SIR2014*. J Appl Crystallogr 2015;48:306–9. https://doi.org/10.1107/S1600576715001132. (b) Sheldrick GM. Crystal structure refinement with *SHELXL*. Acta Crystallogr C Struct Chem 2015;71:3–8. https://doi.org/10.1107/S2053229614024218.

31 Farrugia LJ. *WinGX* and *ORTEP for Windows*: an update. J Appl Crystallogr 2012;45:849–54. https://doi.org/10.1107/S0021889812029111.

32 Vosko SH, Wilk L, Nusair M. Accurate spin-dependent electron liquid correlation energies for local spin density calculations: a critical analysis. Can J Phys 1980;58:1200–11. https://doi.org/10.1139/p80-159.

33 Ernzerhof M, Scuseria GE. Assessment of the Perdew–Burke–Ernzerhof exchange-correlation functional. J Chem Phys 1999;110:5029–36. https://doi.org/10.1063/1.478401.

34 Adamo C, Barone V. Toward reliable density functional methods without adjustable parameters: The PBE0 model. J Chem Phys 1999;110:6158–70. https://doi.org/10.1063/1.478522.

35 van Lenthe E, Ehlers A, Baerends E-J. Geometry optimizations in the zero order regular approximation for relativistic effects. J Chem Phys 1999;110:8943–53. https://doi.org/10.1063/1.478813.

36 Hirata S, Head-Gordon M. Time-dependent density functional theory within the Tamm–Dancoff approximation. Chem Phys Lett 1999;314:291–9. https://doi.org/10.1016/S0009-2614(99)01149-5.

37 (a) Rodrigues AI, Figueira CA, Gomes CSB, Suresh D, Ferreira B, Di Paolo RE, et al. Boron complexes of aromatic 5-substituted iminopyrrolyl ligands: synthesis, structure, and luminescence properties. Dalton Trans 2019;48:13337–52. https://doi.org/10.1039/C9DT02718A. (b) Paramasivam K, Fialho CB, Cruz TFC, Rodrigues AI, Ferreira B, Gomes CSB, et al. New luminescent tetracoordinate boron complexes: an in-depth experimental and theoretical characterisation and their application in OLEDs. Inorg Chem Front 2021;8:3960–83. https://doi.org/10.1039/D1QI00403D.

38 Grimme S. Accurate description of van der Waals complexes by density functional theory including empirical corrections. J Comput Chem 2004;25:1463–73. https://doi.org/10.1002/jcc.20078.

39 Reiher M, Salomon O, Artur Hess B. Reparameterization of hybrid functionals based on energy differences of states of different multiplicity. Theor Chem Acc 2001;107:48–55. https://doi.org/10.1007/s00214-001-0300-3.

40 Becke AD. A new inhomogeneity parameter in density-functional theory. J Chem Phys 1998;109:2092–8. https://doi.org/10.1063/1.476722.

41 (a) Perdew JP. Density-functional approximation for the correlation energy of the inhomogeneous electron gas. Phys Rev B 1986;33:8822–4. https://doi.org/10.1103/PhysRevB.33.8822. (b) Perdew JP. Erratum: Density-functional approximation for the correlation energy of the inhomogeneous electron gas. Phys Rev B 1986;34:7406–7406. https://doi.org/10.1103/PhysRevB.34.7406.

42 Chemcraft Program, https://www.chemcraftprog.com/index.html (last accessed on 10 April 2024).

43 (a) Vieira Ferreira LF, Ferreira Machado I, Gama A, Lochte F, Socoteanu RP, Boscencu R. Surface photochemical studies of nano-hybrids of A3B porphyrins and Fe3O4 silica-coated nanoparticles. J Photochem Photobiol A 2020;387:112152. https://doi.org/10.1016/j.jphotochem.2019.112152. (b) Ferreira DP, Conceição DS, Fernandes F, Sousa T, Calhelha RC, Ferreira ICFR, et al. Characterization of a Squaraine/Chitosan System for Photodynamic Therapy of Cancer. J Phys Chem B 2016;120:1212–20. https://doi.org/10.1021/acs.jpcb.5b11604. (c) Barbieri A, Accorsi G. Absolute Photoluminescence Quantum Yield Determination of Solid-state Samples. EPA Newsletter 2006:26–34.

44 Branco TJF, Botelho do Rego AM, Ferreira Machado I, Vieira Ferreira LF. Luminescence Lifetime Distributions Analysis in Heterogeneous Systems by the Use of Excel's Solver. J Phys Chem B 2005;109:15958–67. https://doi.org/10.1021/jp0520087.

45 de Sa Pereira D, Monkman AP, Data P. Production and Characterization of Vacuum Deposited Organic Light Emitting Diodes. J Vis Exp 2018;141:e56593. https://doi.org/10.3791/56593.

Supplementary Material for

9-Borafluoren-9-yl and diphenylboron tetracoordinate complexes of 8-quinolinolato ligands with heavy-atoms substituents: synthesis, fluorescence and application in OLED devices

Carina B. Fialho,[a] Tiago F. C. Cruz,[a] Maria José Calhorda,[b] Luís F. Vieira Ferreira,[c] Piotr Pander,[d,e,f] Fernando B. Dias,[f] António L. Maçanita,[a] Pedro T. Gomes[a]

[a] *Centro de Química Estrutural, Departamento de Engenharia Química, Instituto Superior Técnico, Universidade de Lisboa, Av. Rovisco Pais, 1049-001 Lisboa, Portugal.*
E-mail: pedro.t.gomes@tecnico.ulisboa.pt

[b] *BioISI - Instituto de Biossistemas e Ciências Integrativas, Departamento de Química e Bioquímica, Faculdade de Ciências, Universidade de Lisboa, Campo Grande, 1749-016 Lisboa, Portugal.*

[c] *BSIRG – Biospectroscopy and Interfaces Research Group, IBB-Institute for Bioengineering and Biosciences, Instituto SuperiorTécnico, Universidade de Lisboa, 1049-001 Lisboa, Portugal*

[d] *Faculty of Chemistry, Silesian University of Technology, Strzody 9, 44-100 Gliwice, Poland*

[e] *Centre for Organic and Nanohybrid Electronics, Silesian University of Technology, Konarskiego 22B, 44-100 Gliwice, Poland*

[f] *Department of Physics, Durham University, South Road, Durham DH1 3LE, U.K.*

Table of Contents

NMR spectra of complexes 3a-3d and 4a-4d

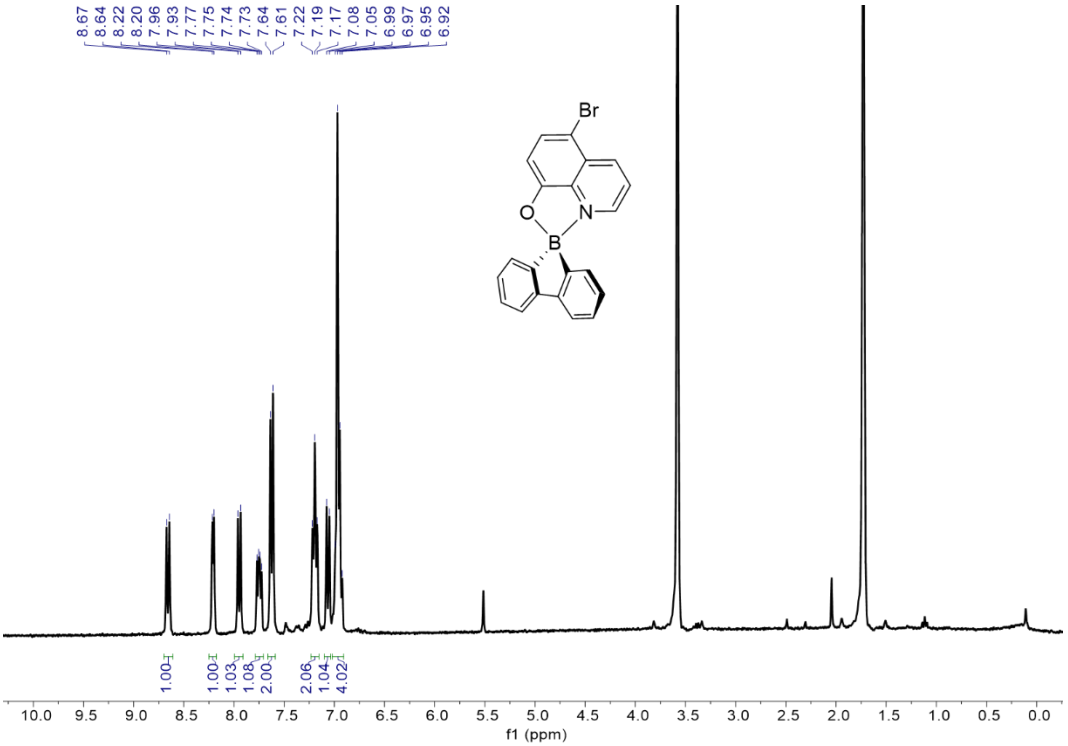

Fig. S1 ^{1}H NMR (THF-d_8, 300 MHz) spectrum of complex **3a**.

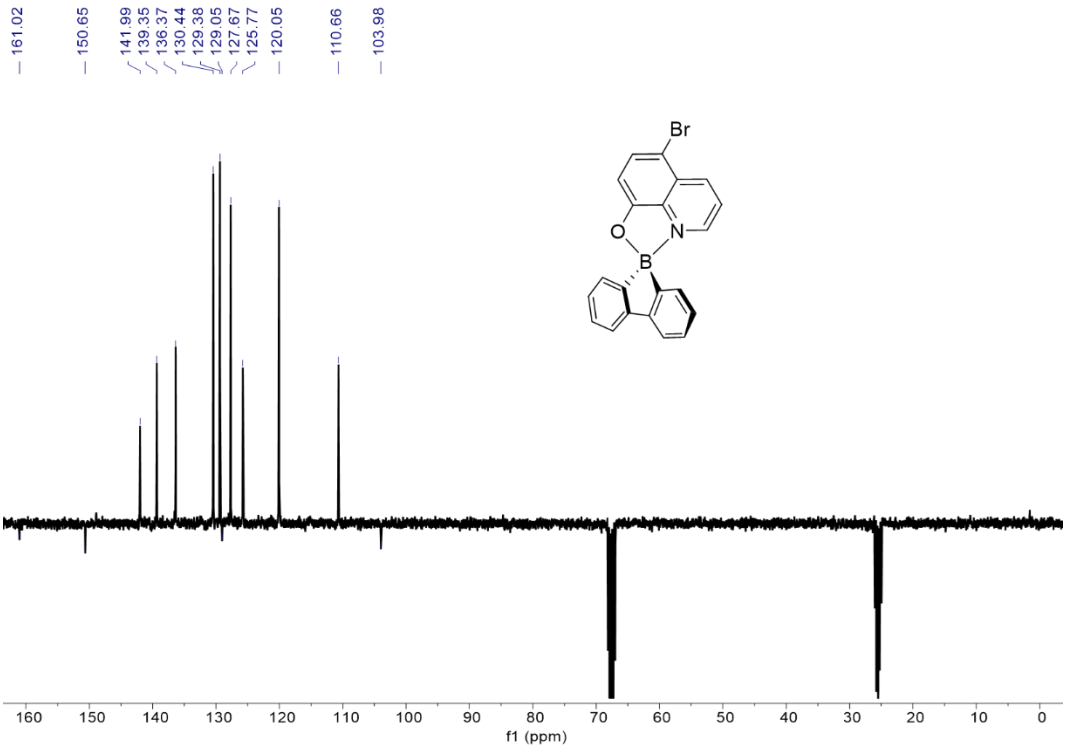

Fig. S2 ^{13}C APT NMR (THF-d_8, 75 MHz) spectrum of complex **3a**.

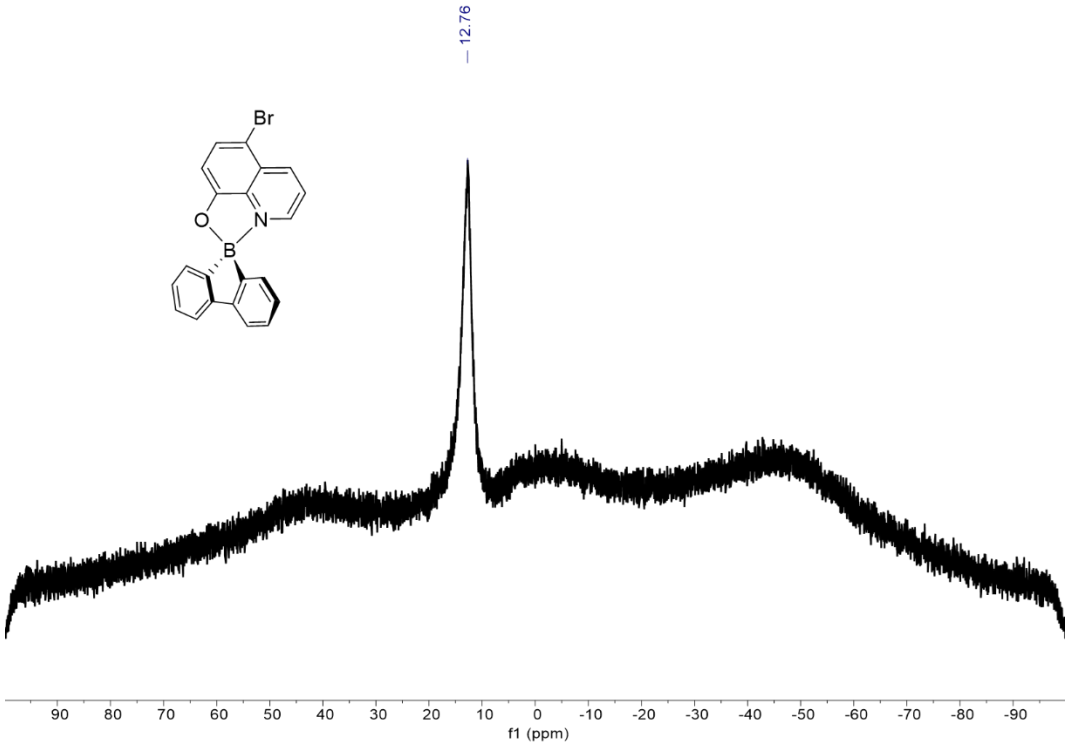

Fig. S3 ^{11}B NMR (THF-d_8, 96 MHz) spectrum of complex **3a**.

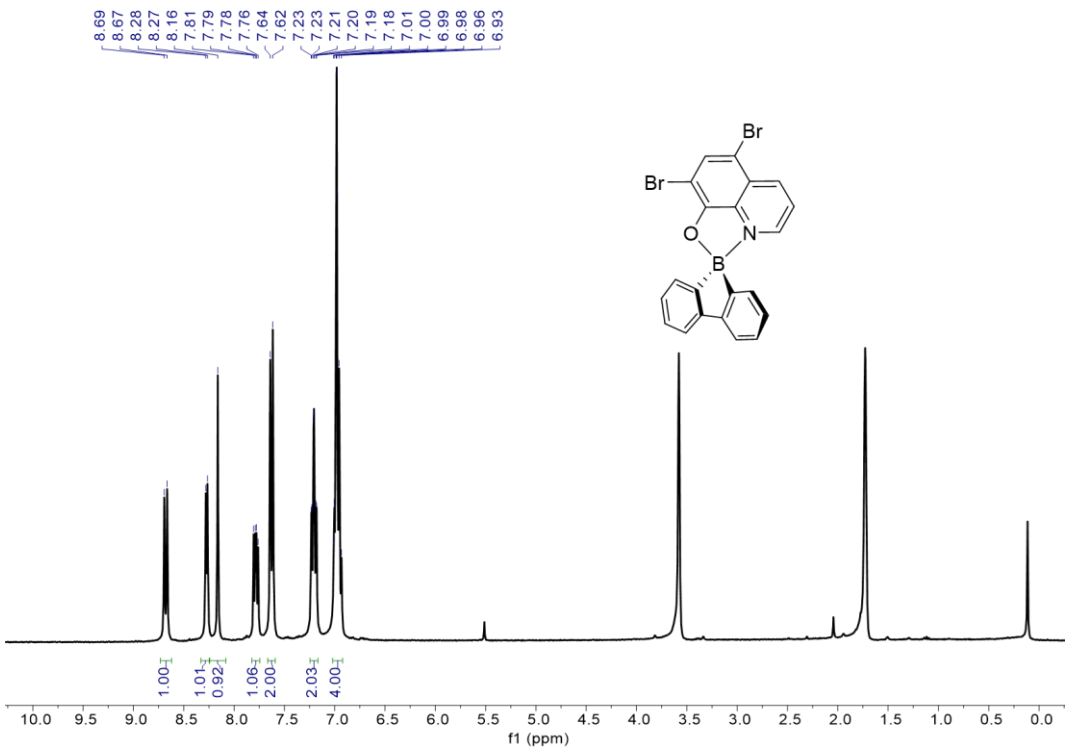

Fig. S4 ^{1}H NMR (THF-d_8, 300 MHz) spectrum of complex **3b**.

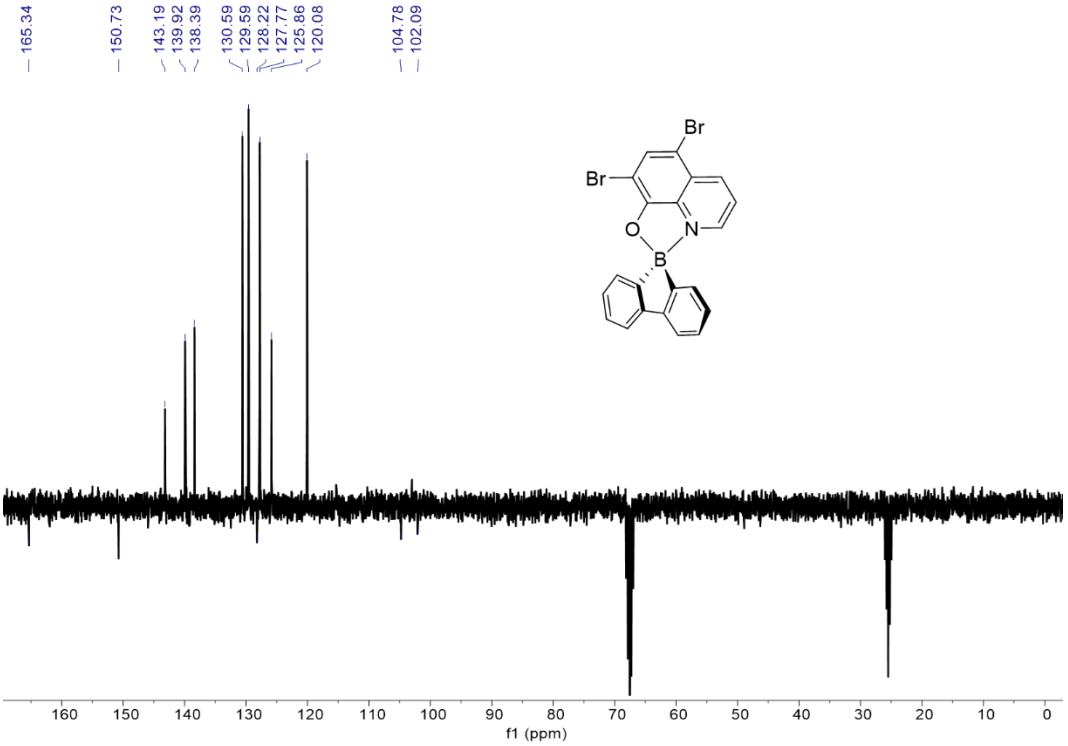

Fig. S5 ^{13}C APT NMR (THF-d_8, 75 MHz) spectrum of complex **3b**.

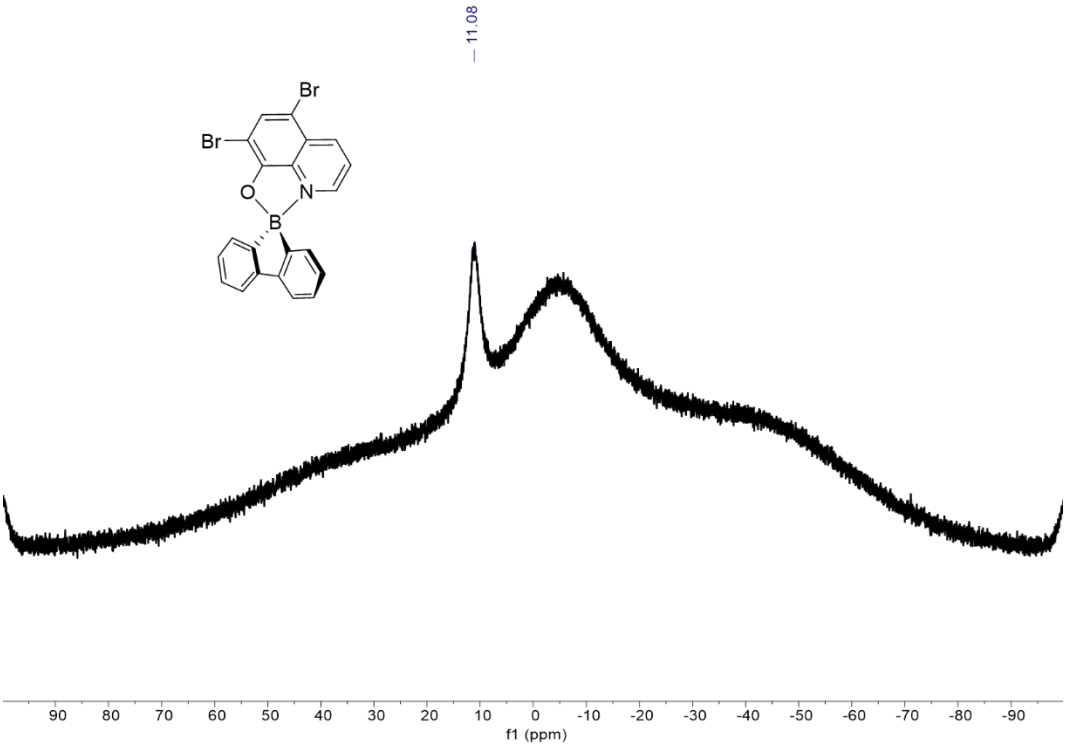

Fig. S6 ^{11}B NMR (THF-d_8, 96 MHz) spectrum of complex **3b**.

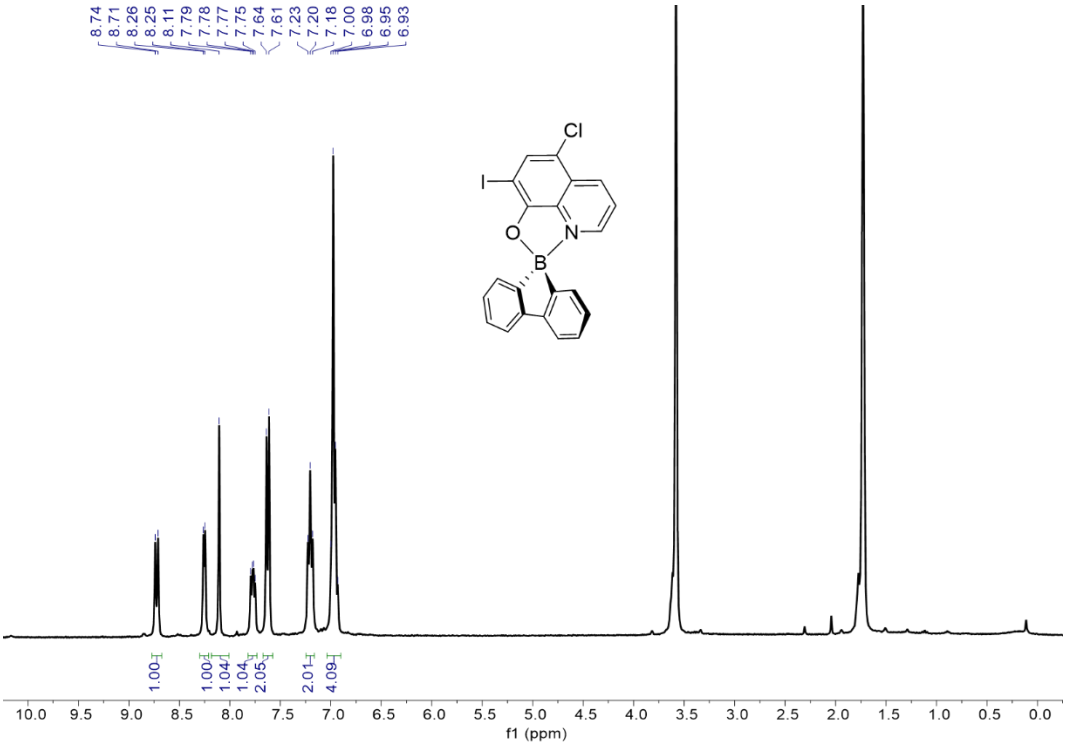

Fig. S7 ^{1}H NMR (THF-d_8, 300 MHz) spectrum of complex **3c**.

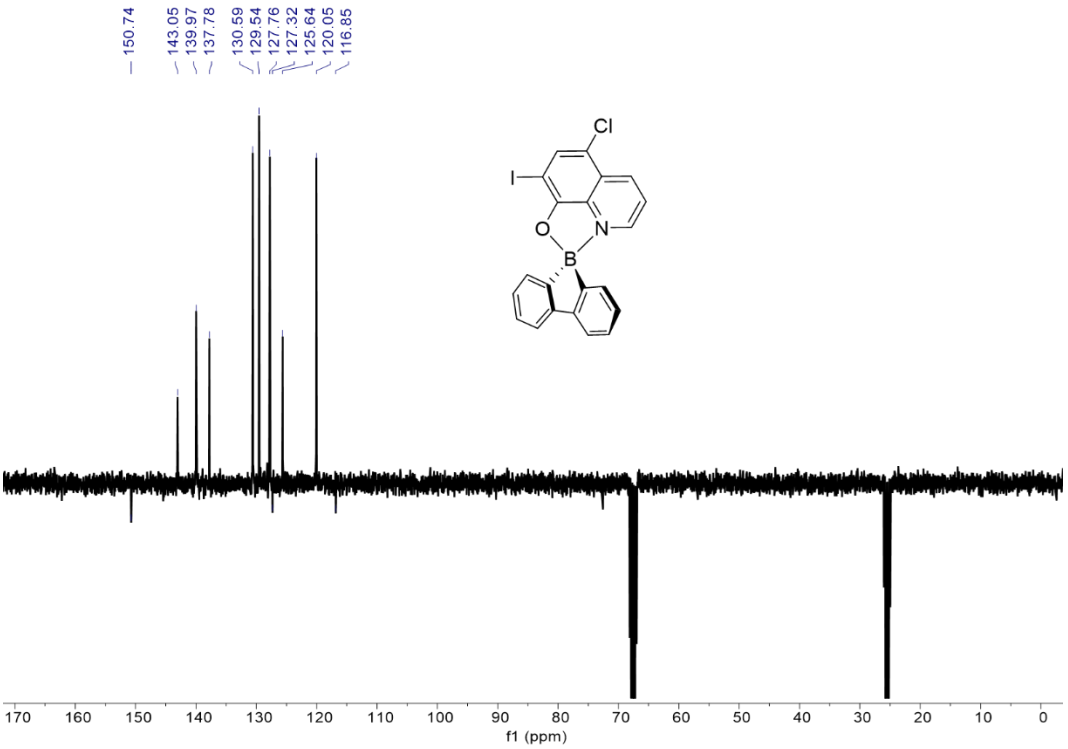

Fig. S8 ^{13}C APT NMR (THF-d_8, 75 MHz) spectrum of complex **3c**.

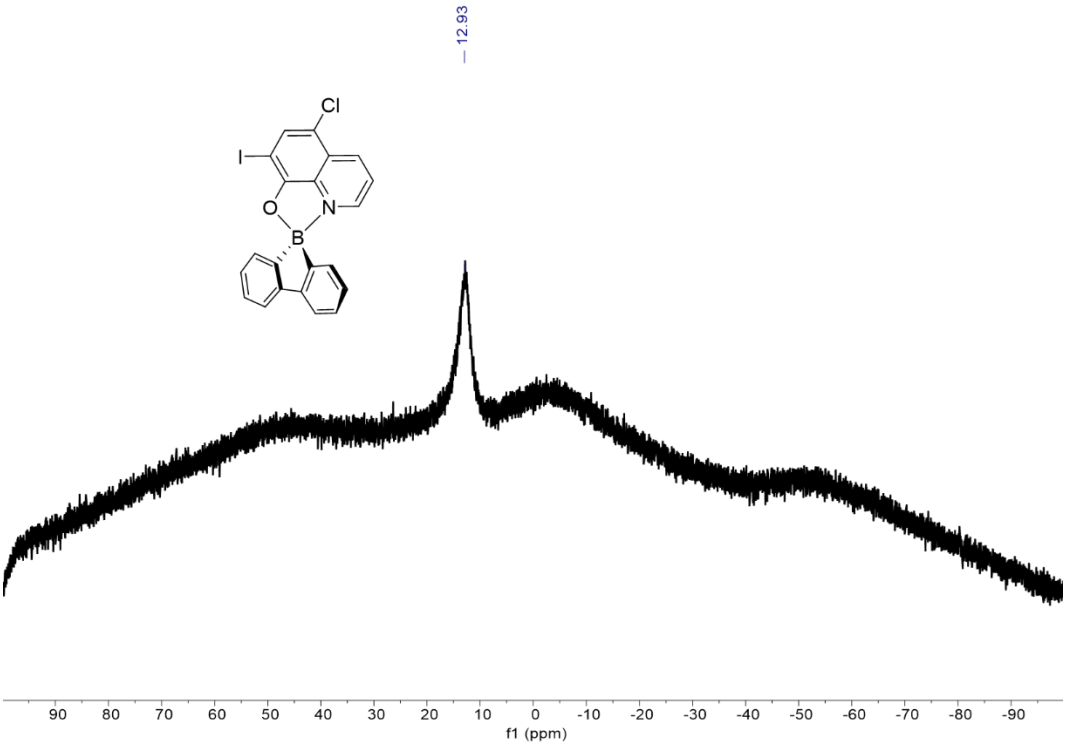

Fig. S9 ^{11}B NMR (THF-d_8, 96 MHz) spectrum of complex **3c**.

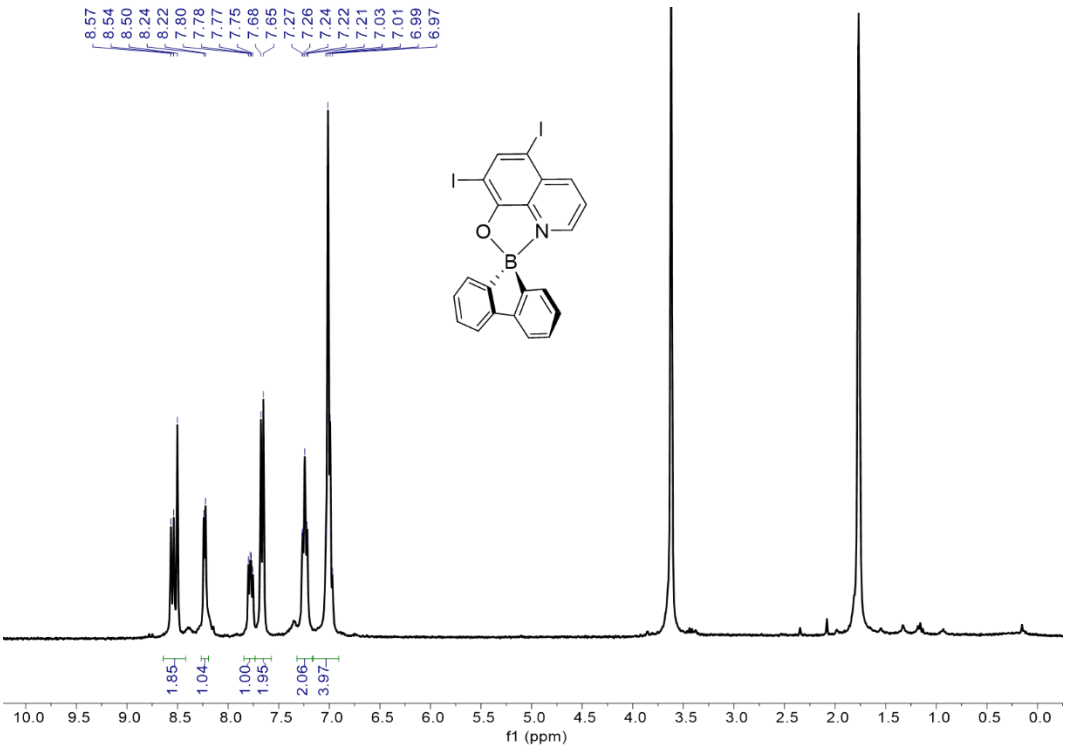

Fig. S10 ^{1}H NMR (THF-d_8, 300 MHz) spectrum of complex **3d**.

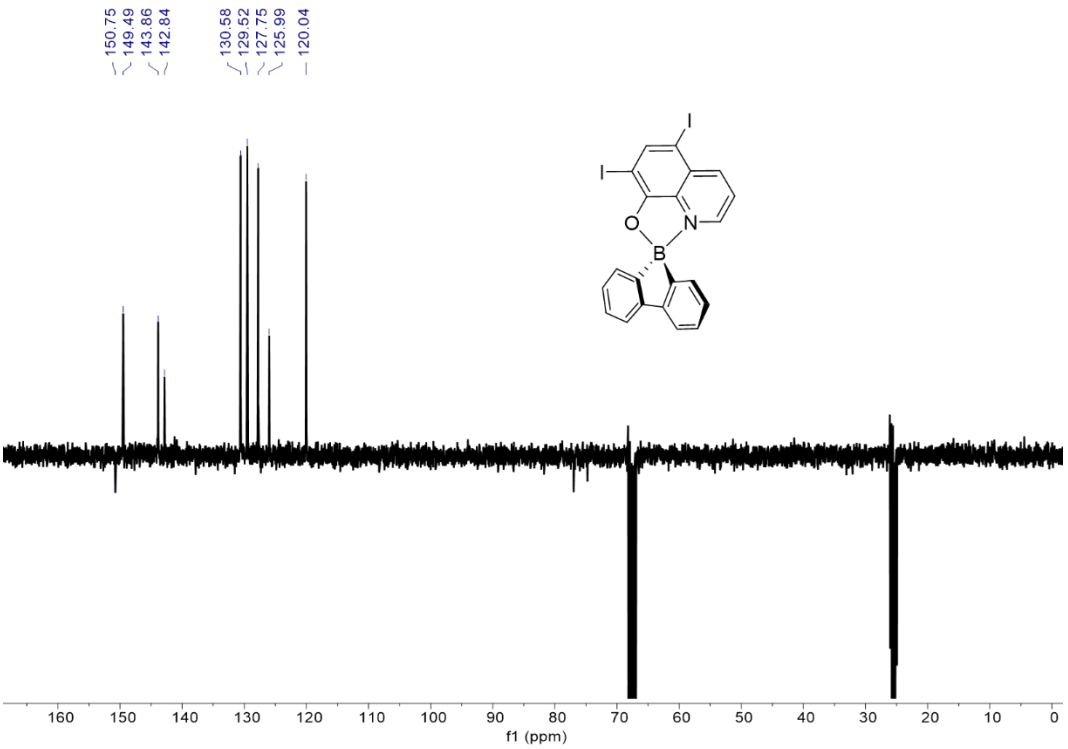

Fig. S11 ^{13}C APT NMR (THF-d_8, 75 MHz) spectrum of complex **3d**.

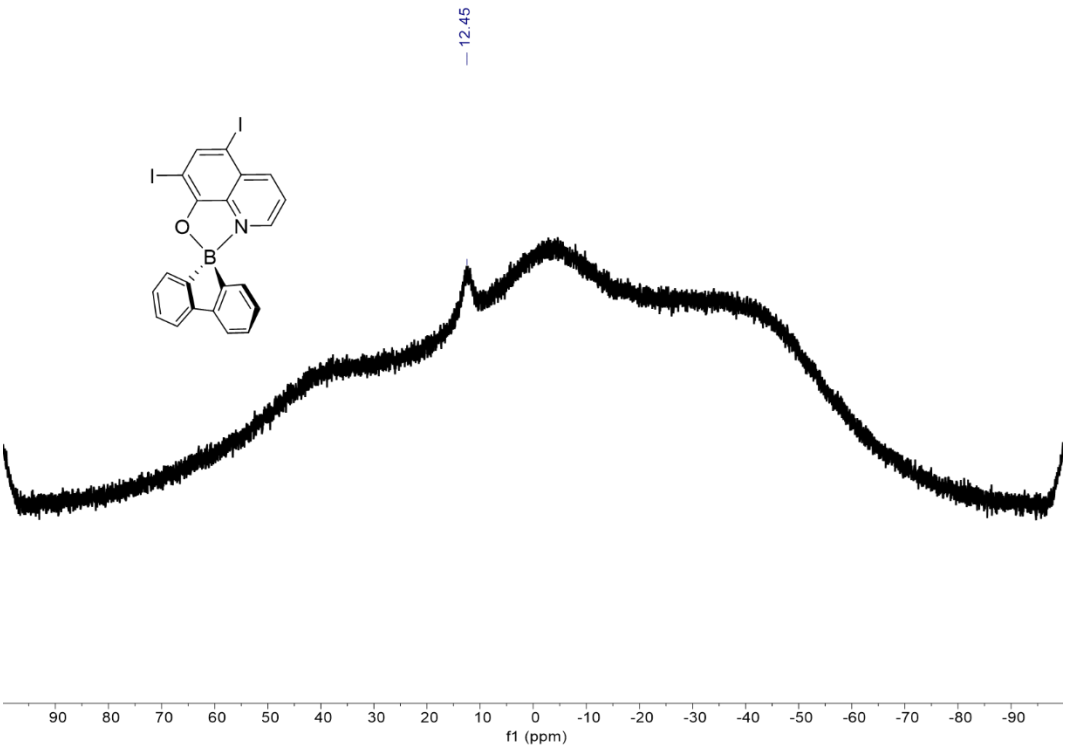

Fig. S12 ^{11}B NMR (THF-d_8, 96 MHz) spectrum of complex **3d**.

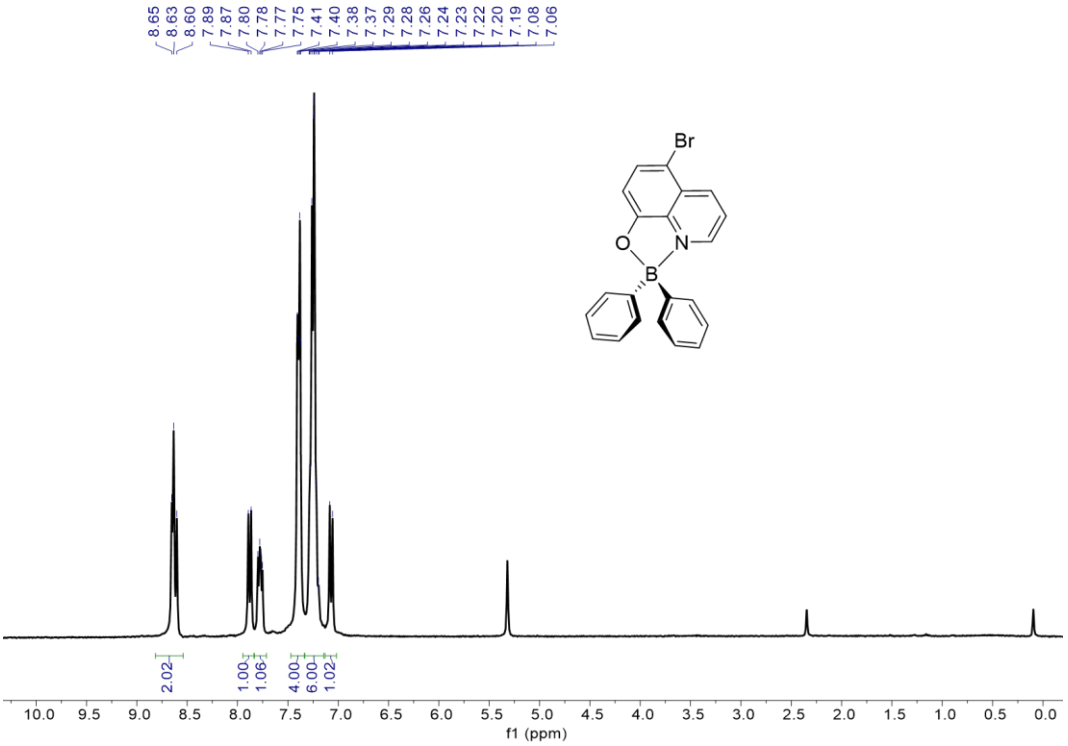

Fig. S13 ^{1}H NMR (CD_2Cl_2, 300 MHz) spectrum of complex **4a**.

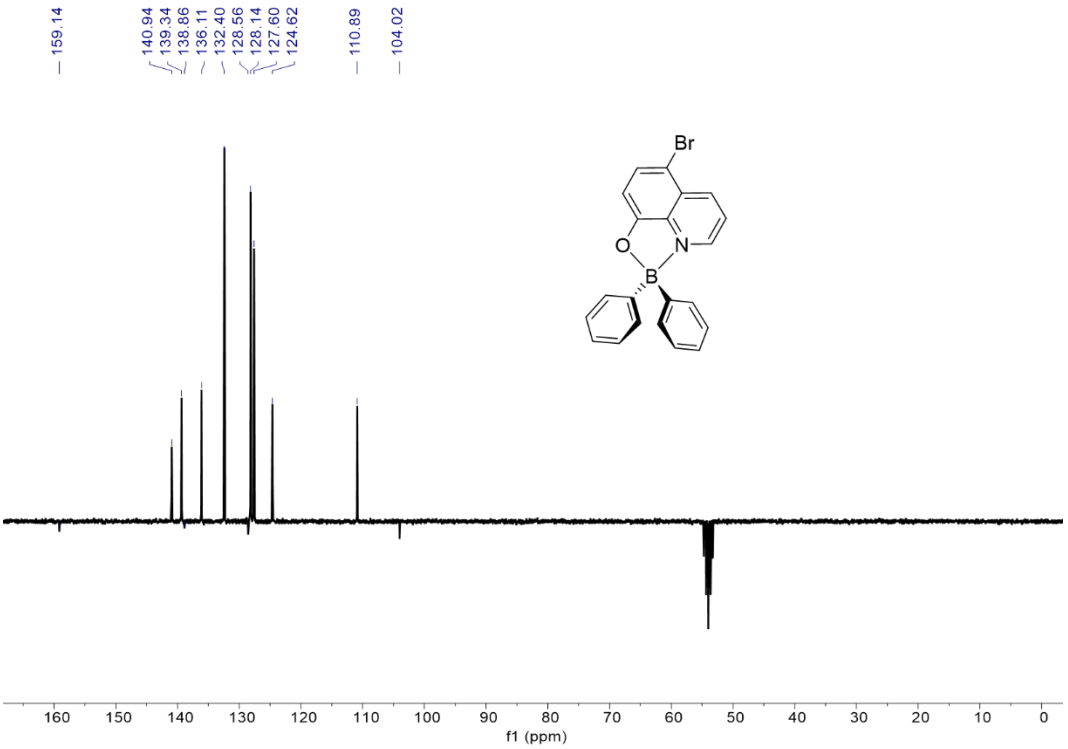

Fig. S14 ^{13}C APT NMR (CD_2Cl_2, 75 MHz) spectrum of complex **4a**.

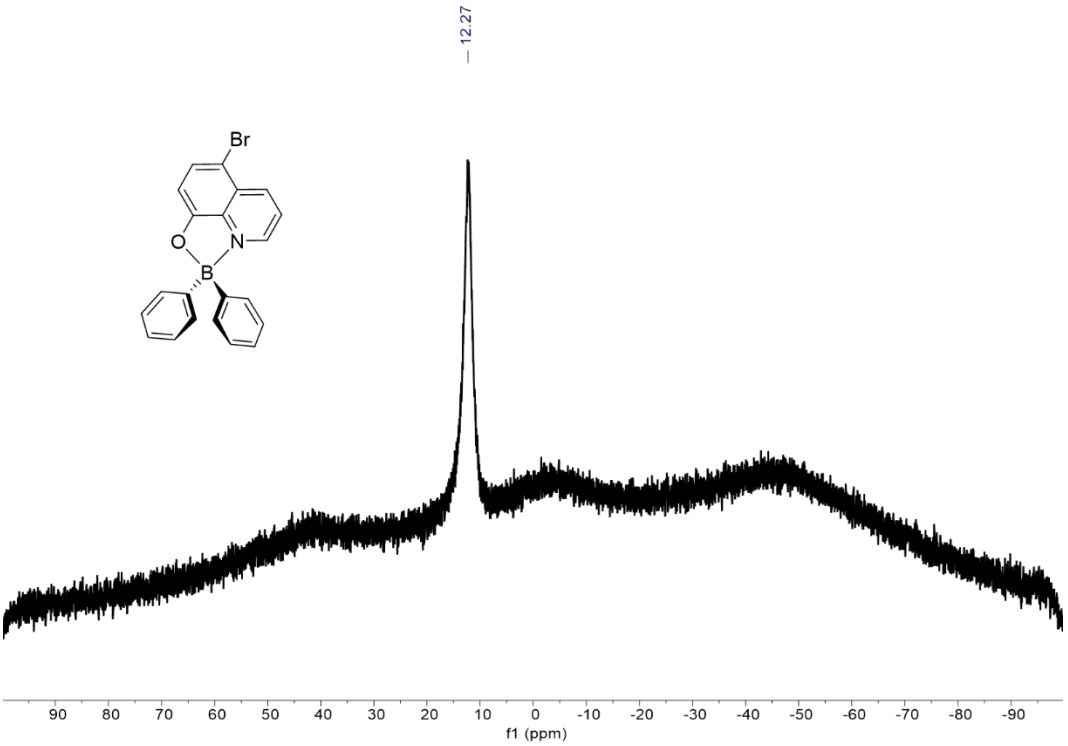

Fig. S15 ^{11}B NMR (CD_2Cl_2, 96 MHz) spectrum of complex **4a**.

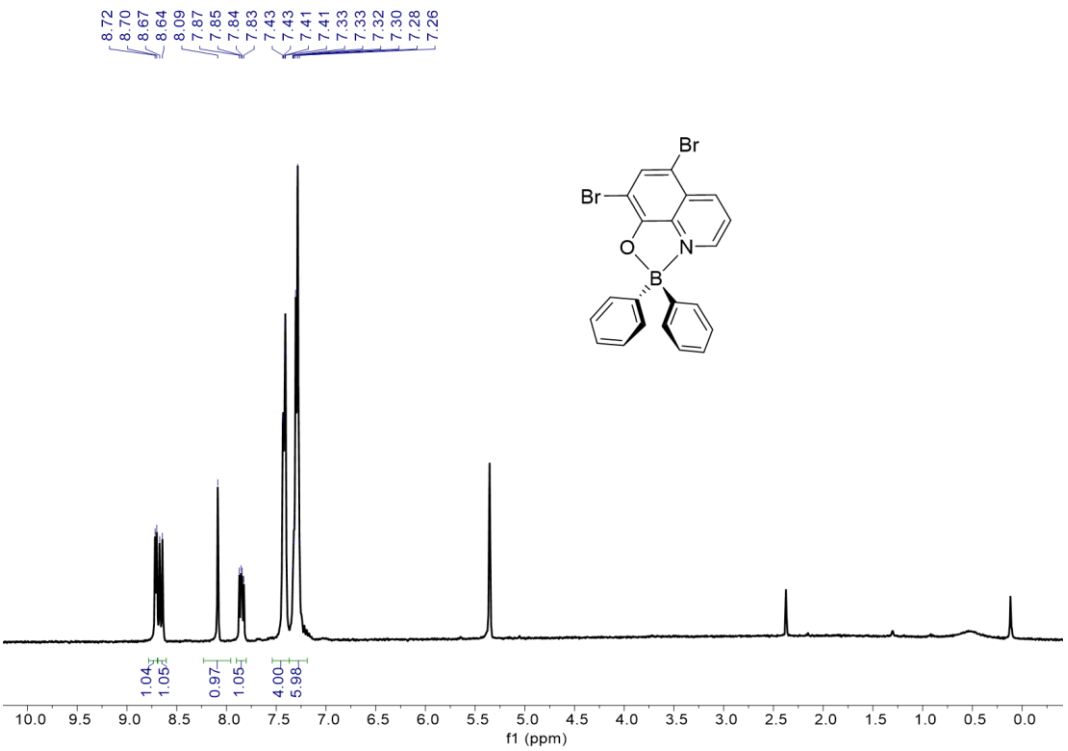

Fig. S16 ^{1}H NMR (CD_2Cl_2, 300 MHz) spectrum of complex **4b**.

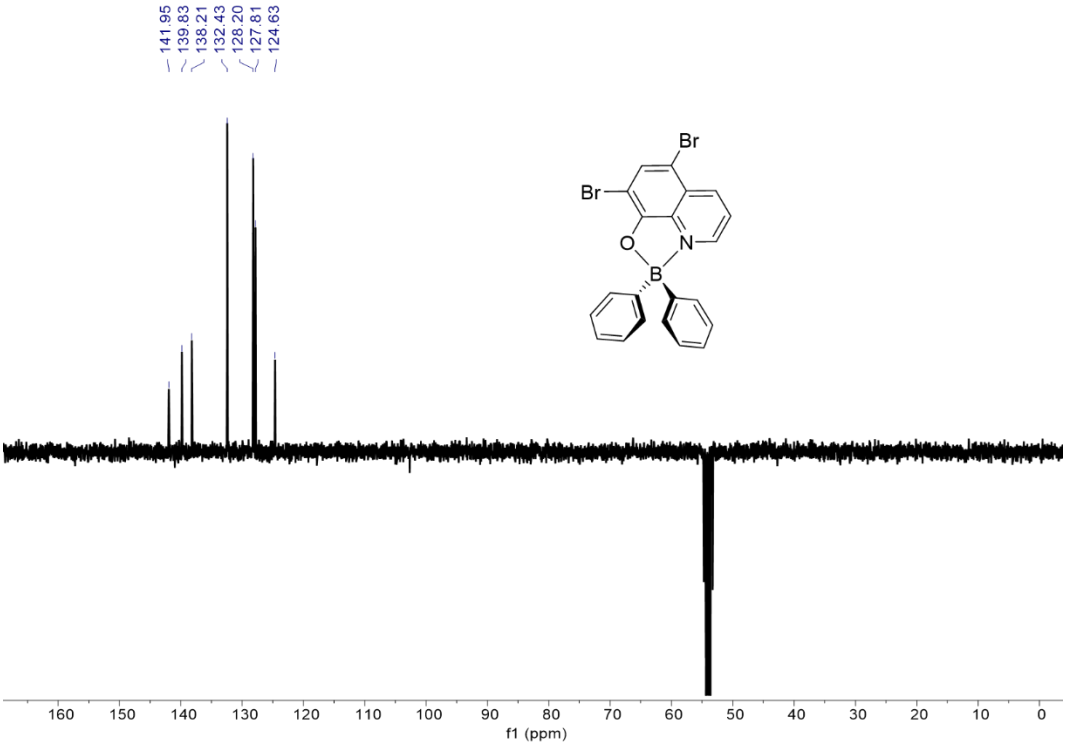

Fig. S17 ^{13}C APT NMR (CD_2Cl_2, 75 MHz) spectrum of complex **4b**.

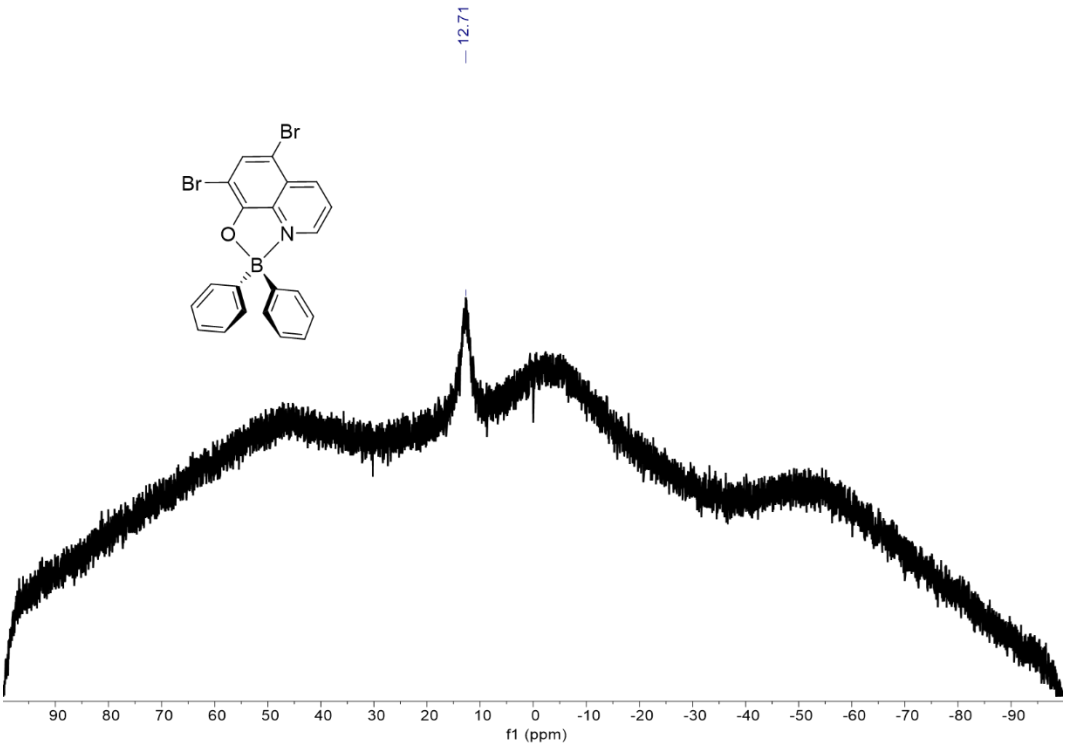

Fig. S18 ^{11}B NMR (CD_2Cl_2, 96 MHz) spectrum of complex **4b**.

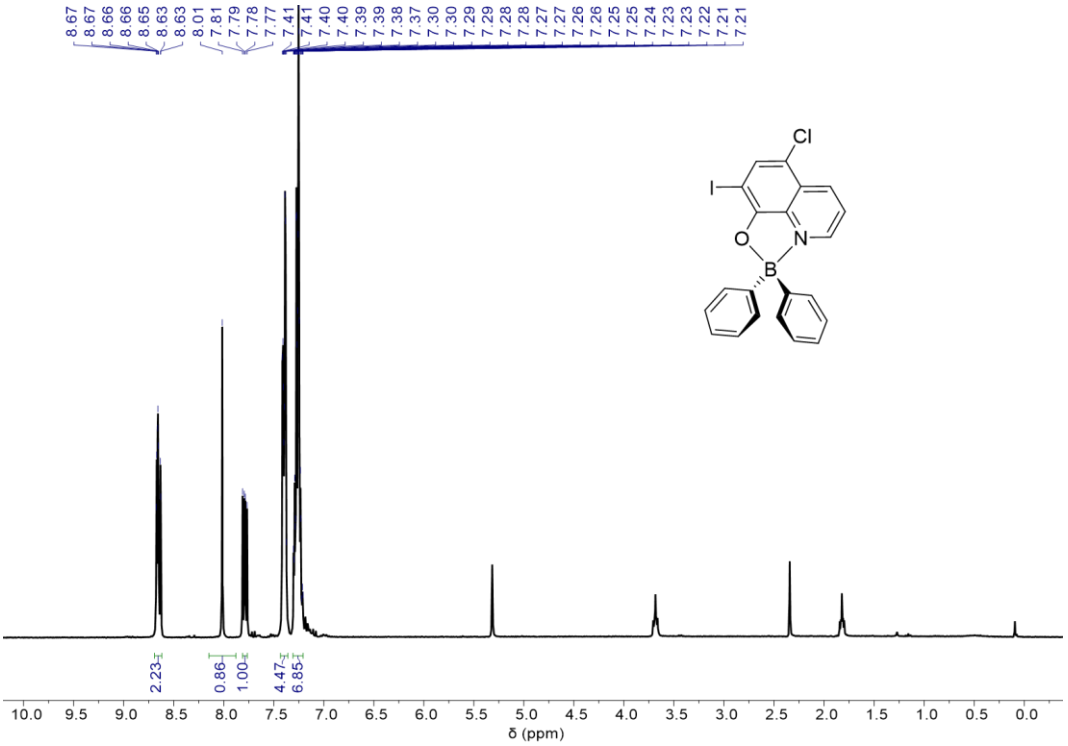

Fig. S19 ^{1}H NMR (CD_2Cl_2, 300 MHz) spectrum of complex **4c**.

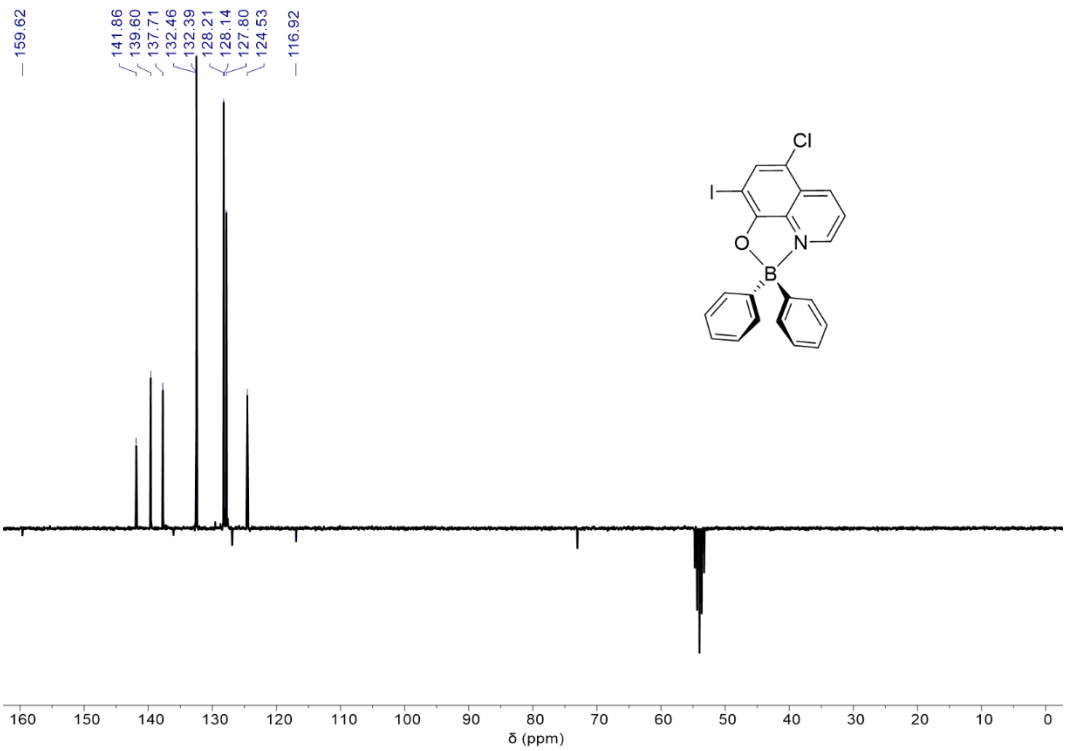

Fig. S20 ^{13}C APT NMR (CD_2Cl_2, 75 MHz) spectrum of complex **4c**.

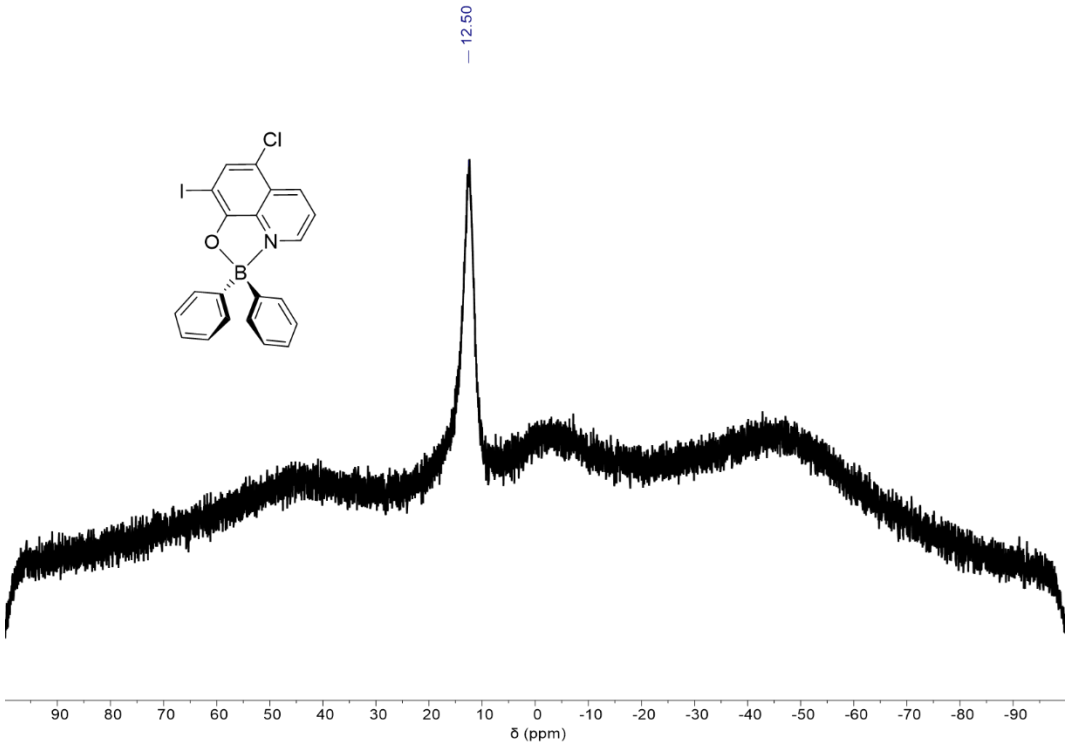

Fig. S21 ^{11}B NMR (CD_2Cl_2, 96 MHz) spectrum of complex **4c**.

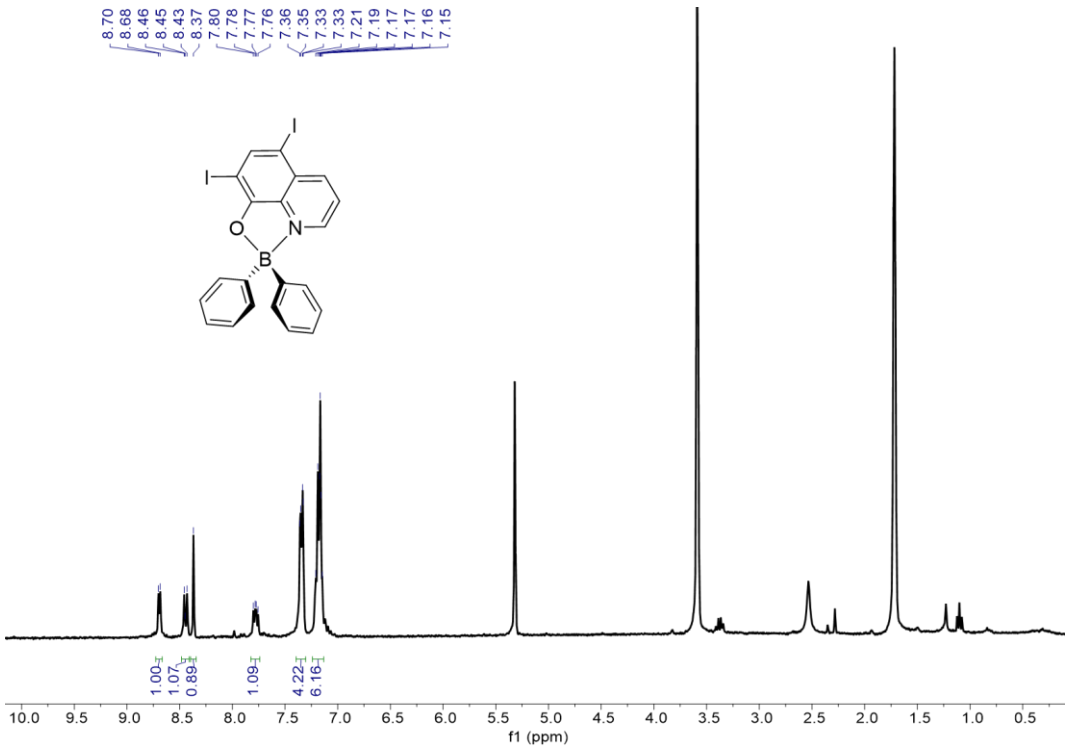

Fig. S22 ^{1}H NMR (CD_2Cl_2, 300 MHz) spectrum of complex **4d**.

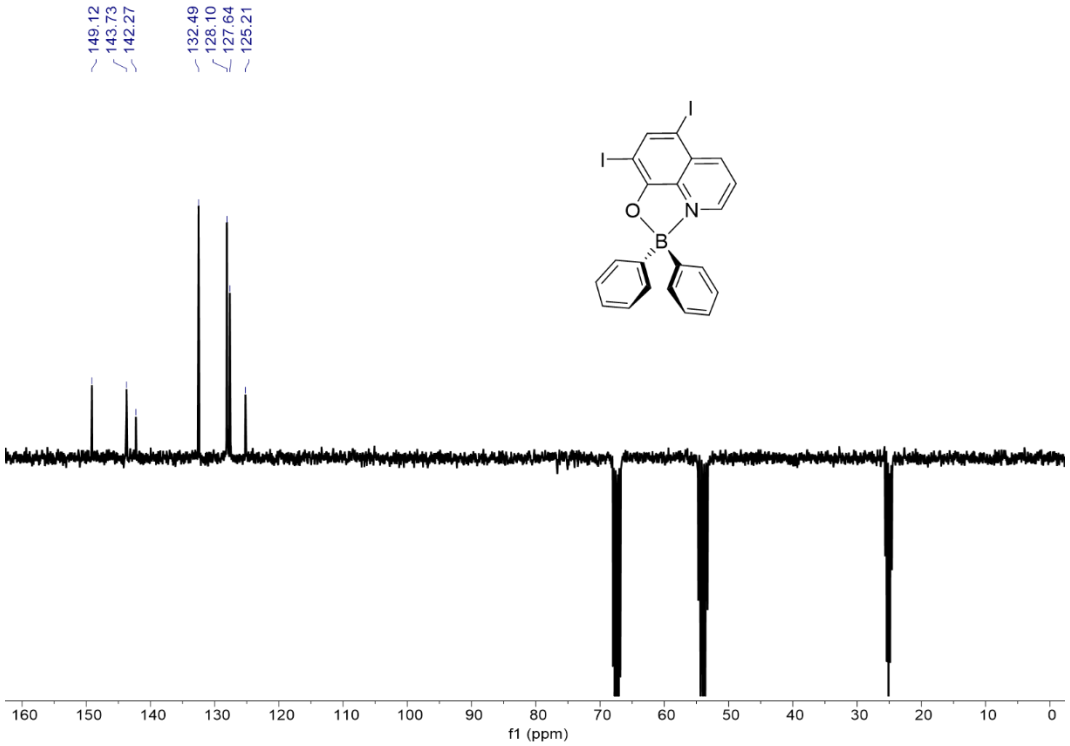

Fig. S23 ^{13}C APT NMR (CD_2Cl_2, 75 MHz) spectrum of complex **4d**.

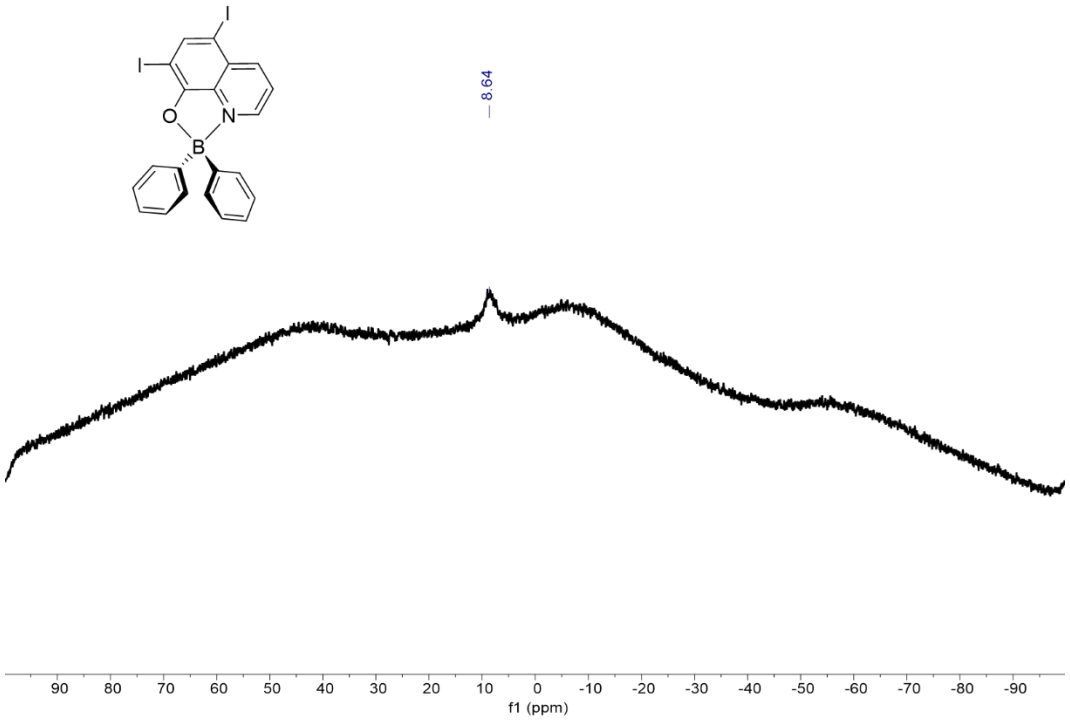

Fig. S24 ^{11}B NMR (CD_2Cl_2, 96 MHz) spectrum of complex **4d**.

Crystallographic and molecular structure data of boron complexes 3a, 3d and 4a-4d

Table S1. Crystallographic data for boron complexes **3a** and **3d**.

	3a	**3d**
Formula	$C_{21}H_{13}BBrNO$	$C_{21}H_{12}BI_2NO$
M (g mol^{-1})	386.04	558.93
λ (Å)	0.71073	0.71073
T (K)	150(2)	150(2)
Crystal system	Triclinic	Monoclinic
Space group	P-1	$P2_1/c$
a (Å)	8.429(7)	13.3783(11)
b (Å)	13.004(12)	11.4151(8)
c (Å)	15.905(14)	13.8673(8)
α (º)	89.72(3)	90
β (º)	76.47(2)	117.816(4)
γ (º)	89.62(3)	90
V (Å^3)	1695(3)	1873.0(2)
Z	4	4
ρ_{calc} (g cm^{-3})	1.513	1.982
Crystal size (mm)	0.20×0.08×0.08	0.10×0.10×0.05
θ_{max} (º)	26.673	27.260
Total data	5052	11337
Unique data	3575	4131
R_{int}	0.0920	0.0570
R [I > 2σ(I)]	0.1623	0.0414
wR	0.2463	0.0552
Goodness of fit	0.832	0.983
ρ_{min}, ρ_{max}	-0.626, 0.403	-1.009, 2004

Table S2. Crystallographic data for boron complexes **4a**-**4d**.

	4a	**4b**	**4c**	**4d**
Formula	$C_{21}H_{15}BBrNO$	$C_{21}H_{14}BBr_2NO$	$C_{21}H_{14}BClINO$	$C_{21}H_{14}BI_2NO$
M (g mol^{-1})	388.06	466.96	469.49	560.94
λ (Å)	0.71073	0.71073	0.71073	0.71073
T (K)	150(2)	150(2)	150(2)	150(2)
Crystal system	Monoclinic	Monoclinic	Monoclinic	Monoclinic
Space group	$P2_1/c$	$P2_1/n$	$P2_1/n$	$P2_1/n$
a (Å)	11.7963(17)	8.9829(6)	8.9459(6)	9.1560(6)
b (Å)	14.572(2)	18.1510(19)	18.2389(12)	18.3248(12)
c (Å)	10.8713(17)	11.2058(10)	11.3753(6)	11.3879(6)
α (º)	90	90	90	90
β (º)	114.636(5)	101.823(4)	100.633(3)	101.464(3)
γ (º)	90	90	90	90
V (Å^3)	1698.7(4)	1788.3(3)	1824.2(2)	1872.6(2)
Z	4	4	4	4
ρ_{calc} (g cm^{-3})	1.517	1.734	1.710	1.990
Crystal size (mm)	0.01×0.01×0.01	0.25×0.25×0.05	0.15×0.15×0.04	0.20×0.10×0.02
θ_{max} (º)	25.709	29.310	25.694	25.745
Total data	7158	17549	13519	13955
Unique data	3236	4828	3463	3568
R_{int}	0.0519	0.0570	0.0376	0.0463
R [I > 2σ(I)]	0.0539	0.0784	0.0275	0.0265
wR	0.0984	0.0846	0.0349	0.0310
Goodness of fit	1.009	1.016	1.113	1.163
ρ_{min}, ρ_{max}	-0.635, 0.915	-0.600, 0.496	-1.108, 0.637	-0.995, 0.707

Selected bond lengths and angles for complexes 3a, 3d and 4a-4d

Table S3. Selected experimental and calculated (DFT) bond lengths (Å) and angles (º) for complexes **3a** and **d**. Atoms X1/X2 refer to the halogen atoms in 5 and 7 positions of the 8-hydroxyquinolinate, respectively.

	3a (molecule 1)	**3a** (molecule 2)	**3a** (DFT)	**3d**	**3d** (DFT)
Lengths (Å)					
B(1)-O(1)	1.56(3)	1.66(4)	1.514	1.518(6)	1.517
B(1)-C(12)	1.67(4)	1.53(5)	1.609	1.608(7)	1.608
B(1)-C(1)	1.53(7)	1.56(5)	1.608	1.600(7)	1.610
B(1)-N(1)	1.75(3)	1.68(7)	1.608	1.617(6)	1.608
C(1)-C(2)	1.33(7)	1.47(2)	1.387	1.389(6)	1.386
C(1)-C(6)	1.41(3)	1.43(5)	1.407	1.411(7)	1.406
C(6)-C(7)	1.45(8)	1.55(2)	1.476	1.496(7)	1.476
C(7)-C(12)	1.45(7)	1.37(5)	1.406	1.399(7)	1.407
C(11)-C(12)	1.22(8)	1.41(2)	1.386	1.402(6)	1.387
C(13)-N(1)	1.28(2)	1.35(4)	1.320	1.323(6)	1.320
C(16)-C(21)	1.38(3)	1.40(6)	1.399	1.407(6)	1.400
C(16)-C(17)	1.46(4)	1.45(5)	1.414	1.407(7)	1.418
C(17)-C(18)	1.32(2)	1.47(4)	1.374	1.358(6)	1.375
C(17)-X(1)	1.89(2)	1.86(5)	1.901	2.098(5)	2.107
C(18)-C(19)	1.42(3)	1.38(6)	1.412	1.422(7)	1.416
C(19)-C(20)	1.36(3)	1.50(5)	1.374	1.377(7)	1.375
C(19)-X(2)	-	-	-	2.095(4)	2.096
C(20)-O(1)	1.32(2)	1.26(5)	1.329	1.331(5)	1.323
C(20)-C(21)	1.36(2)	1.50(5)	1.407	1.407(6)	1.408
C(21)-N(1)	1.37(3)	1.17(5)	1.348	1.359(6)	1.350
Angles (º)					
O(1)-B(1)-C(12)	109(3)	107(4)	116.5	118.5(4)	117.1
O(1)-B(1)-C(1)	126(3)	116(2)	115.3	117.2(4)	114.7
C(12)-B(1)-C(1)	107(3)	107(4)	100.6	100.7(4)	100.7
O(1)-B(1)-N(1)	94(2)	93(4)	99.4	99.1(3)	99.2
C(12)-B(1)-N(1)	108(2)	114(2)	113.5	112.1(4)	113.6
C(1)-B(1)-N(1)	111(3)	112(2)	112.1	109.4(3)	112.3
C(2)-C(1)-C(6)	124(5)	121(3)		117.8(5)	
C(2)-C(1)-B(1)	131(3)	131(3)		132.8(5)	
C(6)-C(1)-B(1)	105(4)	108(2)		109.3(4)	
C(1)-C(6)-C(7)	115(5)	106(3)		109.9(4)	
C(11)-C(12)-C(7)	115(3)	120(3)		117.9(4)	
C(11)-C(12)-B(1)	143(5)	131(3)		133.0(5)	
C(7)-C(12)-B(1)	102(4)	107(2)		109.1(4)	
C(21)-C(16)-C(17)	115(2)	125(4)		114.3(4)	
C(18)-C(17)-C(16)	118(2)	115(5)		121.6(4)	
C(18)-C(17)-X(1)	121(2)	118(3)		119.5(4)	
C(16)-C(17)-X(1)	120(2)	126(3)		119.0(3)	
C(17)-C(18)-C(19)	123(2)	121(4)		122.1(5)	
C(20)-C(19)-C(18)	121(2)	125(3)		119.4(4)	
C(20)-C(19)-X(2)	-	-		120.1(3)	
C(18)-C(19)-X(2)	-	-		120.5(3)	
O(1)-C(20)-C(19)	133(2)	133(3)		130.3(4)	
O(1)-C(20)-C(21)	112(2)	114(4)		113.3(4)	
C(19)-C(20)-C(21)	116(2)	113(4)		116.4(4)	
N(1)-C(21)-C(16)	118(2)	131(4)		124.3(4)	
N(1)-C(21)-C(20)	115(2)	108(5)		109.4(4)	
C(16)-C(21)-C(20)	127(2)	120(4)		126.1(4)	
C(13)-N(1)-C(21)	124 (2)	114(5)		119.4(4)	
C(13)-N(1)-B(1)	131(2)	131(4)		132.8(4)	
C(21)-N(1)-B(1)	105(2)	115(4)		107.8(3)	
C(20)-O(1)-B(1)	115(2)	108(3)		109.9(3)	

Table S4. Selected experimental and calculated (DFT) bond lengths (Å) and angles (º) for complexes **4a**-**4d**. Atoms X1/X2 refer to the halogen atoms in 5 and 7 positions of the 8-hydroxyquinolinate.

	4a	**4a** (DFT)	**4b**	**4b** (DFT)	**4c**	**4c** (DFT)	**4d**	**4d** (DFT)
Lengths (Å)								
B(1)-O(1)	1.531(6)	1.527	1.549(3)	1.533	1.538(4)	1.531	1.545(5)	1.531
B(1)-C(12)	1.609(7)	1.609	1.592(4)	1.608	1.596(6)	1.609	1.597(7)	1.609
B(1)-C(1)	1.621(7)	1.607	1.611(4)	1.608	1.612(5)	1.607	1.602(6)	1.607
B(1)-N(1)	1.629(7)	1.622	1.628(3)	1.622	1.635(5)	1.622	1.617(5)	1.621
C(1)-C(2)	1.385(7)	1.397	1.389(4)	1.397	1.382(5)	1.397	1.391(6)	1.397
C(1)-C(6)	1.399(7)	1.399	1.398(3)	1.399	1.396(5)	1.399	1.387(6)	1.399
C(7)-C(12)	1.395(7)	1.399	1.413(3)	1.399	1.408(5)	1.399	1.396(6)	1.399
C(11)-C(12)	1.398(6)	1.398	1.400(4)	1.398	1.396(5)	1.398	1.384(6)	1.398
C(13)-N(1)	1.326(6)	1..319	1.327(3)	1.320	1.328(5)	1.320	1.323(5)	1.319
C(16)-C(21)	1.406(7)	1.400	1.402(3)	1.399	1.406(5)	1.399	1.394(5)	1.401
C(16)-C(17)	1.418(7)	1.413	1.418(3)	1.414	1.419(5)	1.415	1.416(6)	1.418
C(17)-C(18)	1.359(7)	1.374	1.374(3)	1.372	1.366(5)	1.373	1.386(6)	1.375
C(17)-X(1)	1.884(5)	1.901	1.896(2)	1.898	1.735(4)	1.739	2.092(4)	2.108
C(18)-C(19)	1.414(7)	1.411	1.421(3)	1.411	1.430(5)	1.414	1.407(6)	1.415
C(19)-C(20)	1.386(6)	1.375	1.368(3)	1.377	1.368(5)	1.378	1.371(6)	1.377
C(19)-X(2)	-	-	1.885(2)	1.890	2.077(4)	2.097	2.082(4)	2.098
C(20)-O(1)	1.340(6)	1.326	1.335(2)	1.319	1.334(4)	1.321	1.326(5)	1.320
C(20)-C(21)	1.396(7)	1.407	1.407(3)	1.408	1.413(5)	1.409	1.404(5)	1.409
C(21)-N(1)	1.361(6)	1.348	1.362(3)	1.348	1.357(4)	1.349	1.363(5)	1.349
Angles (º)								
O(1)-B(1)-C(12)	110.1(4)	110.6	108.9(2)	110.0	109.2(3)	110.8	107.7(3)	111.5
O(1)-B(1)-C(1)	110.6(4)	111.2	110.7(2)	110.9	111.0(3)	111.5	111.1(3)	110.9
C(12)-B(1)-C(1)	117.0(4)	115.9	117.3(2)	115.8	117.5(3)	115.3	117.1(3)	115.2
O(1)-B(1)-N(1)	98.4(4)	98.7	98.1(2)	98.5	98.5(2)	98.5	98.4(3)	98.5
C(12)-B(1)-N(1)	108.2(4)	110.5	112.0(2)	110.4	111.3(3)	110.5	112.3(3)	110.6
C(1)-B(1)-N(1)	110.9(4)	108.7	108.2(2)	108.8	107.6(3)	109.0	108.6(3)	108.9
C(2)-C(1)-C(6)	117.8(4)		117.1(2)		117.1(3)		116.6(4)	
C(2)-C(1)-B(1)	123.0(4)		122.0(2)		122.2(3)		121.5(4)	
C(6)-C(1)-B(1)	118.8(4)		120.8(2)		120.6(4)		121.9(4)	
C(11)-C(12)-C(7)	116.8(4)		115.7(2)		116.1(4)		116.3(4)	
C(11)-C(12)-B(1)	120.3(4)		125.8(2)		125.8(3)		124.6(4)	
C(7)-C(12)-B(1)	122.7(4)		118.5(2)		117.9(3)		118.9(4)	
C(21)-C(16)-C(17)	115.7(4)		114.8(4)		114.7(3)		114.8(3)	
C(18)-C(17)-C(16)	120.7(5)		121.4(2)		121.3(3)		120.7(4)	
C(18)-C(17)-X(1)	120.0(4)		120.2(2)		120.2(3)		119.6(3)	
C(16)-C(17)-X(1)	119.3(4)		118.4(2)		118.5(3)		119.7(3)	
C(17)-C(18)-C(19)	123.9(5)		121.0(2)		121.8(3)		121.7(4)	
C(20)-C(19)-C(18)	117.3(5)		120.2(2)		119.4(3)		119.7(4)	
C(20)-C(19)-X(2)	-		119.7(2)		119.8(3)		119.5(3)	
C(18)-C(19)-X(2)	-		120.1(3)		120.8(3)		120.8(3)	
O(1)-C(20)-C(19)	128.8(5)		130.1(2)		129.9(3)		129.6(4)	
O(1)-C(20)-C(21)	113.1(4)		112.9(2)		112.7(3)		113.2(3)	
C(19)-C(20)-C(21)	118.1(4)		117.0(2)		117.3(3)		117.1(4)	
N(1)-C(21)-C(16)	123.9(4)		124.2(2)		124.1(3)		124.1(3)	
N(1)-C(21)-C(20)	110.2(4)		110.3(2)		110.5(3)		110.0(3)	
C(16)-C(21)-C(20)	125.8(5)		125.5(2)		125.4(3)		125.9(4)	
C(13)-N(1)-C(21)	119.8(4)		119.3(2)		119.2(3)		119.0(3)	
C(13)-N(1)-B(1)	132.2(4)		132.5(2)		133.1(3)		132.9(3)	
C(21)-N(1)-B(1)	107.9(4)		108.2(2)		107.6(3)		108.0(3)	
C(20)-O(1)-B(1)	110.3(4)		110.3(2)		110.3(3)		110.0(3)	

Single crystal X-ray diffraction structures of complexes 3a and 4b

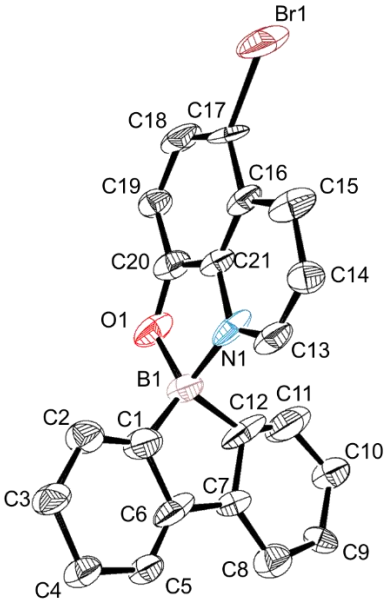

Fig. S25. Perspective view of the molecular structure of complex **3a**. The calculated hydrogen atoms were omitted for clarity and the ellipsoids were drawn at the 50% probability level.

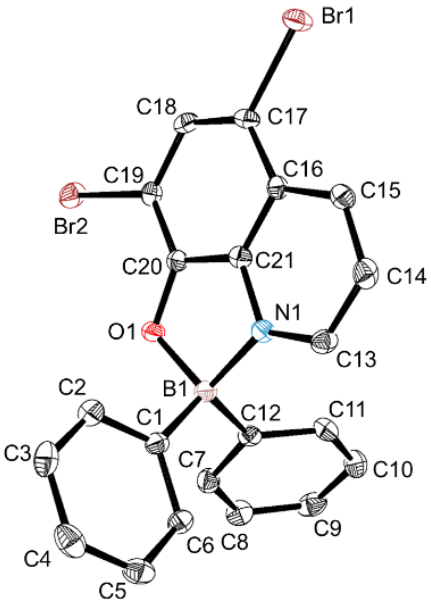

Fig. S26. Perspective view of the molecular structure of complex **4b**. The calculated hydrogen atoms were omitted for clarity and the ellipsoids were drawn at the 50% probability level.

Computational studies – Structures

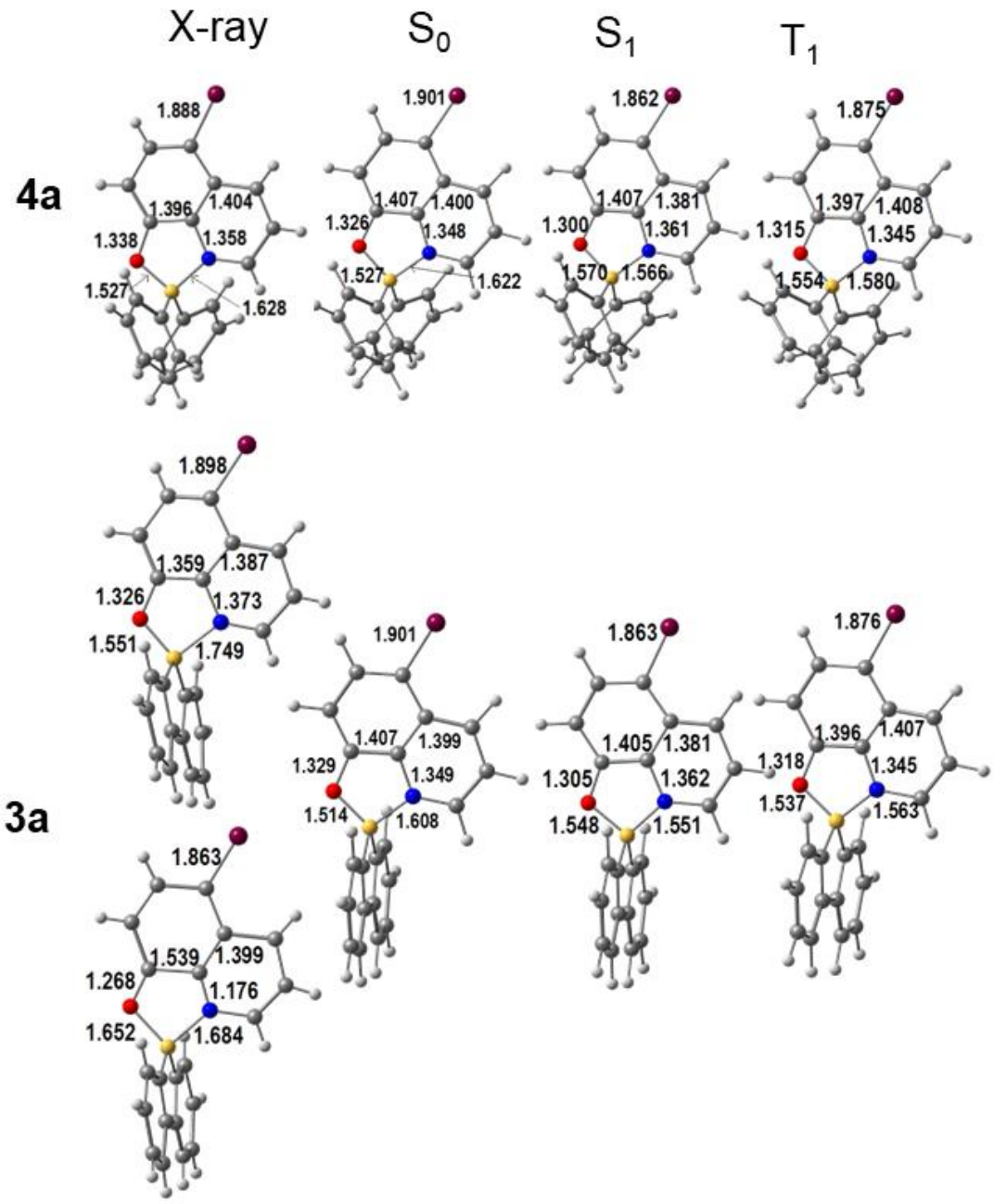

Fig. S27. Experimental (X-ray) and calculated bond distances (Å) for the S_0, S_1 and T_1 states of the bromide derivatives **4a** and **3a**.

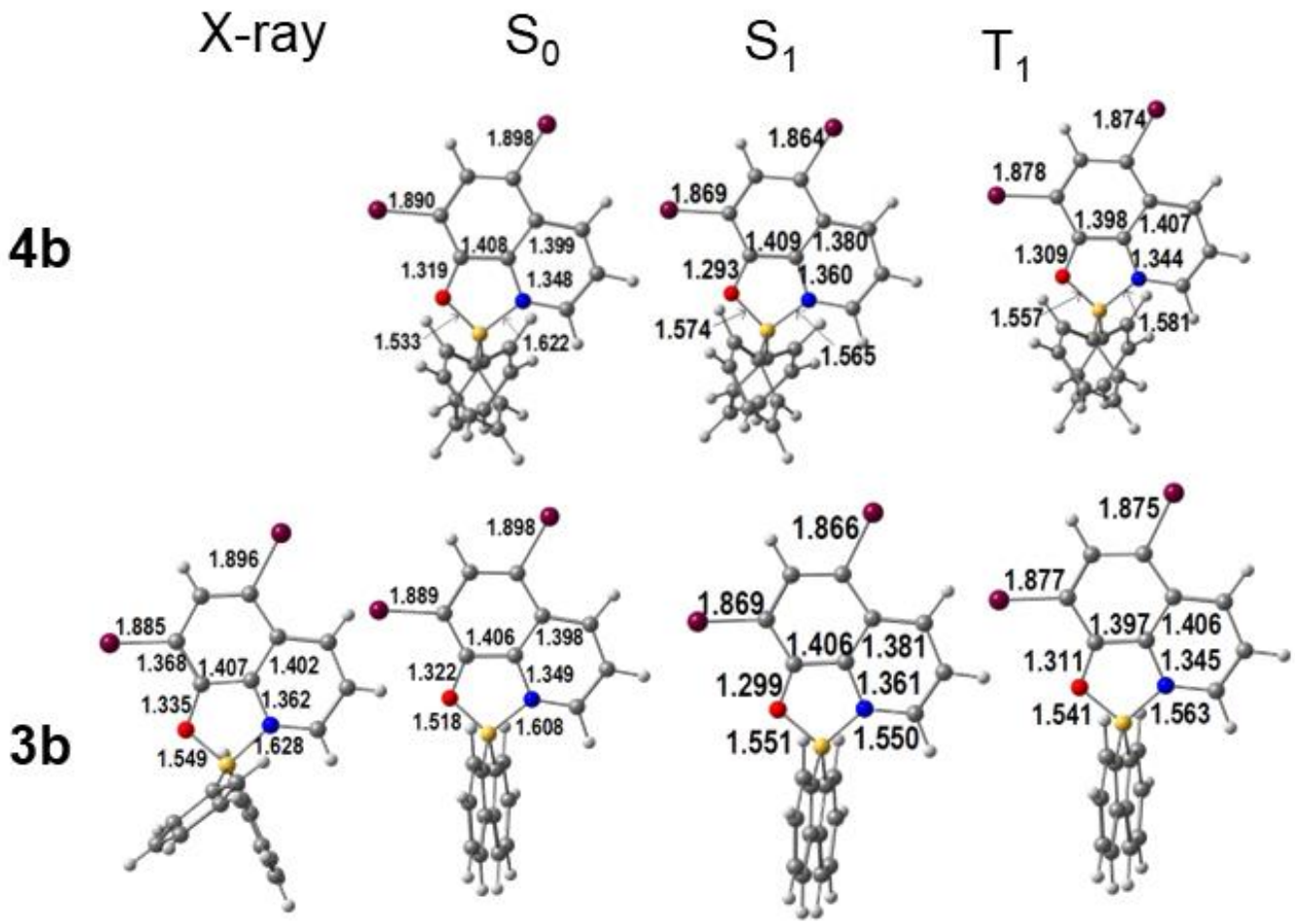

Fig. S28. Experimental (X-ray) and calculated bond distances (Å) for the S_0, S_1 and T_1 states of the two dibromide derivatives **4b** and **3b**.

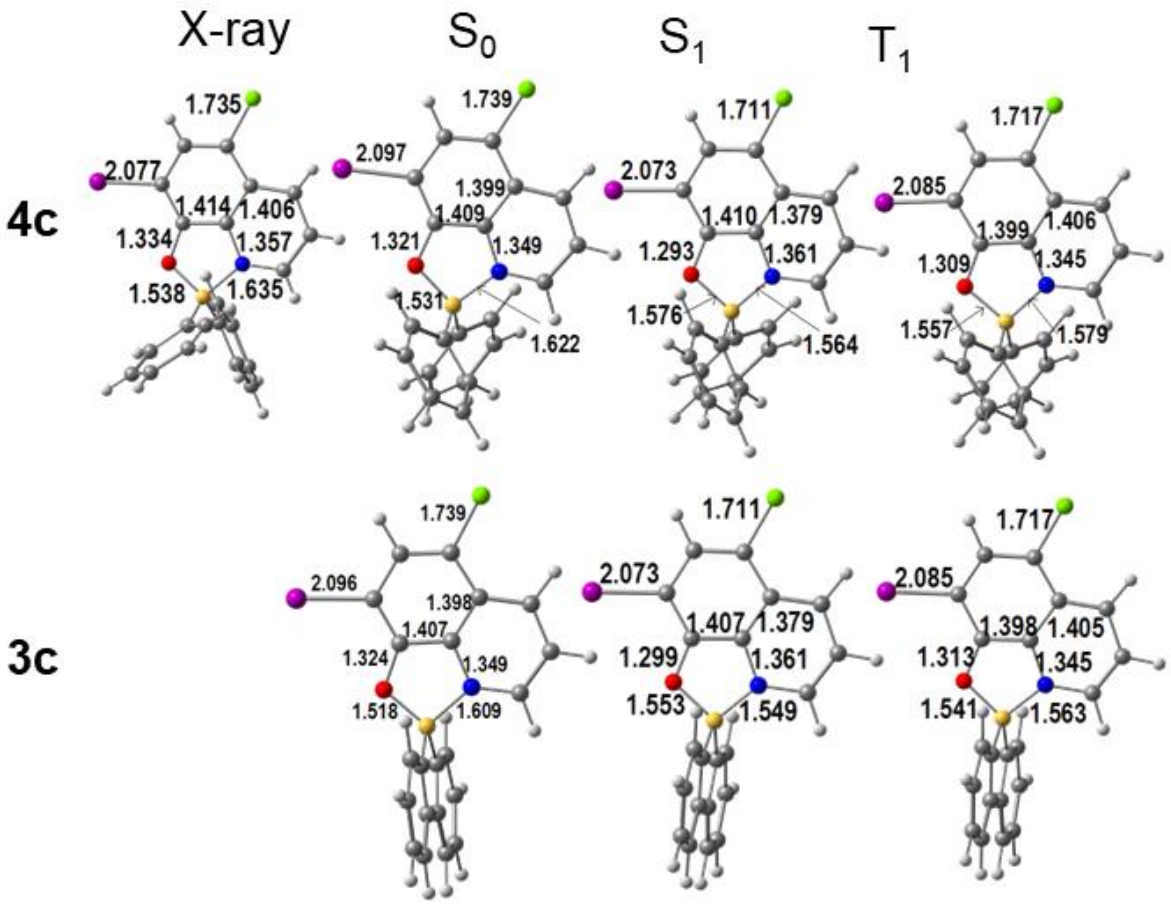

Fig. S29. Experimental (X-ray) and calculated bond distances (Å) for the S_0, S_1 and T_1 states of the chloroiodide derivatives **4c** and **3c**.

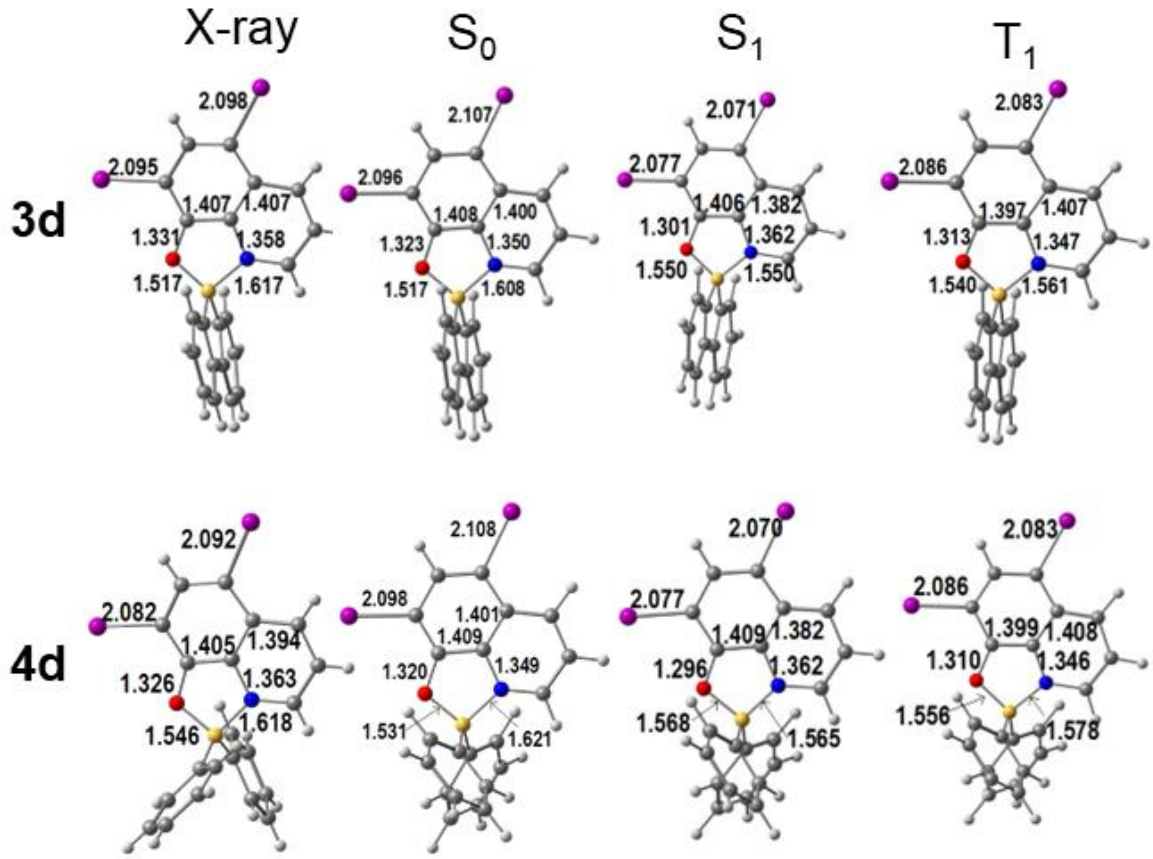

Fig. S30. Experimental (X-ray) and calculated bond distances (Å) for the S_0, S_1 and T_1 states of the diiodide derivatives **4d** and **3d**.

Table S5. Calculated dipole moments (D) for complexes **3** and **4a-d** in S_0, S_{1FC} and S_1 states.

Complex	R^1	R^2	μ_{S0}	μ_{S1FC} [a]	μ_{S1}
4a	Br	H	5.86	5.53	5.95
3a	Br	H	6.30	5.43	6.42
4b	Br	Br	7.36	5.27	7.40
3b	Br	Br	7.73	5.10	7.85
4c	Cl	I	6.73	4.82	6.85
3c	Cl	I	7.11	4.72	7.30
4d	I	I	7.16	6.50	7.12
3d	I	I	7.58	6.45	7.60

[a] S_{1FC} is the non-relaxed singlet excited state (calculated at the S_0 relaxed geometry).

Table S6. More intense TD-DFT electronic transitions calculated for complexes **3** and **4**.

Complexes	**Transition**	***λ* (nm)**	***E* (eV)**	**Composition**	**O.S.**
3a	1	404	3.056	H→L (94%), H-1→L (4%)	0.119
	2	391	3.171	H-1→L (94%), H→L (4%)	0.079
3b	1	406	3.015	H→L (92%), H-1→L (6%)	0.088
	2	391	3.117	H-1→L (91%), H→L (7%)	0.104
3c	1	413	3.004	H→L (96%)	0.101
	2	398	3.114	H-1→L (98%)	0.065
3d	1	417	2.977	H→L (98%)	0.144
	2	398	3.118	H-1→L (99%)	0.038
4a	1	400	3.102	H→L (96%)	0.173
4b	1	404	3.072	H→L (96%)	0.154
4c	1	406	3.052	H→L (96%)	0.131
4d	1	416	2.977	H→L (97%)	0.150

Delayed fluorescence and phosphorescence spectra of complexes 3a-3d and 4a-4d

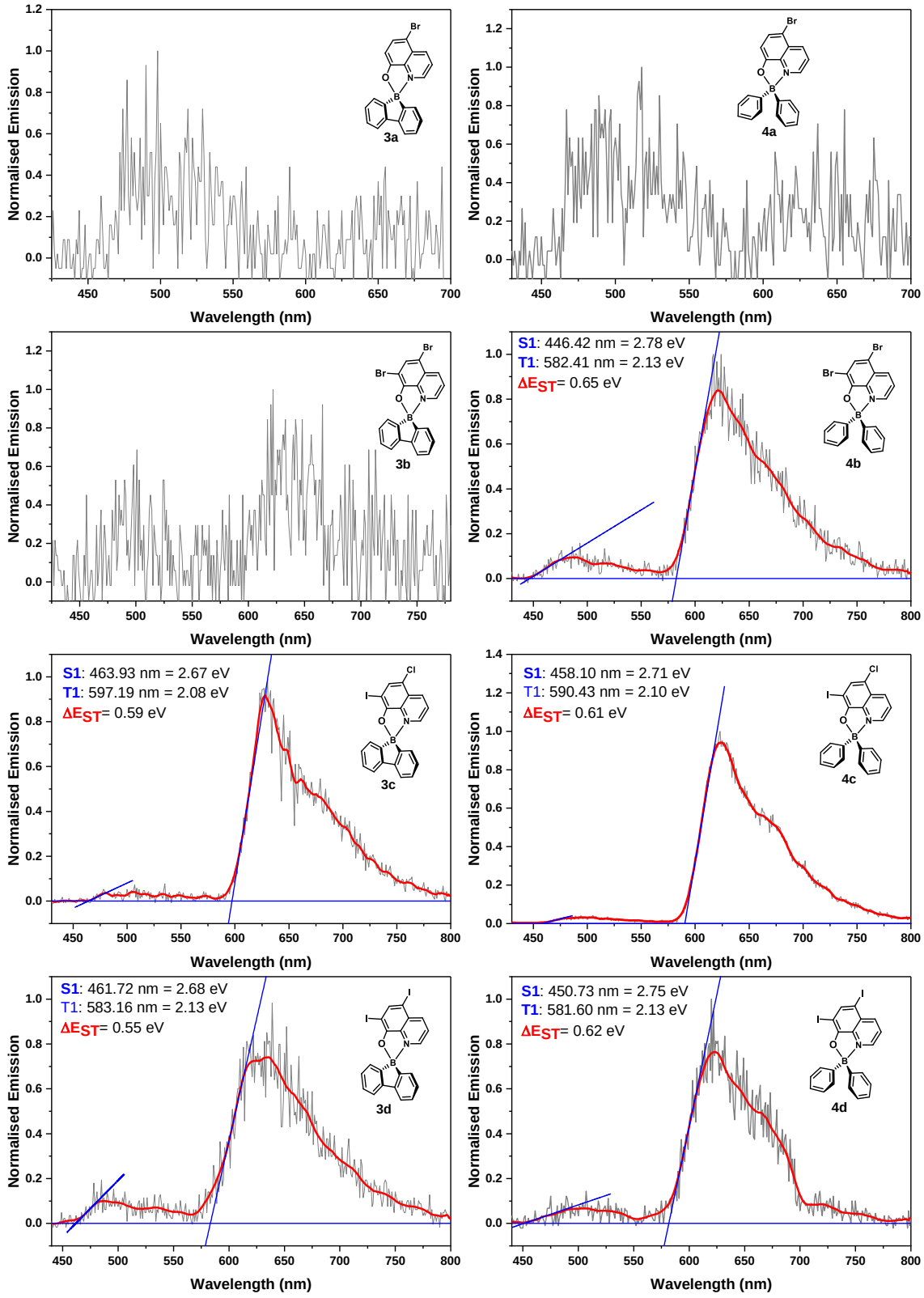

Fig. S31. Fluorescence and phosphorescence emission of the complexes **3a**-**3d** and **4 a**-**4d**, in 2-Me-THF, at 77 K, measured with a 10 ms sample window and with 50 µs of delay upon excitation. (grey line) The poorly resolved spectra were smoothed just for clarification (red line) allowing the calculation of lowest S_1 and T_1 energies from the onset of the emission spectra (blue lines).

Computational studies – Absorption and emission

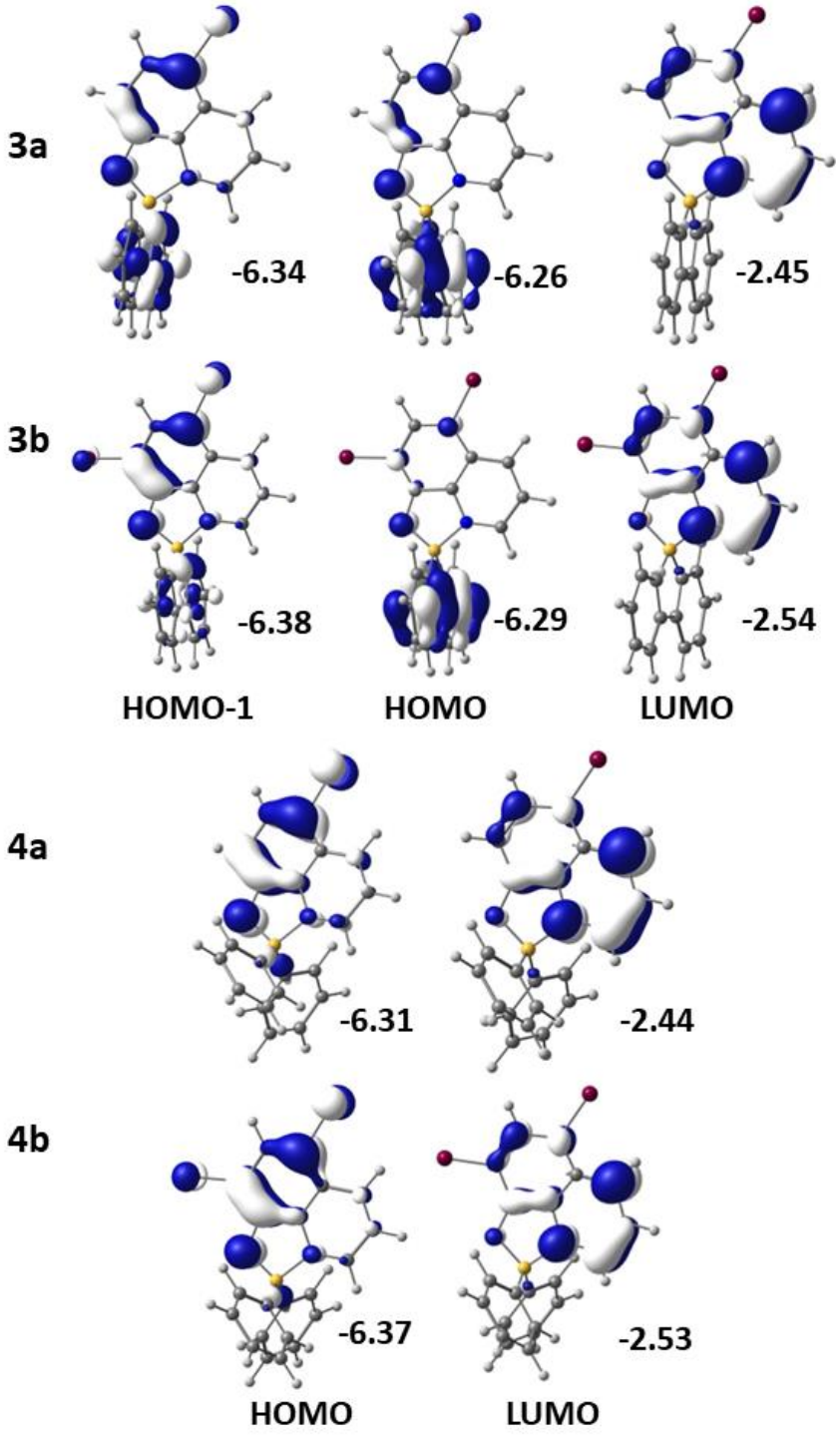

Fig. S32. Relevant frontier orbitals and their energies (eV) for complexes **3a**, **3b**, **4a** and **4b**.

Table S7. Calculated HOMOs and LUMOS energies (eV) for complexes **3** and **4** using different methods.

Complex	A		A/D3		B		B/D3		GP		THF		CH_2Cl_2	
	HOMO	**LUMO**	**HOMO**	**LUMO**	**HOMO**	**LUMO**	**HOMO**	**LUMO**	**HOMO**	**LUMO**	**HOMO**	**LUMO**	**HOMO**	**LUMO**
3a	-6.259	-2.454	-6.263	-2.449	-5.923	-2.511	-5.926	-2.504	-5.304	-3.562	-5.367	-3.281	-5.359	-3.263
3b	-6.290	-2.554	-6.293	-2.540	-5.951	-2.601	-5.951	-2.595	-5.353	-3.686	-5.411	-3.356	-5.403	-3.336
3c	-6.266	-2.521	-6.269	-2.519	-5.933	-2.594	-5.936	-2.570	-5.353	-3.684	-5.371	-3.342	-5.362	-3.323
3d	-6.232	-2.501	-6.234	-2.449	-5.910	-2.544	-5.913	-2.539	-5.346	-3.663	-5.329	-3.321	-5.320	-3.302
4a	-6.305	-2.442	-6.307	-2.439	-6.006	-2.495	-6.010	-2.488	-5.518	-3.555	-5.391	-3.274	-5.302	-3.257
4b	-6.366	-2.530	-6.370	-2.529	-6.072	-2.581	-6.079	-2.578	-5.601	-3.676	-5.442	-3.346	-5.433	-3.328
4c	-6.300	-2.507	-6.303	-2.506	-6.002	-2.552	-6.007	-2.553	-5.575	-3.678	-5.392	-3.332	-5.384	-3.314
4d	-6.246	-2.488	-6.248	-2.486	-5.941	-2.529	-5.946	-2.526	-5.555	-3.656	-5.347	-3.312	-5.339	-3.295

A – PBE0, TZP (all electron), THF, SO
A/D3 – PBE0/D3, TZP (all electron), THF, SO
B – B3LYP, TZP (all electron), THF, SO
B/D3 – B3LYP/D3, TZP (all electron), THF, SO
GP – BP86 (small core, T2ZP)
THF – BP86 (small core, T2ZP), THF (single point)
CH_2Cl_2 – BP86 (small core, T2ZP), dichloromethane (single point)

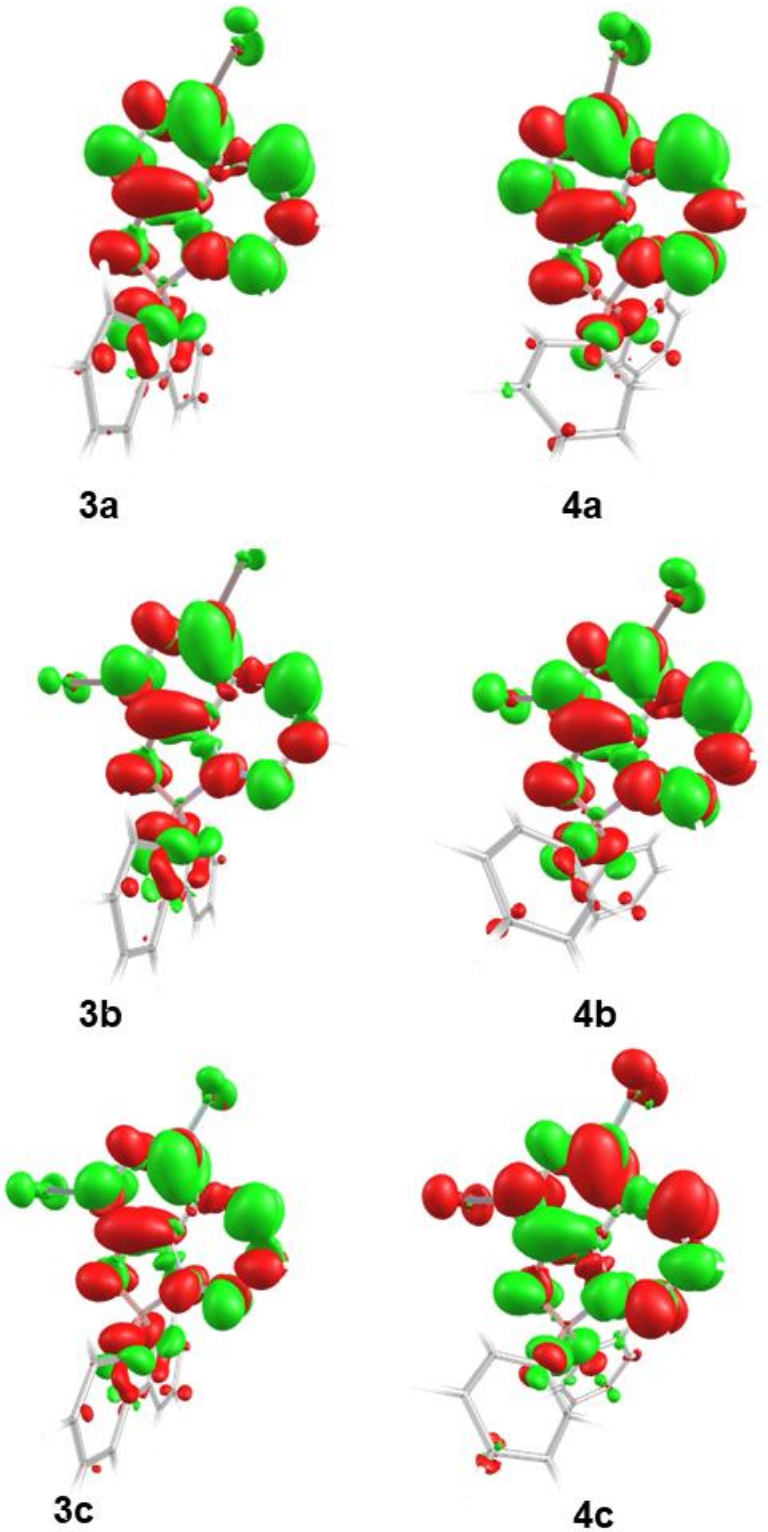

Fig. S33. Charge density plots for complexes **3a**-**3c** (left) and **4a**-**4c** (right) for the lowest energy transition (red: increased electron density; green: decreased electron density; contour value 0.0008).

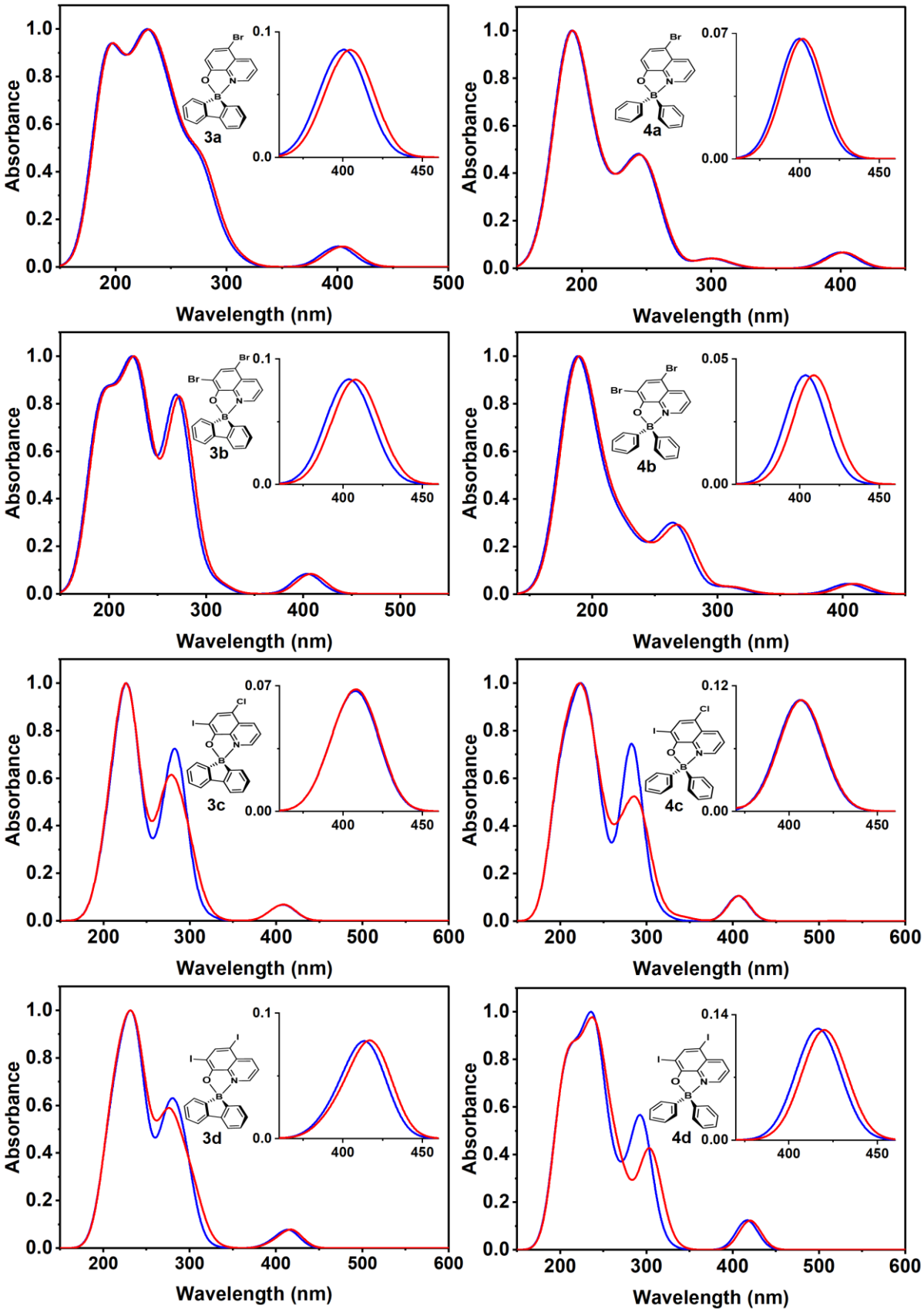

Fig. S34. TDDFT calculated absorption spectra for complexes **3a**-**3d** (left) and **4a**-**4d** (right) with spin-orbit coupling included (red) or not (blue).

Table S8. Energies of S_1 and T_1 states (eV) for complexes **3** and **4** calculated using different methods.

Complex	S_1					T_1				
	A	**B**	**A/D3**	**B/D3**	**GP**	**A**	**B**	**A/D3**	**B/D3**	**GP**
4a	2.324	2.219	2.332	2.233	1.858	1.439	1.456	1.444	1.462	1.479
3a	2.321	2.234	2.328	2.239	1.728	1.428	1.449	1.431	1.454	1.515
4b	2.325	2.218	2.333	2.231	1.898	1.464	1.477	1.444	1.483	1.500
3b	2.327	2.183	2.331	2.166	1.840	1.448	1.466	1.452	1.471	1.464
4c	2.290	2.175	2.299	2.179	1.939	1.429	1.435	1.434	1.437	1.485
3c	2.296	2.204	2.302	2.208	1.883	1.423	1.439	1.426	1.444	1.452
4d	2.297	2.180	2.304	2.190	1.997	1.466	1.468	1.470	1.476	1.513
3d	2.296	2.240	2.303	2.232	1.939	1.456	1.462	1.459	1.468	1.477

A – PBE0, TZP (all electron), THF, SO
A/D3 – PBE0/D3, TZP (all electron), THF, SO
B – B3LYP, TZP (all electron), THF, SO
B/D3 – B3LYP/D3, T2P (all electron), THF, SO
GP – BP86 (small core, TZ2P)

Transient emission spectra of complexes 3a, 3c and 4a and 4c in solid-state films

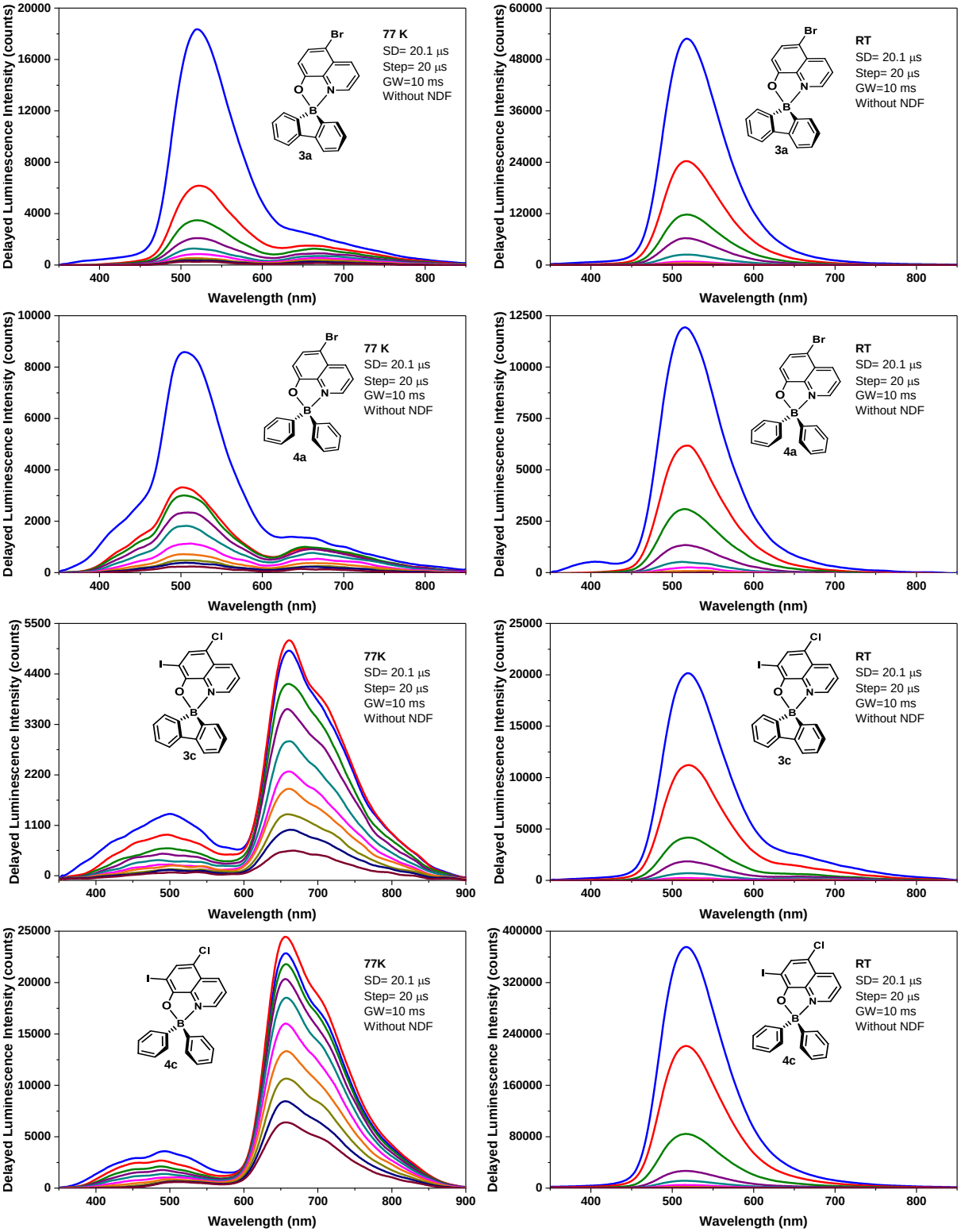

Fig. S35. Transient emission spectra of complexes **3a**, **3c**, **4a** and **4c** in ZEONEX 480R films (1% wt) at 77 K (left) and room temperature (*ca.* 293 K) (right). All spectra were recorded with a start delay (SD) of 20.1 μs (blue curve) and recorded every 20 μs (Step), with the use of a large gate width (GW=10 ms). DF intensity decreases with increasing delay time.

Studies of Delayed Fluorescence *vs* Excitation Dose for complexes 3a-3c and 4b-4d

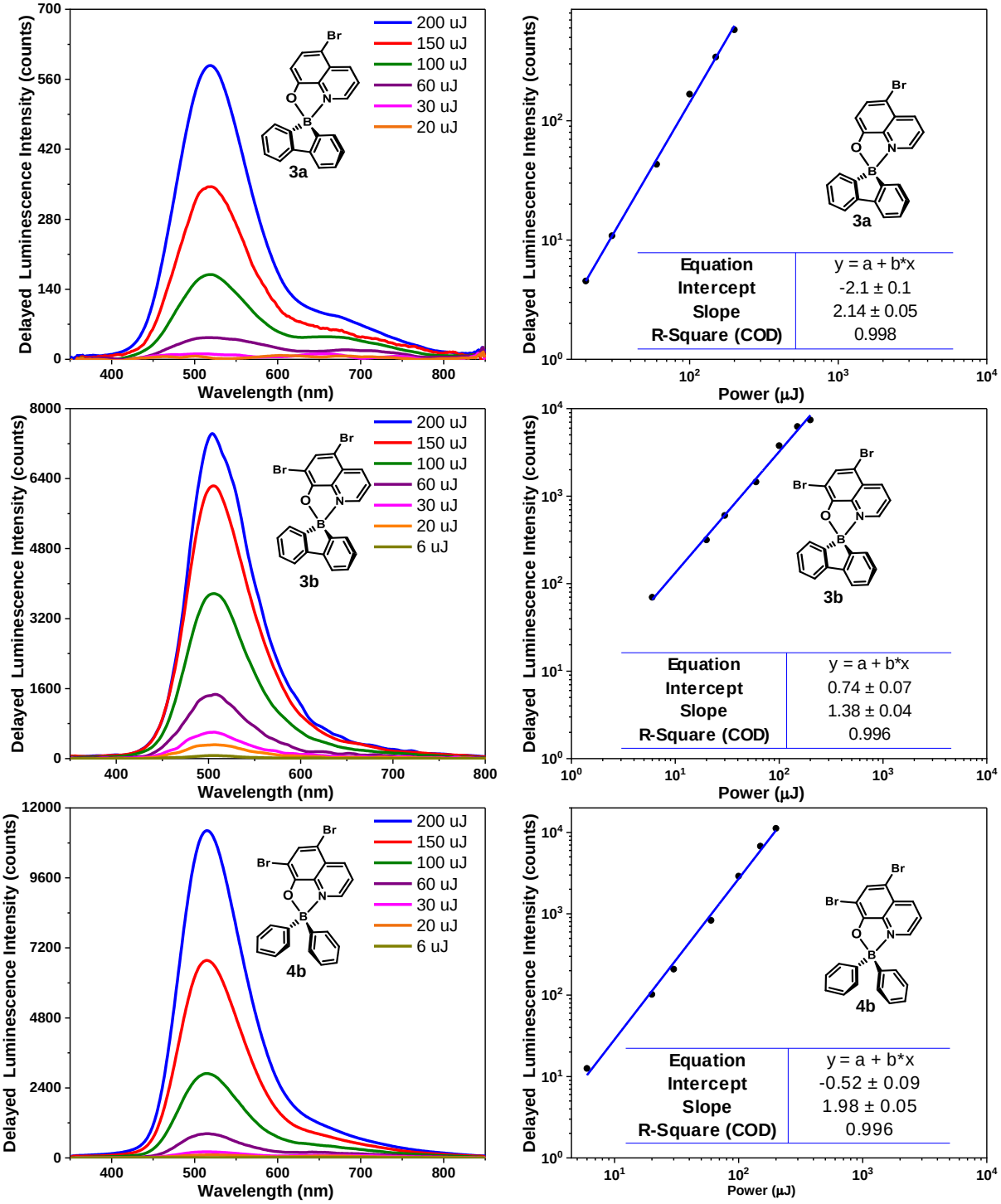

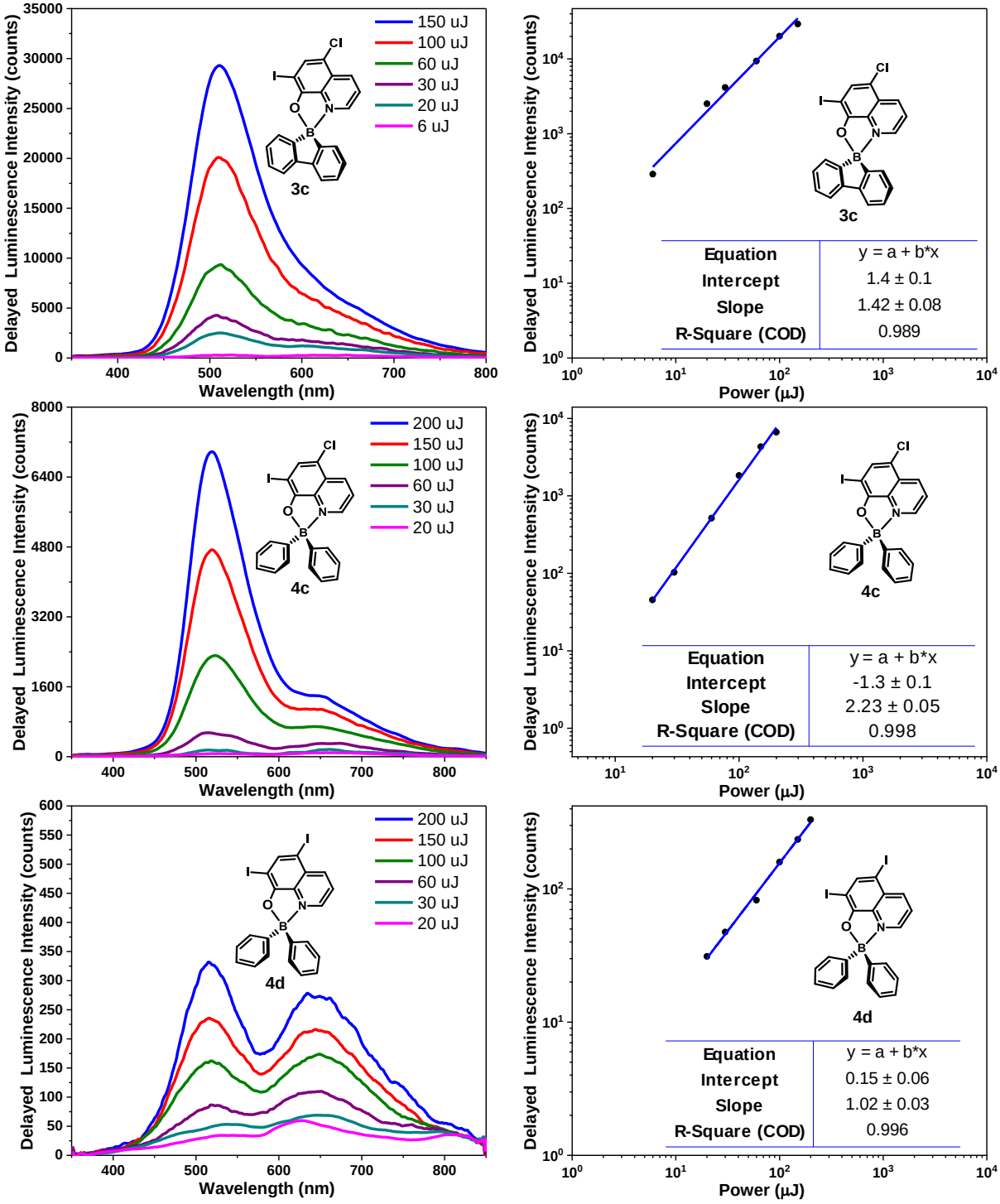

Fig. S36. Dependence of the DF intensity (with a start delay (SD) of 20 µs) on the excitation dose for the complexes **3a-3c** and **4b-4d**, in ZEONEX 480R films at room temperature (*ca.* 293 K) (left), and log-log plot of DF intensity versus excitation dose (right).

Jablonski diagrams for complexes 3a-3c and 4a-4c

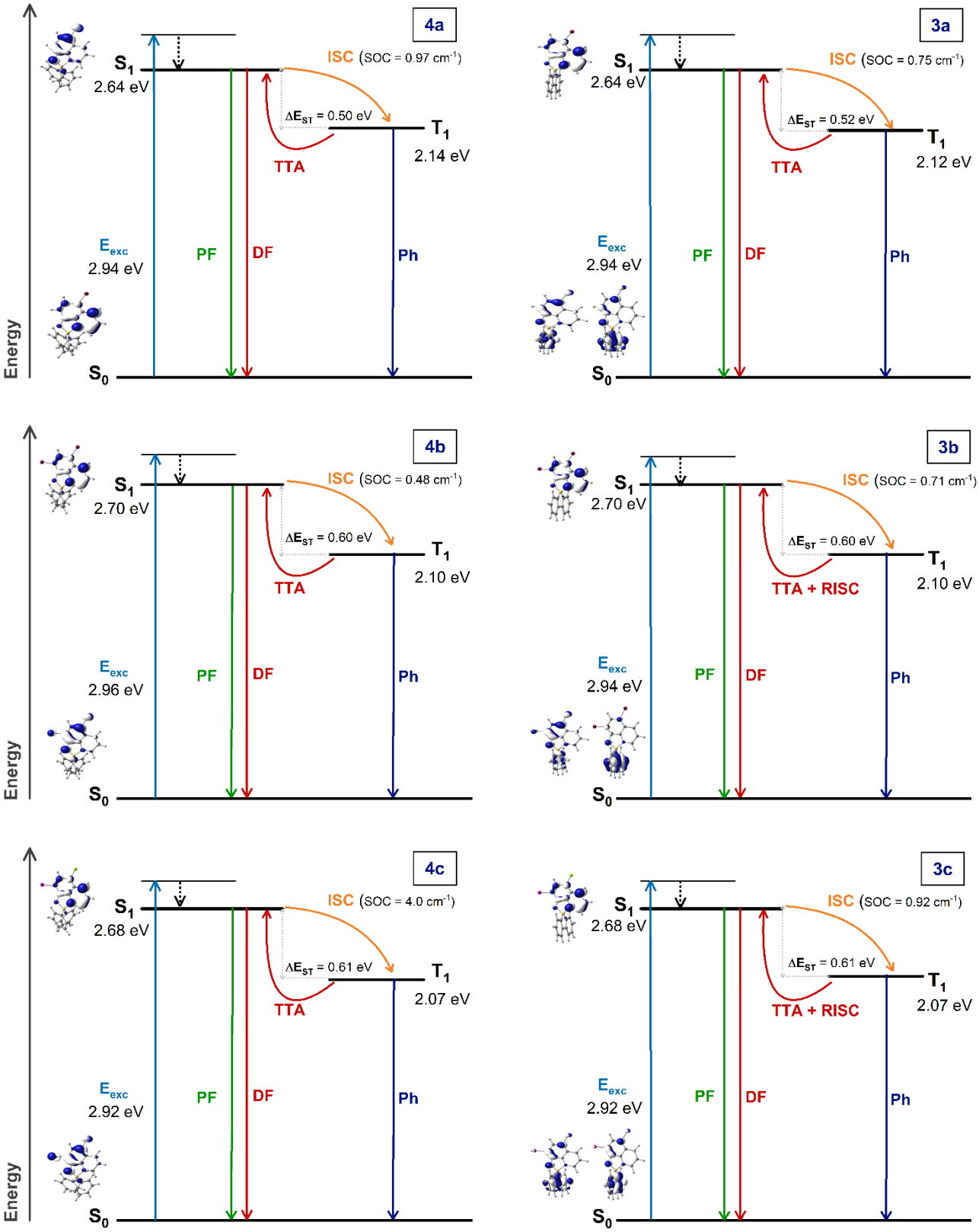

Fig. S37. Jablonski diagrams of complexes **3a-3c** (right) and **4a-4c** (left) illustrating their most relevant photophysical processes and properties, in ZEONEX 480R films, at room temperature (*ca.* 293 K). The values exhibited are experimental, except those of the DFT-calculated SOC values.

Electroluminescent devices

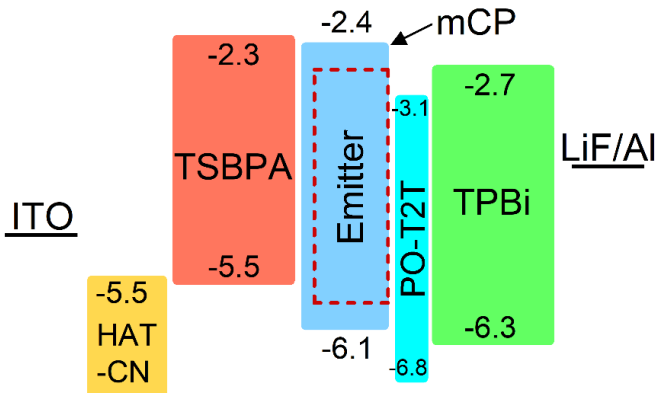

Fig. S38. Graphical representation of the architecture of OLEDs using **3a**, **4a**, **3b**, and **4b** in the emissive layer: ITO | HAT-CN (10 nm) | TSBPA (40 nm) | mCP (2 nm) | mCP co 10% **emitter** (20 nm) | PO-T2T (5 nm) | TPBi (40 nm) | LiF (0.8 nm) | Al (100 nm). Numerical values in eV represent the energy of HOMO (bottom) and LUMO (top).

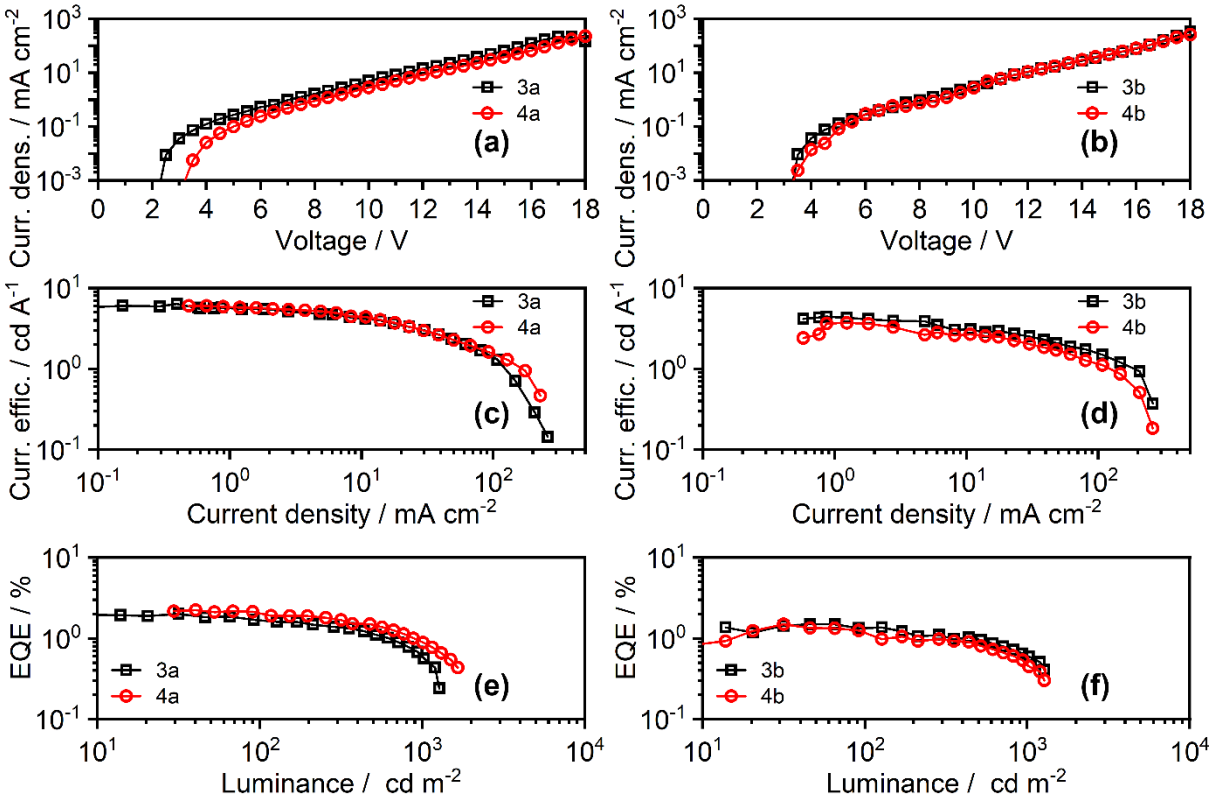

Fig. S39. Characteristics of OLED devices using **3a**, **4a**, **3b**, and **4b** in the emissive layer: (a) and (b) Current density – voltage; (c) and (d) Current efficiency - current density; and (e) and (f) External quantum efficiency - luminance.